Effects of temperature and ultrasound on nucleation behavior during electrochemical synthesis of copper thin films

Archana Mallik

Effects of temperature and ultrasound on nucleation behavior during electrochemical synthesis of copper thin films

A thesis submitted in partial fulfillment of the
requirements for the degree of

DOCTOR OF PHILOSOPHY

by

Archana Mallik
(Roll No. – 50604001)

Department of Metallurgical and Materials Engineering
National Institute of Technology
Rourkela - 769008
India

August 2010

Supervisors

Prof. Bankim Chandra Ray
Prof. Upendra Kumar Mohanty

It follows that it cannot be our task to find an absolutely correct theory, but rather a picture that is as simple as possible while representing the phenomenon as well as possible.

Ludwig Boltzmann

Dedicated to my nation

“INDIA”

Department of Metallurgical and Materials Engineering,
National Institute of Technology
Rourkela-769008
India

CERTIFICATE

This is to certify that the thesis entitled "**Effects of temperature and ultrasound on nucleation behavior during electrochemical synthesis of copper thin films"** submitted by **Archana Mallik** to National Institute of Technology, Rourkela is a record of bonafide research work under our supervision and is worthy of consideration for the award of the degree of Doctor of Philosophy of the Institute. The candidate has fulfilled all prescribed requirements for the thesis, which is based on candidate's own work, has not been submitted elsewhere for a degree or diploma.

Prof. B. C. Ray
Supervisor

Prof. U. K. Mohanty
Co-supervisor

Acknowledgement

This study was carried out at the Department of Metallurgical and Materials Engineering, National Institute of Technology, Rourkela, India.

At this juncture I had to remember my statement while graduating bachelor's degree that "I want to be a giant in Metallurgy". Subsequently I have had the passion to work in scientific fields in an active research group. There are many people in this way helped me to achieve first stages of this goal. First of all, I am highly grateful to my first supervisor, Prof. Bankim Chandra Ray for believing in me and encouraging me to study PhD and pursue my dreams. I know him as a person who has changed my whole life by his unconditional support and never ending patience. He also deserves my earnest thanks for making me learn on how to unravel science, me being a technical person. Bankim, you inspired me how to be observant and how to grasp any phenomenon with a simple scientific view. You also showed me how to deal with conflicts and difficulties in life. I am also thankful for the extra efforts you put to develop my communication skills ranging from writing to presentation. I am so lucky to have spent my studies under the guidance of an intelligent, open minded, forgiving, honest and beloved person like you. You are indeed my best teacher ever! Many thanks Bankim!

I am also highly grateful to my second supervisor Prof. U. K. Mohanty for his constant support and encouragement.

I would like to thank Prof. Sunil Sarangi, Director, for the learning lessons from a great persona with a kind heart full of dedications, management and compassion.

I am also thankful to laboratory members of Department of Metallurgical and Materials Engineering, NIT Rourkela, especially, R. Pattanaik, S. Pradhan, U. K. Sahu and S. Hembram for constant practical assistance and help whenever required. Special thanks go to Prof. J. Bera, Dept. of Ceramic Engg., for allowing me to operate and conduct experiments in AFM. I also appreciate Prof. S. Paria's help in conducting experiments of surface energy in Dept. of Chemical Engg.

I thank Mr. M. Madhan, Mr. Y. S. V. Rao and Ms. Shipra, our potential library committee for their help in getting literature needed for the work.

Thanks to all the help and company I received from National Metallurgical Laboratory, Jamshedpur and Institute of Minerals and Materials Technology, Bhubaneswar. Dr. K. L. Sahoo and Dr. S. Pradhan have always been so helpful.

My special thanks go to my master students Ram, Rakesh, Seshadev, Anil, Arpita and Sabita. Their questions and queries have helped me to approach towards the research world in a more focused and constructed angle. Thanks!

My sincere thanks are to Prof. B. B. Verma, Head, Department of Metallurgical and Materials Engineering, for providing necessary facility for this work.

My sincere gratitude to members of my doctoral scrutiny committee: Prof. B. B. Verma, Prof. R. K. Patel, Prof. S. Paria and Prof. S. Bhattacharya for their help and support throughout this work.

I am thankful to my beloved son, Anu for all the innocent love, plenty of soothing smiles, sweet hugs he has given me. The tiring day of a busy schedule gets refreshed with a sight of his innocent eyes full of

assurance. I would like to thank my husband, Bivu, for his constant support for pursing the studies. You sacrificed so I could pursue this endeavor. A deep sense of gratitude also goes to Laxmi, my maid for taking selfless care of my son in absence of me.

I would like to express my deepest gratitude to my parents and brothers who have always been supporting me in my studies. To my Parents: Shanti Lata Mallik and Arjuna Charan Mallik, to my brothers: Chinu, Appu and Dipu. Thanks for your love and support!

I am grateful to some beautiful persons in my life Soumya, Sanjeev, Mausi, Bhauja.

All errors and limitations remaining in this thesis are mine alone.

Archana Mallik
(August 2010)

Abstract

Temperature is an excellent tool for tuning the phase formation kinetics and hence structure and properties of synthesized materials. The effect of the said parameter with added sonication impact on the electrochemical synthesis of copper thin films has been investigated in the present study. Copper was electroplated on graphite and aluminum substrates from a simple aqueous binary sulfate electrolyte at sub-ambient temperatures in presence of an ultrasonic horn of 20 KHz frequency and 20% output of the total power. The prepared films were characterized by X-ray diffraction and electron microscopic methods i.e. atomic force microscopy (AFM) and scanning electron microscopy (SEM). Reaction kinetics and nucleation mechanism of film formation was investigated by cyclic voltammetry and chrono-amperometry. Mechanical properties and thermal stability of the films were analyzed by nano-indentation and differential scanning calorimetry.

The X-ray diffraction analysis and microscopic studies indicate nano-range deposits with decreasing reaction temperature in both silent and sonication conditions. Crystallinity of both the deposits was confirmed by the sharp XRD peaks. Synthesis under silent conditions had lead to many crystallographic defects as observed by the large peak shifts of X-RD patterns. However, deposits were dendritic powdery and highly scattered in nature in silent conditions. Ultrasound was found to have a significant effect on the deposit morphology. The deposit obtained was compact, uniform and adherent. Energy dispersive spectroscopy result of the deposits revealed an oxidized silent deposit along with some adsorbed sulfur onto the electrode surface. In contrary the in-situ cleaning associated with sonication has resulted in cleaner deposits.

Correlating the morphological investigations (by SEM and AFM) with cyclic voltammetry (CV) and chronoamperometry (CA), the mechanism and kinetics of ultrasound assisted low temperature copper elctrocrystallization has been tried to be portrayed. The results indicate that ultrasound induces secondary nucleation by breaking of the existing primary nuclei in addition to the primary nucleation. The new understanding of the sonoelectrochemical mechanisms clarifies few unclear issues. It could possibly allow for the better design of sonoelectrochemical synthesis. Furthermore it was found that the deposition of copper in the absence of ultrasound had mixed mass and charge transfer kinetics. Copper nucleated according to 3D instantaneous mechanisms for all temperature ranges. The extent of nucleation was found to be increased at low temperatures with a transition of dendritic type morphology to spherical copper deposition. On the other hand, the deposition kinetics was mainly dominated by charge transfer in presence of ultrasound. Diffusion coefficients and nuclei population density were calculated for each temperature range for both presence and absence of ultrasound, both the quantities increased in presence of ultrasound. Sonicated deposits with good surface coverage were found to consist of spherical copper agglomerates of nanosized particles. The results suggest that the effect of power ultrasound on electrochemical systems under a wide range of conditions is non-conventional.

The ex-situ growth kinetics of low temperature sono-electrochemically deposited Cu thin films has been studied under non-isothermal conditions using a differential scanning calorimetric (DSC) technique. The analysis focuses on the effect of deposition temperature on the DSC results. The grain growth mechanism and mode were discussed by determining the variation of the activation and surface energies of the films.

The kinetic observations were then correlated with the morphological evolution of the films using scanning electron microscopy and atomic force microscopy. The results suggest a transition of abnormal growth to normal mode of growth behavior as the film synthesis temperature was reduced.

Knowledge of internal stresses in thin copper film structures is essential in understanding the film properties, such as stress migration, adhesion, hardness and elasticity. The variation of internal stresses and nano-mechanical properties were studied with decreasing deposition temperature of the films. Irrespective of deposition temperature, the stress was observed to be compressive and increased at low electrolyte temperatures. Hardness and elasticity of the films were found to be increased with reduced deposition temperature. With increasing compressive stress, the hardness of the films increased. Hence, residual compressive stresses were expected to blunt crack tips and suppress crack propagation. The surface adhesion of the film deposited at 5 °C was minimum, indicating increased cleanliness and chemical stability with low deposition temperatures.

The mechanism of electrodeposition of copper thin film on aluminum has been studied under the influence of power ultrasound using cyclic voltammetry. The deposited thin films were characterized by x-ray diffraction, scanning electron microscope and atomic force microscope. Films are crystalline in structure. The spherical copper domains of the deposits without sonication have been converted to mushroom structures in presence of ultrasound. Properties, including thermal and mechanical are further analyzed using differential scanning calorimeter and nano-indentation. The films were comparatively stable than the graphite coated films. Further the soft films are found to have good wear properties.

Keywords

Copper, Sono-electrodeposition, Low-temperature, Thin film, Electrocrystallization, Secondary Nucleation, Kinetics, AFM, Residual stress, Hardness, Surface analysis, Profilometry, Nano-indentation, Grain growth, Thermal properties, DSC.

Contents Page No.

List of figures

List of tables

Nomenclature

Major Roman and Greek Symbols

A_j	Constant of proportionality
α	Transportation number
B	Boltzman constant, $J\ K^{-1}$
β_{total}	Total Broadening, Radians
C*	Bulk concentration of electroactive species, M
C_N	Metastable equilibrium concentration of critical clusters
C_L	No. of atoms per unit volume in liquid
C_{sys}	Heat capacity of system, $J\ K^{-1}$
D	Diffusion coefficient, $cm^2 s^{-1}$
d	Crystallite size, nm
δ	Diffusion layer thickness, cm
E	Potential, V
E^0	Equilibrium potential, V
E_{pa}	Peak potential in the anodic scan, V
E_{pc}	Peak potential in the cathodic scan, V
ε	Internal strain
F	Faraday constant, C
G_0	Standard free energy, kJ, kJ $mole^{-1}$
$\Delta G(N)$	Gibbs free energy for formation of cluster of N ions, kJ, kJ $mole^{-1}$
ΔH_d	Activation energy barrier for interfacial diffusion, J $mole^{-1}$
I	Current, A
I_{lim}	Limiting current, A
I_m	Current at maxima, A
i_{pa}	Anodic peak current, A
i_{pc}	Cathodic peak current, A
i_{pf}	Peak current in forward scan, A
i_{pr}	Peak current in reverse scan, A
J	Nucleation rate
J_0	Equilibrium nucleation rate
k	$\left(\frac{8\pi CM}{\rho}\right)^{0.5}$ (dimensionless)
λ^{-1}	Non dimensional quantity
M	Molar mass of electroactive species, M
μ^{sol}	Chemical potential of solution, kJ $mole^{-1}$
μ^{ion}	Chemical potential of ions, kJ $mole^{-1}$
$\Delta\mu$	Supersaturation
n	electrons involved
N	Cluster dimensionality (1, 2 or 3)
N_0	Saturation nuclei density, cm^{-3}
ν	Vibration frequency, s^{-1}
ν_{sl}	Jump frequency of atoms from liquid to critical clusters, s^{-1}
ρ	Density of electrodeposit, g cm^{-3}
P_W	Ultrasonic power, W cm^{-2}
Q	Total charge consumed, C
R	Gas constant, $J\ K^{-1}\ mol^{-1}$
S_{crit}	No. of atoms surrounding a critical cluster

σ^d	Excess charge density in the diffuse layer, C cm^{-2}
σ^i	Charge density of specifically adsorbed ions, C cm^{-2}
σ^s	Total charge density at the double layer, C cm^{-2}
t	Time, s
T	Absolute temperature, °K
θ	Actual fraction of area covered by nucleation
θ_{ex}	Fraction of area covered by diffusion zones without overlapping
W	Frequency of attachment of atoms to the critical nuclei, s^{-1}
$X(N_{crit})$	Extension of excess free energy of creation, kJ, kJ mol^{-1}
Z_0	Zeldovic factor
β^*	charge transfer coefficient (dimensionless)
$\Phi(N_{crit})$	Excess free energy of creation of critical nuclei, kJ, kJ mol^{-1}
Φ	Specific boundary energy, kJ, kJ mol^{-1}
$\sum\psi_i$	Total binding energy of the cluster with the substrate, kJ, kJ mol^{-1}
Ψ_{kink}	Binding energy of a kink atom, kJ, kJ mol^{-1}

Abbreviations

AFM	Atomic Force Microscopy
CV	Cyclic Voltammetry
CA	Chronoamperometry
DSC	Differential Scanning Calorimetry
SEM	Scanning Electron Microscope
XRD	X-ray Diffraction

Chapter 1

Introduction

1.1. Background

When there is evidence that a bulk material will not meet an application requirement, a surface engineering process might be called upon to make the system work. The knowledge transfer from bulk materials to ***thin films*** has led to extensive developments, particularly relevant for the design of novel coatings in the field of surface engineering. Thin films show different physical properties because of many factors such as smaller size of the crystallites and in particular many crystallographic defects such as dislocations, vacancies, stacking faults, grain boundaries and twins which are in different degrees and orders [1]. The enthusiasm to manipulate the structure of the deposited films has further provided an impetus for bridging the fields of ultrafine-structured materials and thin films. Thus, in order to grow these films in a very reproducible manner with desired structure and stoichiometry, it is very important to study their deposition, structure, growth and properties in a detailed manner and then be able to predict the optimal conditions for a particular deposition technique. Many deposition techniques have evolved over the years to deposit thin films which are perfect, both chemically and structurally. The more important thin film processes are vacuum based techniques including PVD, CVD and MBE [2]. The electrodeposition of thin films is a viable alternative to vacuum-based deposition processes. Versatility, relative ease of fabrication and transfer from liquid phase to solid phase, convenience of scale-up and economy are the advantages of the electrodeposition approach to advanced material synthesis.

Electrochemistry, has been around for a very long time now; so why should curious scientists and technologists still get excited by it? Its versatility in the whole spectrum of materials research, from material synthesis to analysis and gradual powerful renovations of the field have attributes that make it so unabated. For example, photo-excitation (photo-electrochemistry) and vibration of the electrochemical cell (*by ultrasound* or by magnetic field) have standing concepts with enough scientific entanglements to work for. Its major advantage is its simplicity, that processing can take place at room temperatures and pressures, and hence film properties can be easily controlled [3,4]. To obtain fine grained depositions from the electrolytic bath, a prerequisite step is to maintain a high supersaturation of the depositing ions near the electrode surface. And there may be two possibilities for meeting the supersaturation condition i.e. either to increase the electrochemical overpotential/current/quantity of electricity or the activity of ions by the non-electrical variables inside the solution. While the phenomenon of overpotential driven supersaturation is quite an established field, the activity driven supersaturation theories are still unexplored and under scientific conflictions. One such approach may be in the direction of lowering the temperature of the electrolyte to enhance the nucleation phenomenon driven by temperature-induced supersaturation.

We can do amazing things with thermal energy, such as moving matter around within a solid without risking melting or changing the basic shape of a component. On the other hand, it can be a real nuisance. It can make magnetic disks 'forget'. It can leave materials 'sapped' of their strength. Just a few degrees of temperature change can make some things unrecognisably different. So, the issue needs to be known about, 'What if the ***temperature*** changes?' is an excellent prompt for engineers. At low temperature**,** the population of critical clusters increases whereas the rate of attachment of further atoms to the cluster decreases due to increased diffusion barrier [5]. Hence temperature can affect the crystal growth by several ways, all of them predominantly resulting in a smaller crystal size at low temperatures.

The literature covering the low temperature electro-depositions, however have descriptions on crystal morphology and less on the surface coverage aspects and electrochemical analysis. To acquire uniform thickness, adhesion, morphology and other properties, there is an urgent need of uniform deposition. Hence, the electrochemical system at low temperature needs to have an activation to compliment the deposition mechanism to comply the above requirements. Coupling ultrasound to electrochemistry, ***sonoelectrochemistry***, has long been acknowledged towards this respect [6,7]. Molecules hence undergo reactions due to the application of powerful ultrasound radiation (20 kHz–10 MHz). The physical phenomenon responsible for the sono-electrochemical process is acoustic cavitation: creation and collapse of microscopic bubbles inside the liquid medium. The heating and cooling rates during cavitation are more than a billion degrees centigrade per second [6,7]. This is similar to the cooling that occurs if molten metal is splattered onto a surface cooled near absolute zero.

Hence, exploring the classical science of temperature at sub-ambient ranges in sono-electrochemical way may lead surface engineers towards a technology revolution.

1.2. Research motivation

Many approaches have been made to electrodeposit ultrafine grained thin films [8-10]. Recent developments in use of low bath temperature [10] were an impetus behind this work. Although this approach is very convincing and has been successful in many respects, it has been found to be ambiguous in some cases e.g. Elsentriecy *et. al.* [11] have observed coarse grained coatings at low deposition temperatures. However, most of the studies in the open literature are limited to morphological and structural investigations and a very little attention has been given to understand the electrochemical crystallization mechanism.

Consequently, the sole impact of this parameter on deposition mechanism, structure and properties of the deposits is not yet completely understood. Hence an establishment on complete analysis would allow more insight into electrochemical process and a wider range of conditions to be investigated. This is one of the objectives of the current study. It begins with the analysis of structure and surface morphology of the deposits and subsequently extends to the copper nucleation mechanisms in presence and absence of ultrasound at low deposition temperatures. The model of Cu^{2+} reduction in the presence of ultrasound at low temperatures accounts for the effects of decreased surface roughness, change in grain habitat and better deposit/substrate interface properties, something which has not been previously investigated.

1.3. Objectives

The overall objectives to be achieved in the present study are:

- To investigate the effects of low temperature and sonication on the structure and morphology of the copper deposits.
- To explore the alterations in nucleation mechanisms in deconvulated conditions of sonication and low temperature, and also in the coupled condition.
- To study the properties of the deposited films including residual stress, hardness, elasticity and surface adhesion. Emphasis has also been given to the ex-situ non-isothermal growth behavior of the films after deposition.
- To observe the change in structure and properties of the films with the change of the depositing substrate material.

The following processes and procedures have been carried out to meet the objectives:
Copper was electroplated from a simple binary sulfate electrolyte onto graphite substrates. The structural information was obtained by X-ray diffraction, SEM and AFM. Nucleation and growth analysis was done by the single step potential technique. The kinetics of the phase formation was obtained by cyclic voltammetry. After the deposition, the intrinsic stress developed during the deposition process was measured by using the curvature analysis method. By nano-indentation technique the hardness and elastic properties were obtained. The post synthesis growth analysis was done by a systematic correlation of the thermal analysis data (by DSC) with the surface morphological evolution and surface energy variation for the deposits before and after synthesis. Finally the effect of substrate was investigated by deposition and subsequent characterization of the copper films on aluminum substrate.

1.4. Structure of the dissertation

This thesis is organized into 5 chapters and 1 appendix. In Chapter 2, general aspects of thin film technology and electrodeposition are introduced. An approach has been presented to assess the possible effects of temperature and sonication on the nucleation and growth mechanism and hence on the structure and properties of the films.

Furthermore electrochemical methods of analysis of nucleation phenomena and reaction kinetics have also been included in the chapter.

Chapter 3 describes about the experimental details of processing technique: ultrasonic cell arrangements and electrolyte selection and characterization and property analysis techniques: X-ray diffraction, scanning electron microscopy, atomic force microscopy, differential scanning calorimetry, nanoindentation, stylus surface profilometer and contact angle measurement.

Chapter 4 includes the results of voltammetry, single step potential, micrsotrutural, phase, mechanical and thermal experiments to study the effects of both the parameters. The first section deals with the phase, structure and compositional variations of the films due the impact of the experimental condition. The evolution of nucleation mechanisms governing the changes in section 1 of this chapter is given in the next section. Section 3 covers impacts on mechanical properties and residual stress. In section 4 the non-isothermal ex-situ growth behavior of the films is presented. The final section includes the alteration in structure and properties by changing the depositing substrate.

A summary of the contributions of this study are presented in Chapter 5.

Film thickness calculation from the total charge consumed in the due process of deposition, curvature method of stress analysis and force-displacement curve analysis for surface adhesion measurement is presented in the Appendix.

1.5. References

1. M. Ohring, The Materials Science of Thin Films, Academic Press, London, UK, 1992.
2. Handbook of thin films.
3. C. M. O. Brett, A. M. O. Brett, Electrochemistry: Principles, Methods and Applications, Oxford University Press, Oxford, 1994.
4. U. Erb, Nanostructuted Materials, 6 (1995) 533.
5. I. V. Markov, Crystal Growth for Beginners, World Scientific Press, Singapore, 2004.
6. K. S. Suslick, Ed., Ulrrasound: Its Chemical, Physical, and Biological Eficts, Wiley VCH, Weinheim, 1988.
7. J. P. Lorimer, T. J. Mason, Electrochemistry, 67 (1999) 924.
8. T. Mahalingam, M. Raja, S. Thanikaikarasan, C. Sanjeeviraja, S. Velumani, H. Moon, Y. Deak Kim, Material Characterization, 58 (2007) 800.
9. E. Go´mez, Jose´ Garcı´a-Torres, E. Valle´s, J. Electroanal. Chem. 594 (2006) 89.
10. L. Zhang, Z. Chen, Y. Tang, Z. Jia, Thin Solid Films, 492 (2005) 24.
11. H. E. Elsentriecy, K. Azumi, H. Konno, Electrochim. Acta, 53 (2008) 4267.

Chapter 2

Literature link

This chapter discusses briefly the important aspects of thin films. Section 2.1. is a summary of evolution of thin films from surface engineering, their deposition methods and important issues. Section 2.2. highlights the fundamental aspects of electrochemical deposition highlighting the effect of temperature on the phase formation. The field of sonoelectrochemistry has been discussed in section 2.3. Literature covering the temperature and sonication effects on the structure and morphology of the deposits and nucleation mechanisms, residual stress and mechanical properties has been covered in their respective results and discussion sections.

2.1. Thin film technology

The recognition that one might protect a surface from environmental attack, by application of an organic, inorganic or metallic coating, so extending the life of not just the surface, but the entire component or equipment, was one of the major advances in the history of technology i.e. surface engineering. The most common reasons for altering the surface are to improve corrosion resistance, control friction and wear, alter dimension or to alter physical properties (reflection, color, conductivity). As applied to materials, surface engineering may be coatings or special surface treatments including processes such as diffusion treatments, selective hardening, plating, hard-facing, thermal spray coatings, high-energy treatments such as laser processing, and organic coatings such as paints and plastic laminates [1-5]. Involvements with coatings dates to the metal ages of antiquity in gold beating and gilting [6,7] and can be said to have transformed itself within a few decades from what was mainly an empirical craft, into a key technology, grounded on scientific principles [8-10]. The advances in coatings have two approaches either in tailoring the microstructure or the thickness. The complexity of the tribological properties of materials and the economic aspects of friction and wear justify an increasing research effort in bridging the fields of ultrafine-structured materials and coatings.

This section is written based on the unpublished article

A. Mallik, B. C. Ray, Evolution of principle and practice of electrodeposited thin film: A review on effect of temperature and sonication, **International Journal of Electrochemistry (In press).**

Talking about thin films, these are the coatings with the thickness value below 1 μm and widely used in microelectronics, optics and solar cell systems [11-17]. Thin film systems necessitate direct control of materials on the molecular and atomic scale, including surface modifications, deposition and structuring. There exists a huge variety of thin film deposition processes and technologies which originate from purely physical or purely chemical processes. However deposition processes for applications in advanced microelectronics and surface engineering processes will require the most demanding approaches in the near future. The more important thin film processes are based on liquid phase chemical techniques, gas phase chemical processes, glow discharge processes and evaporation methods [18]. Typical processes are e.g. ion beam assisted deposition (IBAD) and plasma enhanced chemical vapor deposition (PECVD). Examples for novel thin film processing techniques, which are still under development, are pulsed laser ablation (PLD) and chemical solution deposition (CSD). Both techniques enable the synthesis of complex thin film materials (complex oxides, carbides, and nitrides). The electrodeposition of thin films is a viable alternative to vacuum-based deposition process, such as sputtering, plasma deposition, or chemical vapor deposition. Its major advantages are its simplicity, that processing can take place at room temperatures and pressures, and that thin film properties can be controlled [19-21].

The next section deals with the electrochemical deposition mechanism (electrocrsytallization) which also includes approaches to understand the process towards fabrication of fine grained films.

2.2. Electrochemical deposition

The field of electrochemistry encompasses a massive array of different phenomena (e.g., electrophoresis and corrosion), devices (electrochromical displays, electro analytical sensors, batteries, and fuel cells), and technologies (the electroplating of metals and the large-scale production of aluminum and chlorine) [22-25].

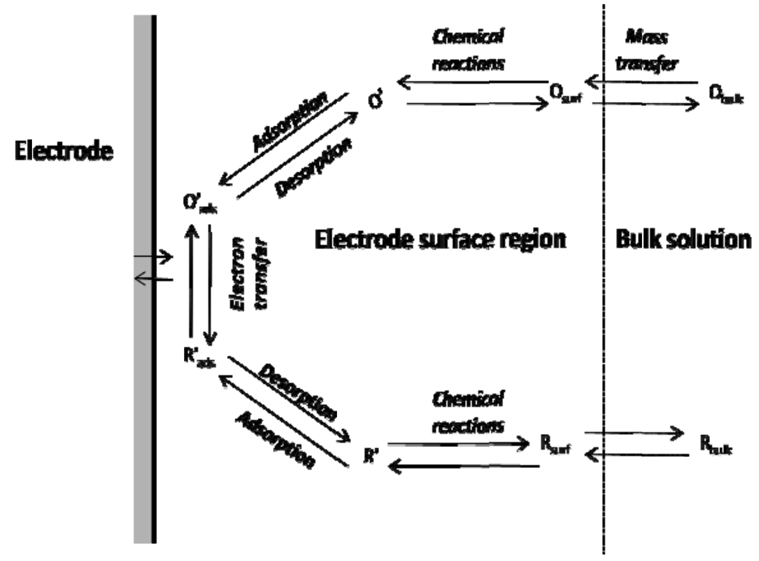

Fig.2.1. Pathway of a general electrode reaction

The technology of electrochemical deposition of metals and alloys involves the reduction of ions from aqueous, organic, and fused salt electrolysis. The deposition of material species involves reduction of ions in the solution as, $M_{Sol}^{Z+} + Ze \rightarrow M_{lattice}$. The seemingly simple single reaction needs pre- and post-complex steps [19,26] before contributing to the whole deposition process as depicted in fig. 2.1. This is a reaction of charged particles at the interface between a solid metal and a liquid solution. The two types of charged particles, an ion and an electron, can cross the interface. Hence four types of fundamental areas are involved in the due process of deposition: (1) electrode-solution interface as the locus of deposition process, (2) kinetics and mechanism of the deposition process, (3) nucleation and growth processes of the deposits and (4) structure and properties of the deposits. The consecutive sections are addressed to above points and every facet has been discussed briefly.

2.2.1. Electrode solution interface

The interface between the electrode and the electrolyte is the heart of electrochemistry. It is the place where charge transfer takes place, where gradients in electrical and chemical potentials constitute the driving force for electrochemical reactions. Electrodeposition processes occur in this very thin region, where there is a very high electric field (10^6 or 10^7 V/cm). The classical approach describes the electric double layer (EDL) of a metal electrolyte interface by a plate condenser of molecular dimensions [19,27]. One plate is the metal surface with its excess charge, the other is formed by the solvated ions at closest approach. The solvated ions that form the outer Helmholtz plane (OHP) and that are held in position by purely electrostatic forces are termed as nonspecifically adsorbed. These are mainly solvated cations. Because of thermal agitation in the solution, the non-specifically adsorbed ions are distributed in a three dimensional region called the diffuse layer: which extends from OHP to the bulk of solution. The excess charge density in the diffuse layer is σ^d (μC/cm^2).

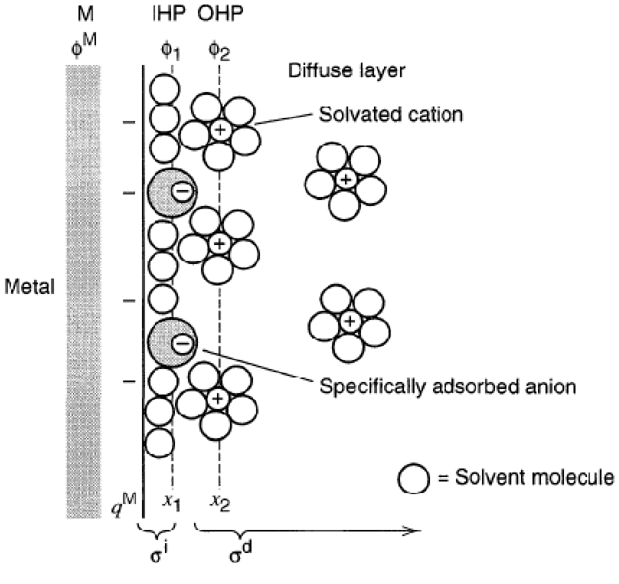

Fig.2.2. Double layer region at the electrode/electrolyte interface

Most anions however give away part of that solvation shell when entering the double layer to form a chemical bond with the electrode surface. These ions are termed specifically adsorbed and their centers form the inner Helmholtz plane (IHP). The total charge density from specifically adsorbed ions in this inner layer is σ^i, hence the total excess charge density on the solution side of the double layer, σ^s is given by:

$$\sigma^s = \sigma^i + \sigma^d = -\sigma^m \quad (2.1)$$

The thickness of the diffuse layer depends on the total ionic concentration in the solution; for concentrations greater than 10^{-2} M, the thickness is less than ~100 A°. The potential profile because of the charge density variation is also shown in the fig. 2.2. The capacitance and the charging currents in the electrochemical system can either be measured by a potential/current step or by ramping the voltage.

2.2.2. Thermodynamics and kinetics of deposition mechanism

2.2.2.1. Nucleation work

In the formation and growth of adion clusters, two processes are of fundamental importance: (1) the arrival and adsorption of ions (atoms) at the surface, and (2) the motion of these adsorbed ions (adions, adatoms) on the surface [19,27]. An adion deposited on the surface of a perfect crystal stays on the surface as an adion only temporarily since its binding energy to the crystal is small. It is not a stable entity on the surface, but it can increase its stability by formation of clusters. For the formation of a cluster of N ions, the Gibbs free energy, ΔG(N) has two components [28,29]:

$$\Delta G(N) = -N\Delta\mu + \emptyset(N) \qquad (2.2)$$

Where the first term is related to the transfer of N ions from a supersaturated (Δμ) solution to the crystal phase and the second term is related to the increase of the surface energy due to creation of the surfaces of a cluster. The transfer of ions is purely a thermodynamic conceptual origin. Under the state of thermodynamic equilibrium in an electrochemical system comprising metal ions in solution, metal adatoms on an electrode and metal atoms in the deposit, the system is stable. The formation, growth or dissolution of a phase cannot occur in this situation. Favorable conditions for a first order phase transition i.e. for metal ions discharging either on the crystal or on the substrate, occur when the solution is supersaturated [20]. This means that the electrochemical potential of the electrochemically active species in the parent phase (the electrolyte 8olution) is larger than the electrochemical potential of the bulk metal. That being the case, the difference $\Delta\mu = \mu^{sol} - \mu^M > 0$ defines the electrochemical supersaturation, which is the thermodynamic driving force and the reason for the nucleus formation to be connected with the overcoming of an energy barrier for the phase transition. Thus the interrelation between the supersaturation ($\Delta\mu$) and the size of the critical nucleus (N_{crit}) will decide the lowest Gibbs energy of phase formation (ΔG_{crit}) and highest rate ($J = A_J \exp\left(-\frac{\Delta G_{crit}}{BT}\right)$) of cluster formation [20,30] at a fixed set of temperature (T) and pressure. B is Boltzman constant. Different approaches have been established for the estimation of the parameters depending upon the size of the clusters.

If adsorption, diffusion and binding of the clusters are not the limiting factors (for sufficiently large clusters) than ΔG_{crit} will have a value [29]:

$$\Delta G_{crit} = \frac{\Delta\mu N_{crit}}{\gamma-1} = \frac{1}{\gamma}\varphi X(N_{crit}) = \frac{1}{\gamma}\emptyset(N_{crit}) \qquad (2.3)$$

Where γ is the dimensionality of the cluster and φ is specific boundary energy. For small crystals with the dominant effect of binding energies of adatom with substrate as well as bulk phase may have an expression for ΔG_{crit}:

$$\Delta G_{crit} = \Delta\mu(N_{crit} + \beta^*) - \sum\Psi_i - N_{crit}(\Psi_{kink} + \varepsilon) \quad (2.4)$$

Where β^* denotes the charge transfer coefficient, Ψ_i is the binding energy, Ψ_{kink} is the binding energy of a kink atom and ε is the average strain energy per atom. Hence, irrespective of the size of the initial critical nuclei, the increase in supersaturation will explicitly follow a decreasing N_{crit} trend. Furthermore in a macroscopic scale, Kardos and foulke [31] distinguish three possible mechanisms for improved smooth and bright electrodepositions: true leveling, grain refining and randomization of crystal growth. The indiscriminate deposition on all available surface sites unlike the selective one, on favorable kinks, steps and the ends of screw dislocations may fulfill the requirements. One of the approaches for such requirements in the process is to employ sufficient supersaturation, by varying both the external and internal deposition parameters.

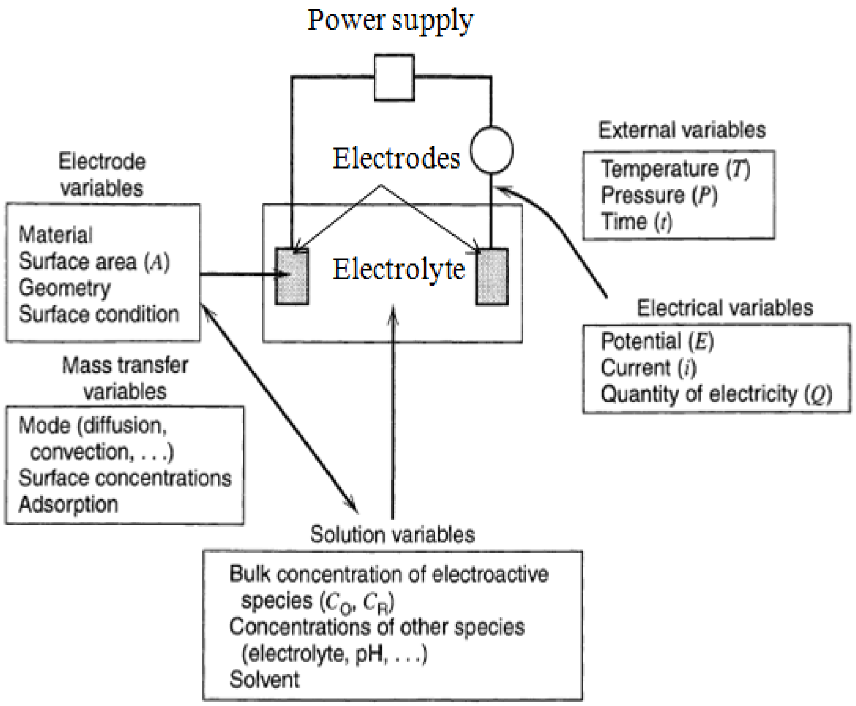

Fig.2.3. Variables affecting electrochemical phase formation

Hence, to discuss how the electrolyte can get supersaturated, an idea of possible electrochemical variables which can contribute to the factor need to be known. The parameters of importance in electrochemical cells are shown in fig. 2.3. All these variables can be categorized into two broad groups, electrical and non-electrical parameters. Hence there may be two possibilities for meeting the supersaturation condition i.e. either to increase the electrochemical overpotential/current/quantity of electricity or the activity of ions by the non-electrical variables inside the solution. While the phenomenon of overpotential driven supersaturation is quite an established field, the activity driven supersaturation theories are still unexplored and under scientific conflictions. One such approach may be in the direction of lowering the temperature of the electrolyte to enhance the nucleation phenomenon driven by temperature induced supersaturation. The following section will discuss so.

2.2.2.2. Effect of temperature

It is scarcely surprising that, as the temperature is varied within the wide range available, the properties of all materials undergo very considerable modifications. Hence there are fundamental, analytical and technological reasons for wanting to extend this temperature range in venturing the relatively unexplored technology associated with the science [32,33]. The technology of low temperature has the aspects of cryo-physics, cryo-bilology, cryo-surgery, cryo-electrochemistry and so on in the discipline [34-36]. Since the date of experimentation on cryo-electrochemistry, there has been renewed interest for the field towards intermediate electrode reactions, electrformation and electranalysis [37,38] to characterize the temperature dependent electrode processes that are often of interest themselves, these include: standard electrode potentials, activity coefficients, conductance measurements, equilibrium constants, diffusion activation constants, the electrodeposition of metals and alloys. Covering all these aspects is beyond the scope of the present research and concentration is now on low temperature electrodeposition.

The thermodynamics and kinetics of the electrochemical phase formation may depend on a number of factors. And the existence of an energy barrier makes nucleation a probability process [20,39], with a rate

$$J_0 = Z_0 W \lambda^{-1} \exp\left[\frac{-\Delta G_{crit}}{kT}\right] \qquad (2.5)$$

Where, Z_0 /cm^{-2} is the number density of active sites on the substrate, W /s^{-1} is the frequency of attachment of single atoms to the nucleus and λ^{-1} is a non-dimensional quantity accounting for the difference between the quasi-equilibrium and the stationary number of nuclei, ΔG_{crit} is the maximum energy barrier at a critical cluster size N_{crit}, k and T have their usual meanings. From the expression it can be observed that the energy barrier which has to surmount for an adatom formation by the ions is an obvious function of temperature. Alterations in the temperature range used may affect the kinetics in the following way. Decreasing temperature increases the level of supersaturation. Hence, the activity of ions will increase and the critical nucleating condition will occur at low temperature. The relationship between morphology and degree of supersaturation is an open area of research. However supersaturation determines the degree of metastability in the parent phase. To relate the non-equilibrium cluster energetic and fluctuational growth to the rate of nucleation, it is necessary to describe the cluster population distribution.

The metastable equilibrium concentration of critical clusters of a given size, C_N, is then [40]:

$$C_n = C_l \exp\left[\frac{-\Delta G}{kT}\right] \qquad (2.6)$$

Where, C_l is the number of atoms per unit volume in the liquid. Thus a high nucleation rate can be achieved at low temperature. The growth of clusters past the critical size can be represented kinetically [44,45] as:

$$J = \nu_{SL} S_{crit} C_n = \nu \exp\left[\frac{-\Delta H_d}{kT}\right] S_{crit} C_l \exp\left[\frac{-\Delta G}{kT}\right] \qquad (2.7)$$

Where, ν_{SL} is the jump frequency of atoms form the liquid to the critical cluster (It can be estimated from lattice vibration frequency ν and activation energy barrier for interfacial diffusion ΔH_d), S_{cr} is the number of atoms surrounding a cluster and C_n is the number of critical clusters. At low temperature**,** the population of critical clusters increases whereas the rate of attachment of further atoms to the cluster decreases due to increased diffusion barrier. Hence temperature can affect the crystal growth by several ways, all of them predominantly resulting in a smaller crystal size at low temperatures [20,39].

The literature covering the low temperature electro-depositions, however have descriptions on crystal morphology and less on the surface uniformity aspects and electrochemical analysis. To acquire uniform thickness, adhesion, morphology and other properties, the uniform spreading of the grains in the deposit is imperative. Hence, the electrochemical system at low temperature needs to have an activation to compliment the deposition mechanism to comply the above requirements. Coupling ultrasound to electrochemistry, sonoelectrochemistry, has long been acknowledged towards this respect. A brief review of the mechanism and effects of the parameter is covered in the following section.

2.3. Sonoelectrochemistry

The benefits of coupling ultrasound to electrochemical processes have been recognized and explored for a long time [41-48]. The complexity of the processes induced by power ultrasound [49,50] and the sensitivity of results on conditions and experimental parameters [51] have hitherto prevented ultrasound in electrochemistry, or sonoelectrochemistry, from becoming a reliable and established tool. However, the use of ultrasound in a reaction system provides specific activation based on a physical phenomenon: acoustic cavitation. Cavitation occurs from the alternating longitudinal sound wave creating pressure variations within the liquid media in which the activation of preexisting nuclei form stable or transient bubbles or voids in the liquid structure [52]. Fig. 2.4 shows a representation of cavitation. Noltingk and Neppiras characterized a particular type of cavitation in which small bubbles in strong acoustic fields undergo growth to many times their original size and then subsequently undergo rapid collapse [53]. The bubble serves to concentrate the acoustic energy whereby the growth phase is isothermal with the collapse being adiabatic. This is termed transient cavitation which is distinguished from the less energetic stable cavitation where the bubble pulsates about equilibrium over successive acoustic cycles.

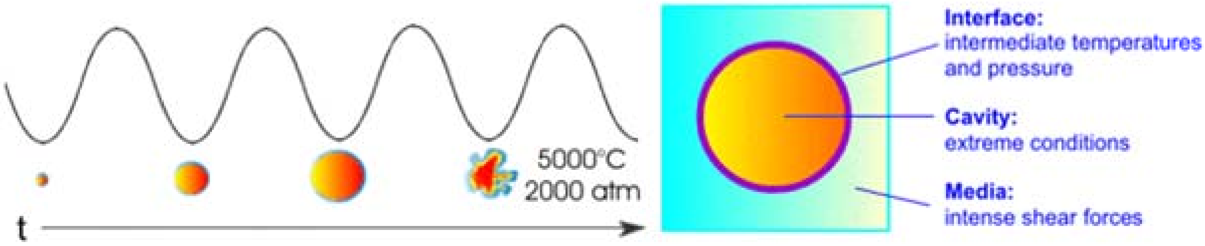

Fig. 2.4. Formation of a cavitation bubble by ultrasound

Because of the cavitation of the liquid, the lists of effects (fig. 2.5.) which can create unusual physical and chemical conditions [54,55] include (a) acoustic streaming: cavitation bubbles can oscillate around their resonant size and generate velocities that induce shear stresses. It is brought about by the momentum being absorbed by the liquid media, which manifests itself as turbulent flow in the direction of the applied sound field. This is a non-linear effect [56], which has been suggested to lead to local flow rates of more than 10 m s^{-1} [57]. Fig. 2.6 shows a typical flow pattern such as induced by a sonic horn operating at 20-40 kHz and located near a surface.

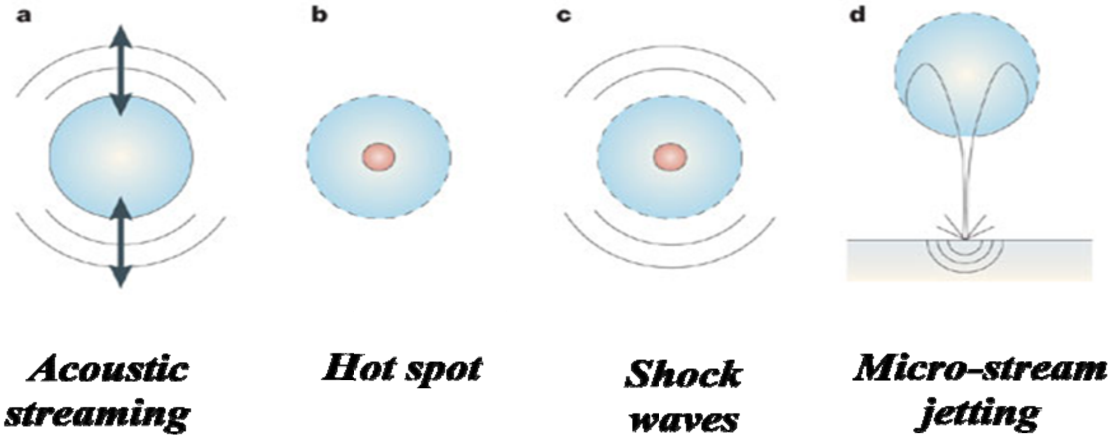

Fig. 2.5. Effects of acoustic cavitation in the liquid medium

(b) Hot spot: sudden collapse of bubbles generates momentary high temperatures and pressure in the bubble core. During transient cavitation, energy is focused within the bubble to generate [53,55,58] localized transient high temperatures and pressures estimated at temperatures of 5000 °C and pressures of 1700 bar with relatively low bulk temperatures.

For example, Suslick et al. showed that clouds of collapsing cavitation bubbles produced equivalent temperatures of roughly 5000 °C, pressures of about 1000 atmospheres and heating and cooling rates above 1 010 K s^{-1} [54, 58]. Whilst these estimations may be approximate, experimental measurements suggest that these are not unreasonable and that even higher temperatures may be produced [59-63] in both multibubble and single bubble cavitation [64,65]. (c) Shock waves: sudden collapse of cavitation bubbles leads to the formation of shock waves. (d) Liquid microjets: collapsing bubbles near a surface experience non-uniformities in their surroundings that results in the formation of high velocity micro-jets. Cavitation at the solid-liquid interface occurs more readily than in bulk solution, where crevices and active sites exist where vapor bubbles readily form.When transient cavitation occurs near a solid surface such as an electrode, collapse becomes non-spherical driving a high speed jet into the surface [66,67]. This violent impact leads to surface cleaning, ablation, and/or fracture of the solid-liquid interfaces or acoustic emulsification for liquid-liquid systems.

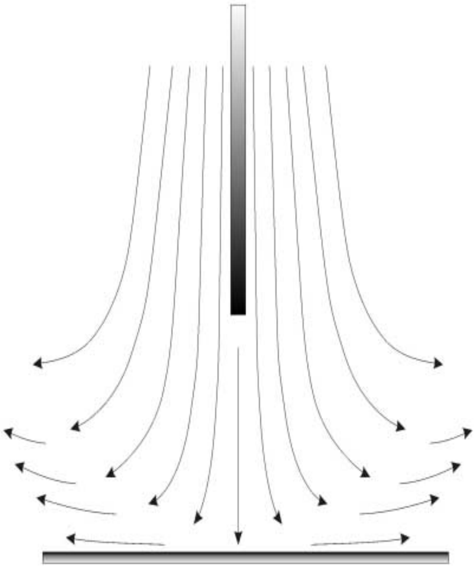

Fig. 2.6. Acoustic streaming: A typical flow pattern induced by a sonic horn

When applied to electrochemical experiments, ultrasound provides an increased mass transport regime in which the voltammetric response is qualitatively changed. This forced convection can be parameterized by assuming that ultrasonic application results in a truncated or thinned Nernst diffusion layer. The diffusion layer model (fig. 2.7) allows a naive description of the mass transport at the electrode interface by assuming a laminar sub-layer close to the surface and an approximately linear concentration gradient across a thin layer adjacent to the electrode.

Equation (2.8) best describes transport to an insonated electrode based on the uniformly accessible electrode model [57,68]:

$$I_{lim} = \frac{nFDAc_{bulk}}{\delta} \qquad (2.8)$$

where the limiting current, I_{lim}, is related to the number of transferred electrons, n, the Faraday constant, F, the diffusion coefficient, D, the electrode area, A, the concentration, c, and the diffusion layer thickness, δ. For a geometry in which the electrode is face-on to the horn in aqueous media it has been found experimentally that [69]: $\delta \propto D^{1/3}$.

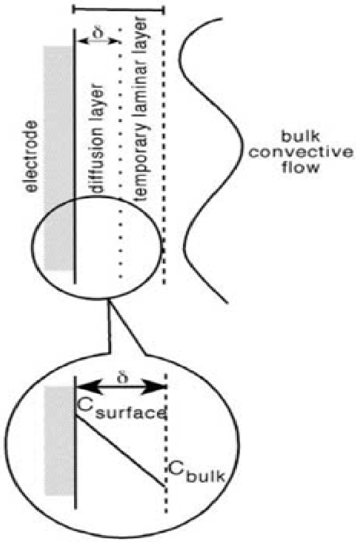

Fig. 2.7. Schematic representation of the diffusion and boundary layers at the electrode-solution interface as applied in the diffusion layer model

This is a general feature of convective systems and suggests that the diffusion layer is not purely stagnant as suggested by Nernst model but contains a convective component. Experiments conducted in a face on geometry [57] in aqueous solution have shown that: $\delta \propto D^{1/3}A[X]$, suggesting that an insonated system behaves as a hydrodynamic electrode [70]. Moriguchi [71] is thought to have first drawn attention to the fact that ultrasound decreases the thickness of the diffusion layer, although Marken et al. [57] and Cooper et al. [72] proposed independently that acoustic streaming provides the major contribution of the possible ultrasonic mechanisms on the rate of mass transport to an electrode.

Marken et al. [57] also showed that under extreme conditions that the minimum diffusion layer achievable in aqueous solution as thin as 0.7 µm (± 0.1 µm). In view of the above effects the ultrasound can have multiple impacts on the crystallization process as listed below.

2.3.1. Sonocrystallization

Crystallization under sonication may be referred as sono-crystallization. Using ultrasound to generate nuclei in a relatively reproducible way provides a well defined start point for the crystallization process, and allows the developer to focus on controlling the crystal growth for the remainder of the residence time in the crystallizer. This approach has been used successfully to manipulate crystal size distribution, solid-liquid separation behaviour, washing and product purity, product bulk density and powder flow characteristics. Hence ultrasound can be used beneficially in several key areas of crystallization such as [73-76]:

- Initiation of primary nucleation, narrowing the metastable zone width.
- Secondary nucleation.
- Crystal habit and perfection.
- Reduced agglomeration.
- A non-invasive alternative to the addition of seed crystal (seeding) in sterile environment.
- Manipulation of crystal distribution by controlled nucleation.

All these effects are function of ultrasonic parameters such as frequency of oscillations, intensity of irradiation and physical properties of the liquid such as degree of supersaturation and operating parameters such as temperature.

With a knowledge of the best possible effects of the two parameters on the deposition mechanism and hence the structure and properties of the films, the next section will cover the analytical electrochemical techniques used for both qualitative and quantitative analysis of the electrocrystallization phenomenon.

2.4. Nucleation and Growth analysis

The continued growth of nuclei of electrodepositing species can only take place by a Faraday process and the observed current is thus an exact measure of the combined rate of nucleation and growth of the mature nuclei or crystallites. A variety of current-potential-time relationships can be explored and any particular experiment can be exactly repeated many thousands of times to give the mean values and also the statistical variance of the results. Thus, either deterministic or stochastic descriptions of nucleation are amenable to experimental study by electrochemical means. The experimental study of electrochemical nucleation has been based on the observed response of a conducting substrate to a variety of imposed wave forms. Linear sweep voltammetry and cyclic voltammetry invariably indicate the presence of nucleation, mainly in a qualitative way. The current step method and most widely used single (and also the double) potential step potentiostatic are useful means of quantitative detection of the process of nucleation.

2.4.1. Cyclic Voltammetry (CV)

Cyclic voltammetry is a very versatile electrochemical technique which allows us to probe the mechanics of redox and transport properties of a system in solution [27, 77]. This is accomplished with a three electrode arrangement whereby the potential relative to some reference electrode is scanned at a working electrode while the resulting current flowing through a counter (or auxiliary) electrode is monitored in a quiescent solution. The technique is ideally suited for a quick search of redox couples present in a system; once located, a couple may be characterized by more careful analysis of the cyclic voltammogram. Usually the potential is scanned back and forth linearly with time between two extreme values – the switching potentials using triangular potential waveform (see fig. 2.8a).

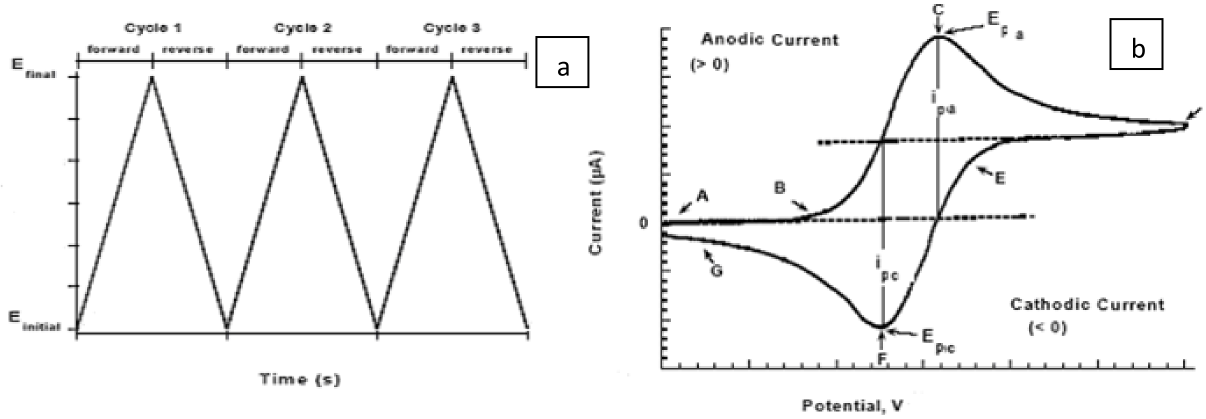

Fig. 2.8. (a) A cyclic voltammetry potential wave from with switching potentials and (b) the expected response of a reversible redox couple during a single potential cycle

A typical voltammogram is shown in fig. 2.8b. The scan shown starts at a slightly negative potential, *(A)* up to some positive switching value, *(D)* at which the scan is reversed back to the starting potential. The current is first observed to peak at E_{pa} (with value i_{pa}) indicating that an oxidation is taking place and then drops due to depletion of the reducing species from the diffusion layer. During the return scan the processes are reversed (reduction is now occurring) and a peak current is observed at E_{pc} (corresponding value, i_{pc}). The magnitude of the observed Faradaic current can provide information on the overall rate of the many processes occurring at the working electrode surface. As is the case for any multi–step process, the overall rate is determined by the slowest step. In general, the electrode reaction rate is governed by the rates of processes such as:

1) Mass transfer (e.g., of O from the bulk solution to the electrode surface).
2) Electron transfer at the electrode surface.
3) Chemical reactions preceding or following the electron transfer. These might be homogeneous processes (e.g., protonation or dimerization) or heterogeneous ones (e.g., catalytic decomposition) on the electrode surface.
4) Other surface reactions, such as adsorption, desorption, or crystallization (electrodeposition).

The simple electrodeposition reactions are far from the control of chemical and surface reactions, and the kinetics is mainly controlled by either by mass transport or charge transfer reactions. If, for example, an electrode process involves only fast heterogeneous charge-transfer kinetics and mobile, reversible homogeneous reactions, we will find below that (a) the homogeneous reactions can be regarded as being at equilibrium and (b) the surface concentrations of species involved in the faradaic process are related to the electrode potential by an equation of the Nernst form. The net rate of the electrode reaction, υ_{rxn} is then governed totally by the rate at which the electroactive species is brought to the surface by mass transfer, υ_{mt}: $\upsilon_{rxn} = \upsilon_{mt} = {}^{i}/_{nFA}$. Such electrode reactions are often called reversible or nernstian, because the principal species obey thermodynamic relationships at the electrode surface. If the overall reaction is not mass transport, then the sluggish electron transfer, irreversible will take the control of the kinetics. Since mass transfer and charge transfer play big role in electrochemical dynamics, we review here its three modes and begin a consideration of mathematical methods for treating them.

2.4.1.1. Reversible redox system

Mass transport processes are involved in the overall reaction. Mass transfer, that is, the movement of material from one location in solution to another, arises either from differences in electrical or chemical potential at the two locations or from movement of a volume element of solution. The modes of mass transfer are:

1) *Migration.* Movement of a charged body under the influence of an electric field (a gradient of electrical potential).
2) *Diffusion.* Movement of a species under the influence of a gradient of chemical potential (i.e., a concentration gradient).
3) *Convection.* Stirring or hydrodynamic transport. Generally fluid flow occurs because of *natural convection* (convection caused by density gradients) and *forced convection,* and may be characterized by stagnant regions, laminar flow, and turbulent flow.

Mass transfer to an electrode is governed by the Nernst-Planck equation*,* written for one- dimensional mass transfer along the x-axis as:

$$J_i(x) = D_i \frac{\partial C_i(x)}{\partial x} - \frac{z_i F}{RT} D_i C_i \frac{\partial \emptyset(x)}{\partial x} + C_i v(x) \qquad (2.9)$$

where $J_i(x)$ is the flux of species i at distance x from the surface, D_i is the diffusion coefficient, $dC_i(x)/dx$ is the concentration gradient at distance x, $\partial\phi(x)/\partial x$ is the potential gradient, z_i and C_i are the charge (dimensionless) and concentration of species i, respectively, and $v(x)$ is the velocity with which a volume element in solution moves along the axis.

For the oxidation reaction involving n electrons, $Red \rightleftarrows Ox + ne^-$: the Nernst Equation gives the relationship between the potential and the concentrations of the oxidized and reduced form of the redox couple at equilibrium (at 298 K):

$$E = E^{0'} + \frac{0.059}{n} log_{10} \frac{[Ox],}{[Red]} \qquad (2.10)$$

where E is the applied potential and $E^{0'}$ is the formal potential. Note that the Nernst equation may or may not be obeyed depending on the system or on the experimental conditions. Providing that the charge–transfer reaction is reversible, that there is no surface interaction between the electrode and the reagents, and that the redox products are stable (at least in the time frame of the experiment), the ratio of the reverse and the forward current $i_{pr}/i_{pf} = 1.0$ (in Fig. 2 $i_{pa} = i_{pf}$ and $i_{pc} = i_{pr}$). In addition, for such a system it can be shown that:

1) The expression of the peak current (A) for the forward sweep in a reversible system at 298 K is given by the Randles–Sevick equation:

$$i_{pf} = (2.69 \times 10^5) n^{3/2} A D^{0.5} v^{0.5} C^* \qquad (2.11)$$

where n is the number of electron equivalent exchanged during the redox process, A the active area of the working electrode, D and C^* is the diffusion coefficient and the bulk concentration of the electroactive species respectively and v is the voltage scan rate.

2) The corresponding peak potentials E_{pa} and E_{pc} are independent of scan rate and concentration,

3) The formal potential for a reversible couple $E^{0'}$ is centered between E_{pa} and E_{pc}:

$$E^{0'} = \frac{(E_{pa} + E_{pc})}{2} \; (2.12)$$

4) The separation between peaks is given by:

$$\Delta E_p = E_{pa} - E_{pc} = 2.3 \frac{RT}{nF} = \frac{59}{n} \text{ mV (at 25 °C)} \; (2.13)$$

for a n electron transfer reaction, at all scan rates. However, the measured value for a reversible process is generally higher due to uncompensated solution resistance and non-linear diffusion. Larger values of ΔE_p, which increase with increasing scan rate, are characteristic of slow electron transfer kinetics.

5) It is possible to relate the half-peak potential ($E_{p/2}$, where the current is half of the peak current) to the polarographic half-wave potential,

$$E_{1/2}: E_{p/2} = E_{1/2} \pm \frac{29}{n}\,\text{mV} \qquad (2.14)$$

The sign is positive for a reduction process.

6) The difference between E_p and $E_{p/2}$

$$E_p - E_{p/2} = (2.2\frac{RT}{nF}) = \frac{56.5}{n}\ \text{mV (at 25 °C)} \qquad (2.15)$$

2.4.1.2. Irreversible and quasi-reversible system

When the rate determining process is the charge transfer reaction the theory of metal deposition is based generally on the Butler-Volmer [78-81] equation giving the current density on a metal substrate as function of overvoltage η:

$$i = i_0\left[\exp\left(\frac{\alpha zF\eta}{RT} - \frac{(1-\alpha)z\alpha F\eta}{RT}\right)\right] = i_0 V(\eta) \qquad (2.16)$$

where i_o is the exchange current density and α is the charge transfer coefficient. For such irreversible processes (those with sluggish electron exchange), the individual peaks are reduced in size and widely separated. Totally irreversible systems are characterized by a shift of the peak potential with the scan rate:

$$E_p = E^0 - (RT/\alpha n_a F)[0.78 - \ln(k^0/D^{0.5}) + \ln\,(\alpha n\_a\, Fv)\ /\ RT)^{0.5}] \quad (2.17)$$

Thus, E_p occurs at potentials higher than E°, with the overpotential related to k° (standard rate constant) and α. Independent of the value k°, such peak displacement can be compensated by an appropriate change of the scan rate. The peak potential and the half-peak potential (at 25°C) will differ by 48/αn mV. Hence, the voltammogram becomes more drawn-out as αn decreases. The peak current, given by:

$$\boldsymbol{i_p = (2.99 \times 10^{0.5}) n(\alpha n_a)^{0.5} A C D^{0.5} v^{0.5}} \qquad (2.18)$$

where n_a is the number of electrons involved in the reaction. The current is still proportional to the bulk concentration, but will be lower in height (depending upon the value of α). Assuming α = 0.5, the ratio of the reversible-to-irreversible current peaks is 1.27 (*i.e.* the peak current for the irreversible process is about 80% of the peak for a reversible one). For quasi-reversible systems (with $10^{-1} > k° > 10^{-5}$ cm/s) the current is controlled by both the charge transfer and mass transport. The shape of the cyclic voltammogram is a function of the ratio $k°/(\pi v n F D/RT)^{1/2}$. As the ratio increases, the process approaches the reversible case. For small values of it, the system exhibits an irreversible behavior.

Overall, the voltammograms of a quasi-reversible system are more drawn out and exhibit a larger separation in peak potentials compared to a reversible system.

Unlike the CVs shown in fig. 2.8, certain cyclic voltammograms may have single or multiple crossover points in between forward and reverse scans as shown in fig. 2.9. The crossovers in cathodic and anodic branches are predominant in reversible systems involving undissolved products at cathode e.g. nucleation and growth of metallic deposits at cathode.

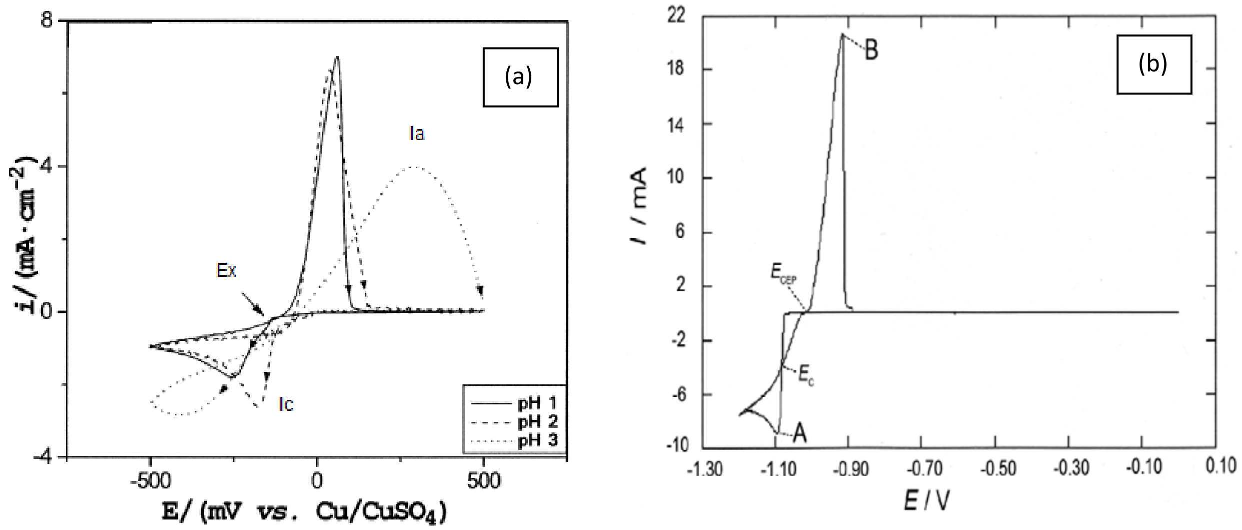

Fig. 2.9 Cyclic voltammograms with (a) single [83] and (b) double crossover potentials[84]

Deposition potential of metallic ions on a foreign substrate is usually higher than deposition potential on the electrode made of the same metal due to crystallographic substrate – metal misfit. Therefore, deposition on foreign electrodes commences at potentials that are more negative compared with the redox potential of M/M^{n+}. In the anodic direction, however, the oxidation of metal ion starts from the surface that already has deposited metal, resulting in a potential close to the M/M^{n+} equilibrium potential. Due to the difference in deposition and dissolution potentials, a crossover occurs between the cathodic and anodic current traces [82,83] at the crossover potential *Ex*. Hence the presence of the crossover is diagnostic for the nuclei formation on the electrode. Multiple crossover points may indicate nucleation mechanisms involving complex chemical reactions [84].

2.4.2. Potential step technique (Chronoamperometry)

Potentiostatic transients or chronoamperograms can be made the basis of the evaluation of induction times, nucleation rate constants, nuclear number densities and the mode of nuclei apperance. A typical chroamperogram or the current-time transient for nucleation with is shown in fig. 2.10. The principal nature of the transient is the falling current (I_{dl}) , then a rising section (I_{max}) and again a falling section corresponding to double layer charging, nuclei appearance on the substrate and the subsequent growth of electroactive area as established nuclei grow respectively. The earliest work on this 'constant overvoltage' for studying the nucleation and growth of electrodeposited materials were done by researchers such as

Fleischmann and Thirsk, and Pangarov [85,86]. The current-time transients they recorded showed maxima [87], followed by approximately exponential decay, which suggested that the nuclei were formed according to the equation:

$$\frac{dN}{dt} = AN_0 e^{(-At)} \qquad (2.19)$$

where t is the time since the potential was applied, N is the number of nuclei, N_0 is the saturation nucleus density (number of active sites) and A is the nucleation rate constant (a potential dependent constant with units of nuclei s^{-1}). This nucleation rate law is of great significance, as it is assumed as a basis for an entire family of more sophisticated models developed for the analysis of the process.

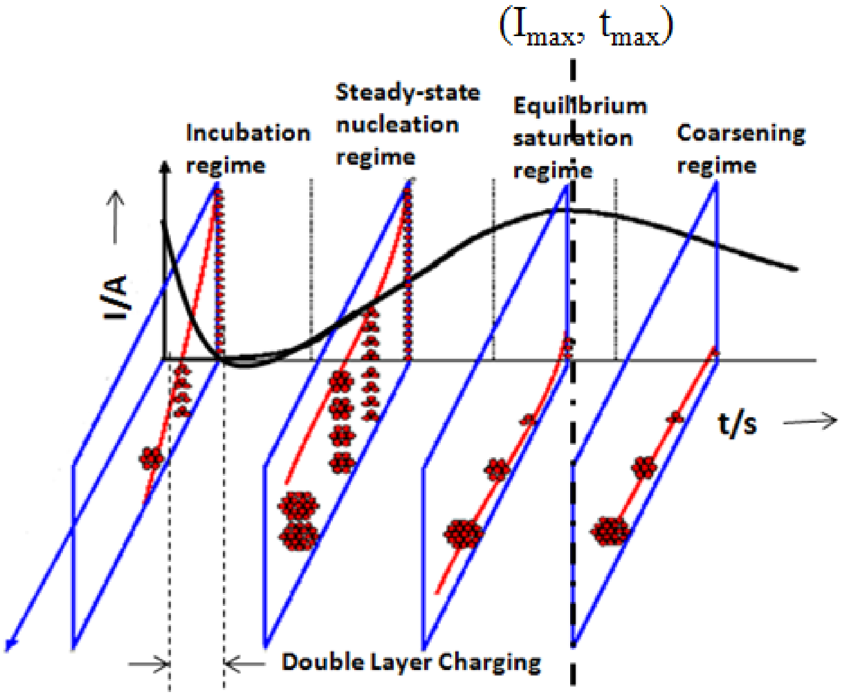

Fig. 2.10. A typical chronoamperogram

Theoretical modeling started with the estimation of nucleation current for a single spherical nucleus growing under planar diffusion [88] and then development and improvement of the models for multiple nucleations with overlapping diffusion zones. An excellent review covering all these models and the gradual development of new models can be followed in the ref [26]. However, all the modified theories could put light only on the decaying current tail of the transient (growth), nucleation current being unchanged. Hence, here we will describe the phase formation technique based on the SH model [89]. Their work lies on the simplification of the multidimensional diffusion field on the growing nuclei to two dimensional cases (fig. 2.11) and hence application of Avirami's theorem of phase formation can be feasible.

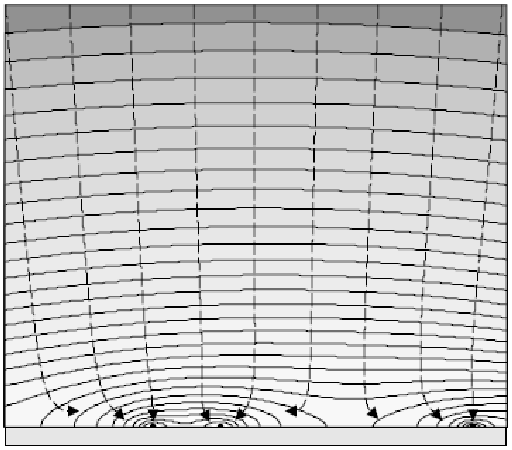

Fig. 2.11. Diffusion zones around growing nuclei

Table 2.1: Current expressions and their kinetic parameters from SH model [89]

Instantaneous nucleation	Progressive nucleation
$\boldsymbol{I = \frac{zFD^{1/2}c}{\pi^{1/2}t^{1/2}}[1 - \exp(-N\pi kDt)]}$	$I = \frac{zFD^{1/2}c}{\pi^{1/2}t^{1/2}}[1 - \exp(-AN_\infty \pi k' D^2/2)]$
$\boldsymbol{t_m = \frac{1.2564}{N\pi kD}}$	$t_m = (\frac{4.6733}{AN_\infty \pi k' D})^{1/2}$
$\boldsymbol{I_m^2 t_m = 0.1629(zFC)^2 D}$	$I_m^2 t_m = 0.2598(zFC)^2 D$

The theorem describes as:

$$\theta = 1 - e^{(-\theta_{ex})} \qquad (2.20)$$

Where θ is the actual fraction of surface covered and θ_{ex} is the fraction of area covered by diffusion zones without taking overlap into account, if the N centers are randomly distributed on the electrode surface. Avrami's theorem allowed Scharifker and Hills to relate the radial flux density through the real diffusion zones to an equivalent diffusive flux to an electrode of area A. By applying a mass/current balance and then integrating for the instantaneous or progressive cases, expressions can be derived for the total current with respect to time. The current expressions along with other kinetic parameter expressions are given in Table 2.1.

With this in mind, this section is an attempt to assess the current situation of the effects of different electrochemical parameters in both silent as well as ultrasound assisted electrodeposition, with a particular emphasis on the extraction of information about the nucleation process from electrochemical data in varying deposition temperatures. The morphological aspects and other properties will be discussed in the respective sections of study. In fact the effect of deposition potential on nucleation and growth mechanism takes the major share of reported open literature. Typical variation of current transients with this parameter in a diffusion controlled system follow trends as shown in fig. 2.12 [90].

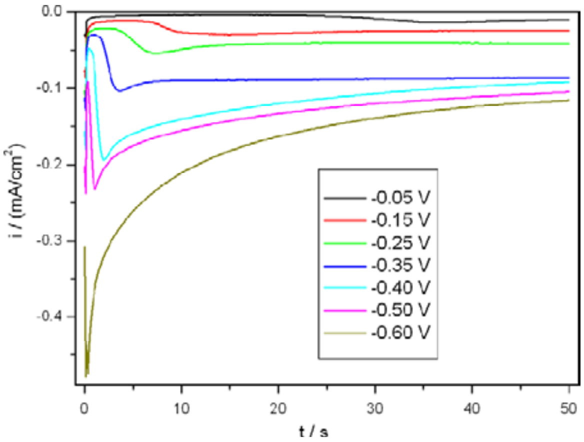

Fig. 2.12. Current–time transients for Se delectroeposition on SnO2-electrode from 0.5 mM H2SeO3 + 0.1 M LiCl solution at different potentials

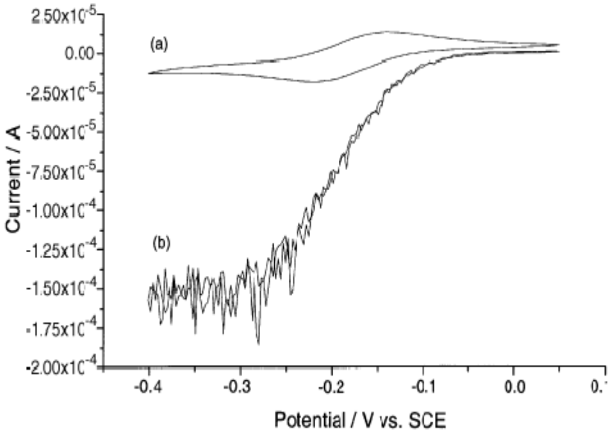

Fig. 2.13. Silent cyclic voltammogram (a) and sono-voltammogram (b) for the reduction of 1 mM $Ru(NH_3)_6^{3+}$ in aqueous 0.1 M KCl

The current reaches maximum and then starts decreasing as the diffusion fields of the nuclei overlap. The maxima are higher and occur at shorter times as the potential step increases suggesting that the number of active sites and nuclei increases with the potential. The transients are then fitted to available models for the type of assumed nucleation. To enlist few are: black and white Co deposition on steel [91] and Cu deposition on glassy carbon electrodes at extended overpotential region [92] and pencil graphite electrodes [93], it follows the response predicted for 3D instantaneous nucleation with diffusion control. The effect of the parameter on island growth has been reported by Guo et. al [94]. The effects of other parameters on the nucleation mechanism has also been reported but with less generalization. For example, pH of the depositing solution can affect the reaction mechanism by altering a mass controlled system to a mixed diffusion + ion transfer controlled regime [93]. Similarly increase in the discharging ion concentration, may transit an instantaneous nucleating system to a progressive one [93]. However the effect of temperature has rarely been studied on this context though some researchers have reported the variation of current observed under varying temperatures [95]. Reports on ultrasound assisted depositions, have mainly highlighted the final properties rather the process analysis. However sonication generally increases the analysis currents as shown in fig. 2.13 [96]. Though current transient in the sonication environment have been reported [97], the analysis of nucleation mechanism are far from conclusion.

2.5. Structure and Property correlation

As engineering coatings and thin films continue to increase in structural complexity and industrial importance, the need for accurate assessment of the mechanical and physical properties also increases. The deposition of such coatings inherently modifies the microstructure of the coating, resulting in mechanical properties of the coating that may differ significantly from those of the starting material from which the coating was produced [98,99]. In addition, residual stresses are often present in the film thickness and are strongly dependent upon deposition method and coating thickness [100,101]. These stresses can lead to failure of the component owing to cracking or interface delamination.

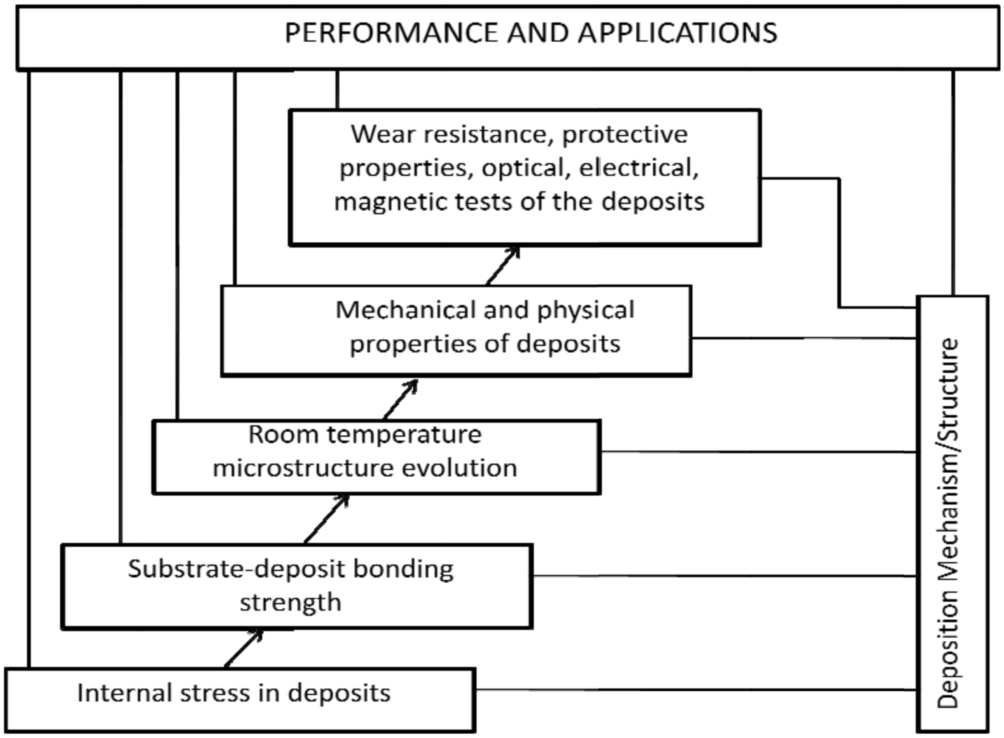

Fig. 2.14. Scheme of complex studies of the base metal-coating composition

Another parameter which may affect the final performance of the films is ex-situ growth of the grains. As-deposited, the film's grains are fine and equiaxial with a narrow statistical distribution of grain size; however, it is noted that the nano-sized as-plated grains are metastable even at room temperature. The grain size will increase to several microns over a period of time ranging from hours to weeks after deposition. This commonly observed phenomenon is variously referred to as self-annealing, room-temperature recrystallization or grain growth [102-104]. Since the grain size and texture of polycrystalline films have substantial impacts on their electrical and mechanical properties, it is therefore of scientific and technological interest to study the microstructural evolution of deposited films under different processing parameters.

It has been observed that phenomenon is very dependent on the deposition parameters, and, hence, on the microstructure of the as-deposited film. Thus, it is clear that in order to maximize coating performance, the microstructure evolution, stress state and mechanical properties of the coating must be well characterized. Comprehensive research of the base metal-coating composition is based on the interrelation of structure, properties and performance as shown in the figure below (fig. 2.14). When moving upwards from step by step, a researcher may consider each previous step as a basis for transition to the next, higher step bringing him closer to estimate the final performance.

2.6. Concluding remarks

Small is not only beautiful but also eminently useful. The burgeoning interest is amply justified, of course, by the unique properties of ultrafine grained materials and by the promises these systems hold as components of optical, electrical, opto-electrical, magnetic, magneto-optical, and catalytic sensors and devices. The synthesis of these materials for industry has resulted in a tremendous increase of innovative thin film processing technologies. Numerous methods have been applied to fabricate thin films. While each method has its advantages and disadvantages, electrochemistry has reached sufficient maturity and sophistication to be used for the deposition of fine-structured films. Fundamentally, electrodeposition can yield grain sizes in the nano-crystalline range when the electrodeposition variables (e.g. bath composition, pH, temperature, current density) are chosen such that nucleation of new grains is favourably enhanced in compared to the growth of existing grains. Size reduction of the crystals based upon low temperature of formation is fast becoming popular due to ‘clean’ synthesis. At low temperature**,** the population of critical clusters i.e. nucleation increases whereas the rate of attachment of further atoms (growth of nuclei) to the cluster decreases due to increased diffusion barrier. The aspects of low temperature electrochemistry did develop as cryo-electrochemistry [105]. Cryo-electrochemistry (at around −70 °C) however, has been limited to electrochemical analysis in non-polar solvents [106-108], and rarely been investigated for aqueous solutions and electrochemical synthesis. Studies have been limited to synthesis of insoluble products to as low as 10 °C [109]. The reports mainly have enlisted the effects of the parameter either on the morphological and property variations or the electrochemical analysis. Relation of the structural and morphological evolution with the nucleation mechanism is not clearly understood and therefore needs to be explored. Though nucleation will be favored at low temperatures of deposition, the film continuity may get impeded due to poor uniformity of the deposition. Synergistic interactions of ultrasound and low temperature can be apparent in this dearth in terms of good surface coverage, adherence, appearance and stability of films. Ultrasound has been found to be beneficial by (i) causing extremely fast mass transport, (ii) enhancing the mixing and dissolution kinetics at low temperature, and (iii) affecting the formation of solid products at the electrode surface. Experimental evidence of beneficial effects of ultrasound in low temperature electrochemical system has been proposed by various authors [110-112]. Like the silent processes at low temperature, these investigations have been restricted to processes involving the study of mass transport and cavitational effects of 20 kHz ultrasound in non-aqueous electrolytes. Some authors have also reported [113] the electrosynthesis at that low temperature, yet their work was mainly focused on electrochemical quantifications as the system of study was on a soluble final product.

However, to the best of our knowledge no specific prior work has been carried out on deposition formation at low temperatures, though ample literature is available on the effects of this parameter on structure and properties of deposits at room and high temperatures [114,115].

The pace and progress of developments is increasing a space in use of low bath temperature and ultrasound towards thin film synthesis are an impetus behind this work. Systematic complete investigation of nucleation and growth processes, solid state reactions, structural variation, the thermal and mechanical stability of thin film systems and phase boundaries is needed to improve the basic understanding of the process.

2.7. References

1. H. A. Jehn, Surf. Coat. Technol., 131 (2000) 433.
2. M. Zubielewicz, A. Królikowska, Prog. Org. Coat., 66 (2009) 129.
3. A. W. Ruff, K. G. Kreider, Wear, 203 (1997) 187.
4. J. W. Seok, N. M. Jadeed, R. Y. Lin, Surf. Coat. Technol., 138 (2001) 14.
5. A. Basu, J. Chakraborty, S. M. Shariff, G. Padmanabham, S. V. Joshi, G. Sundararajan, J. Dutta Majumdar, I. Manna, Scr. Mater., 56 (2007) 887.
6. L. B. Hunt, Gold Bull., 9 (1976) 24.
7. O. Vittori, Gold Bull. 12 (1979) 35.
8. L. I. Tushinsky, I. Kovensky, A. Plokhov, V. Sindeyev, P. Reshedko, Coated Metal: Structure and Properties of Metal-Coating Compositions, Springer, Germany, 2002.
9. F. C. Krebs, Sol. Energy Mater. Sol. Cells, 93 (2009) 394.
10. J. T. P. Derksen, F. P. Cuperus, P. Kolster, Prog. Org. Coat., 27 (1996) 45.
11. J. D. Ranacourt, Optical Thin Films, Macmillan Publishing Company, New York, 1987.
12. D. Lippkow, H.-H. Strehblow, Electrochim. Acta, 43 (1998) 2131.
13. H. Kubota, M. Sato, T. Miyazaki, J. Magn. Magn. Mater., 167 (1997) 12.
14. R. P. Ra€aellea, T. Potdevina, A. F. Heppb, S. G. Baileyb, Mater. Sci. Semicond. Process., 2 (1999) 289.
15. N. Nancheva, P. Docheva, M. Misheva, Mater. Lett., 39 (1999) 81.
16. N. A. Mohemmed Shanid, M. Abdul Khadar, Thin Solid Films, (2008).
17. I. Moreno, J. Jesus Araiza, M. Avendano-Alejo, Opt. Lett., 30 (2005) 914.
18. D. A. Glocker, S. I. Shah, Ed., Handbook of Thin Film Process Technology, Institute of Physics Publishing, Bristol and Philadelphia, 1998.
19. M. Paunovic, M. Schlesinger, Fundamentals of Eelectrochemical Deposition, Wiley Interscience, USA, 2006.
20. G. Staikov, A. Milchev, in: G. Staikov (Ed.), Electrocrystallization in Nanotechnology, Wiley VCH, Weinheim, 2007.
21. W. Schwarzacher, Electrochem. Soc. Interface, 15 (2006) 32.
22. D. D. G. Jones, H. G. Masterson, Advances in Corrosion Science and Technology, vol. 1, Plenum Press, 1970.
23. D. D. Macdonald, Modern Aspects of Electrochemistry, Vol. 11, Plenum Press, New York 1975.
24. J. L. Sudworth, Electrochemical Power Sources: Primary and Secondary Batteries, Peter Peregrinus, 1980.
25. D. Dobrev, J. Vetter, N. Angert, Nucl. Instrum. Methods Phys. Res., Sect. B, 149 (1999) 207.
26. M. E. Hyde, R. G. Compton, J. Electroanal. Chem., 549 (2003) 1.

27. J. Bard, L. R. Faulkner, Electrochemical methods: Fundamentals and applications, John Wiley and Sons, 2001, USA.
28. J.W. P. Schmelzer, Ed., Nucleation Theory and Applications, Wiley VCH, 2005.
29. E. Budevski, G. Staikov, W. J. Lorenz, Electrochim. Acta, 45 (2000) 2559.
30. J. W. Christian, The Theory of Transformations in Metals and Alloys, Pergamon Press, Hungary, 1975.
31. O. Kardos, D. G. Foulke, in: C. W. Tobais (Ed.), Advances in Electrochemistry and Electrochemical Engg., Vol. 2, Interscience, New York, 1962.
32. P. V. E. McClintock, D. J. Meredith, J. K. Wigmore, Matter at Low Temperatures, Blackie & Sons Limited, Glasgow, London, 1984.
33. G. G. Wildgoose, D. Giovanelli, N. S. Lawrence, R. G. Compton, Electroanalysis, 16 (2004) 421.
34. R. G. Chambers, Cryogenics, 1 (1960) 119.
35. I. Katkov, Int. J. Refrig., 29 (2006) 341.
36. N. N. Korpan, J. Surg. Res., 153 (2009) 1.
37. C. E. Banks, R. G. Evans, J. Rodrigues, P. G. Turner, T. J. donhoe, R. G. Compton, Tetrahedron, 61 (2005) 2365.
38. R. P. Van Duyene, C. N. Reilley, Anal. Chem., 44 (1972) 158.
39. I. V. Morkov, Crystal Growth for Beginners, World Scientific, Singapore, 1995.
40. J. H. Perpezko, in: D. M. Stefenescu (Ed.), Metals Handbook, Vol. 15, ASTM International, Ohio, 1988, p. 99.
41. N. Moriguchi, J. Chem. Soc. Japan, 5 (1934) 751.
42. R. Walker, in: T. J. Mason (Ed.), Advances in Sonochemistry, Vol. 3, JAI Press, 1993.
43. T. F. Connors, J. F. Rusling, Chemosphere, 13 (1984) 415.
44. R. Penn, E. Yeager, F. Hovorka, J. Acoust. Sot. Am. 31 (1959) 1372.
45. B, Gautheron, C, Degrand, G. J. Tainturer, J. Am. Chem. Soc., 197 (1985) 5579.
46. D. J. Walton, A. Chyla, J. P. Lorimer, T. J. Mason, G. Smith, Chem. Comm., (1989), 603.
47. D. J. Walton, S. S. Phull, in: T. J. Mason (Ed.), Advances in Sonochemistry, Vol. 4, JAI Press, 1996.
48. J. P. Lorimer, T. J. Mason, Electrochemistry, 67 (1999) 924.
49. K. S. Suslick (Ed.), Ultrasound: Its Chemical, Physical, and Biological Effects, Wiley VCH, Weinheim, 1988.
50. T. G. Leighton, The Acoustic Bubble, Academic Press. London, 1994.
51. B. Pugin, Ultrasonics, 25 (1987) 49.
52. P. R. Birkin, S. Silva-Martinez, J. Electroanal. Chem., 416 (1996) 127.
53. T. J. Leighton, Ultrason. Sonochem., 2 (1995) S123.
54. K. S. Suslick, W. B. McNamara III, Y. Didenko, in: L. A.Crum, T. J. Mason, J. Reisse, K. S. Suslick (Eds.), Sonochemistry and Sonolumincesence, Kluwer, Dordrecht, The Netherlands, 1999.
55. K. S. Suslick, Y. Didenko, M. M. Fang, T. Hyeon, K. J. Kolbeck, W. B. McNamara III, M. M. Mdleleni, M. Wong, Phil. Trans. R. Soc. Lond. A., 357 (1999) 355.
56. F. J. D. Del Campo, J. Melville, J. L. Hardcastle, R. G. Compton, J. Phys Chem. A, 105 (2001) 666.
57. F. Marken, R. P. Akkermans, R. G. Compton, J. Electroanal. Chem., 415 (1996) 55.
58. P. Cintas, J.-L. Luche, Green Chem., 1 (1999) 115.
59. D. F. Gaitan, L. A. Crum, J. Acoust. Soc. Am., 87 (1990) S141.
60. L. S. Berstein, M. R. Zakin, J. Phys. Chem., 99 (1995) 14619.
61. L. S. Berstein, M. R. Zakin, E. B. Flint, K. S. Suslick, J. Phys. Chem., 100 (1996) 6612.
62. F. Lepoint-Mullie, D. D. Pauw, T. Lepoint, P. Supiot, R. Avni, J. Phys. Chem., 100 (1996) 12138.
63. H. Y. Kwak, J. H. Na, J. Phys. Soc. Jpn., 66 (1997) 3074.
64. L. A. Crum, Phys. Today, 47 (1994) 22.

65. S. J. Putterman, Scient. Am., (1995) 46.
66. C. F. Naude, A. T. Ellis, J. Basic Eng., 83 (1961) 648.
67. L. A. Crum, J. Phys., 11 (1979) C8.
68. F. Marken, T. O. Rebbitt, J. Booth, R. G. Compton, Electroanalysis, 9 (1997) 19.
69. R. G. Compton, J. C. Eklund, F. Marken, T. O. Rebbitt, R. P. Akkermans, D. N. Waller, Electrochim. Acta, 42 (1997) 2919.
70. H. A. O. Hill, Y. Nakagawa, F. Marken, R. G. Compton, J. Phys. Chem., 100 (1996) 17395.
71. N. Moriguchi, J. Chem. Soc. Jap., (1934) 55.
72. E. L. Cooper, L. A. Coury Jr, J. Electrochem. Soc., 145 (1998) 1994.
73. R. Chow, R. Blindt, R. Chivers, M. Povey, Ultrasonics, 41 (2003) 595.
74. G. Ruecroft, D. Hipkiss, T. Ly, N. Maxted, P. W. Cains, Org. Process Res. Dev., 9 (2005) 923.
75. P. W. Cains, P. D. Martin, C. J. Price, Org. Process Res. Dev., 2 (1998) 34.
76. P. R. Gogate, R. K. Tayal, A. B. Pandit, Current Science, 91 (2006) 35.
77. P. M. S. Monk, Fundamentals of Electro-Analytical Chemistry, John-Wiley and Sons, 2008.
78. T. Erdey-Gruz, M. Volmer, Z. Phys. Chem. A, 150 (1930) 203.
79. T. Erdey-Gruz, M. Volmer, Z. Phys. Chem. A, 157 (1931) 165.
80. J. A.V. Butler, Trans. Farad. Soc., 19 (1924) 734.
81. J. A.V. Butler, Trans. Farad. Soc., 28 (1932) 379.
82. Southmpton Electrochemistry Group, in: T. J. Kemp (Ed.), Instrumental Methods in Electrochemistry, Ellis Horwood Ltd., Chicster, UK, 1985.
83. Darko Grujicic, Batric Pesic, Electrochim. Acta, 47 (2002) 2901.
84. Luis Humberto Mendoza-Huízar, Clara Hilda Rios-Reyes, María Guadalupe Gómez-Villegas, J. Mex. Chem. Soc., 53 (2009) 243.
85. N. A. Pangarov, S. Rashkov, Compt. Rend. Acad. Bulgare Sci., 13 (1960) 555.
86. N. A. Pangarov, S. Rashkov, Compt. Rend. Acad. Bulgare Sci., 13 (1960) 439.
87. M. Fleischmann, H. R. Thirsk, Trans. Faraday Soc., 51 (1955) 71.
88. D. J. Astley, J. A. Harrison, H. R. Thirsk, Trans. Faraday Soc., 64 (1967) 192.
89. B. R. Scharifker, G. J. Hills, J. Electroanal. Chem., 130 (1981) 81.
90. Y. Lai, F. Liu, Jie Li, Z. Zhang, Y. Liu, J. Electroanal. Chem., 639 (2010) 187.
91. E. Barrera, M. P. Pardavé, N. Batina, I. Gonzálezc, J. Electrochem. Soc. 147 (2000) 1787.
92. T. Zapryanova, A. Hrussanova, A. Milchev , J. Electroanal. Chem., 600 (2007) 311.
93. M.R. Majidi, K. Asadpour-Zeynali, B. Hafezi, Electrochim. Acta, 54 (2009) 1119.
94. L. Guo, P. C. Searson, Electrochim. Acta., 55 (2010) 4086.
95. Chun-Chen Yang, J. Power Sources 115 (2003) 352.
96. S. Floate, M. Hyde, R. G. Compton, J. Electroanal. Chem., 523 (2002) 49.
97. J. L. Hardcastle, G. Hignett, J. L. Melville, R. G. Compton, Analyst, 127 (2002) 518.
98. K. J. Van Vliet, A. Gouldstone, Surface Engineering, 17 (2001) 140.
99. D. A. Hardwick, Thin Solid Films, 154 (1987) 109.
100. G. C. A. M. Janssen, Thin Solid Films, 515 (2007) 6654.
101. W.D. Nix, B.M. Clemens, J. Mater. Res., 14 (1999) 3467.
102. M.T.P. Prado, J. J. Vlassak, Scripta Mater., 47 (2002) 817.
103. V.A. Vasko, I. Tabakovic, S.C. Riemer, Electrochem. Solid-State Lett., 6 (2003) C100.
104. H. Lee, S.S. Wong, S.D. Lopatin, J. Appl. Phys., 93 (2003) 3796.
105. D. K. Gosser, Q. Huang, Journal of Electroanalytical Chemistry, 267 (1989) 333.
106. T. J. Donohoe, D. J. Johnson, R. G. Compton, J. D. Wadhawan, Tetrahedron, 60 (2004) 5945.
107. N. Fietkau, C. A. Paddon, F. L. Bhatti,T. J. Donohoe, R. G. Compton, J. Electroanal. Chem., 593 (2006) 131.
108. C. A. Paddon, F. L. Bhatti, T. J. Donohoe, R. G. Compton, J. Electroanal. Chem., 589 (2006) 187.
109. P. E. de Jongh, D. Vanmaekelbergh, J. J. Kelly, Chem. Mater., 11 (1999) 3512.

110. F.J. Del Campo, A. Neudeck, R.G. Compton, F. Marken, J. Electroanal. Chem., 477 (1999) 77.
111. F.J. Del Campo, A. Neudeck, R.G. Compton, F. Marken, S.D. Bull, S.G. Davis, J. Electroanal. Chem., 507 (2001) 144.
112. F.J. Del Campo, E. Maisonhaute, R.G. Compton, F. Marken, A. Aldaz, J. Electroanal. Chem., 506 (2001) 170.
113. C. A. Paddon, C. E. Banks, I. G. Davies, R. G. Compton, Ultrason. Sonochem., 13 (2006) 126.
114. T. Ohsaka, M. Isaka, K. Hirano, T. Ohishi, Ultrason. Sonochem., 15 (2008) 283.
115. C. Wang, L. Sun, H. Yun, J. Li, Y. Lai, C. Lin, Nanotechnology, 20 (2009) 5601.

Chapter 3

Experimental details

Copper thin films were synthesized from a simple aqueous sulfate solution at low bath temperatures in presence of ultrasound. Several different characterization techniques have been used to study the structure and properties of these films. In this chapter, the synthesis and characterization techniques are described in detail.

3.1. Synthesis

3.1.1. Chemicals and substrates

Copper sulfate (Cu_2SO_4. $5H_2O$) and sulfuric acid (H_2SO_4) of analytical grade were obtained from Merck and used as received without further purification. Aqueous solution was prepared from doubly distilled water. Graphite sheets were from Asbury Ltd. USA and aluminum (99% pure) from local market was procured. All other chemical were used as received.

3.1.2. Electrode preparation

Every time, fresh graphite electrodes washed with acetone and dried properly were used for experimentation where as aluminum electrodes follow simple preparation routine before experimentation. The electrodes were treated before each use; by first washing with distilled water and polishing with alumina powder 0.05 μm and then with diamond paste. Then, the electrodes were repeatedly washed with ultrasound and successively in distilled water and acetone for 20 min. The electrodes were finally dried in order to remove solvents.

3.1.3. Electrochemical cell and instrumentation

The electrochemical cell used was a conventional three-electrode configuration, with a 5 cm long counter electrode of Pt rod (3.5 cm^2) and an Ag/AgCI reference electrode (3M KCl, Eco chemie). A regular cell was employed for experiments without ultrasound. A small amount of the solution about 100 ml was taken out in a beaker for the silent experiments. A still water-jacketed cell of 500 ml capacity was used in the sonication measurements to maintain the temperature as shown in fig. 3.1. Before putting the solution into the water jacketed cell, a freezer was used to maintain low temperature conditions. Experiments were performed in the absence of antifreezers to avoid/minimize convoluting complications by the presence of foreign particles. The data acquisition and control was handled by a computer interfaced to the potentiostat/galvanostat (EG&G Autolab 12, Netherland) via General Purpose Electrochemical Software (GPES). The instruments were calibrated using dummy cells to calibrate the data. Sonication applications were accomplished either by a 20 kHz ultrasonic horn transducer system with 20% power output (Sonics & Materials, VCF 1500) fitted with a titanium probe of 25 mm diameter or an ultrasonic cleaner of 30 kHz frequency, with 60 W power with an inbuilt thermostatic heater of 0.04 kW. The working electrodes were semicrystalline graphite electrodes or aluminum electrodes.

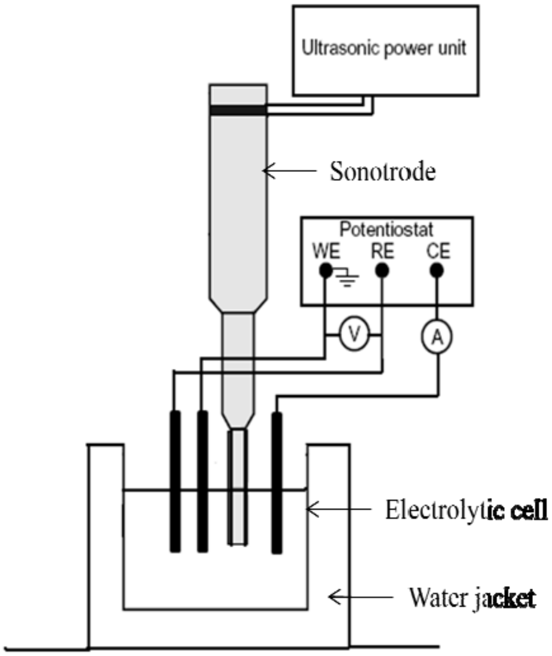

Fig. 3.1. The sonoelectrochemical cell

3.1.4. Deposition

The electrolyte used in these experiments differs from those encountered in usual electrochemistry. Usually, one works in the presence of a supporting electrolyte apart from the electroactive species which react at the electrodes (for example Cu^{2+}). The electrolyte contains non-electroactive species, preferably in much higher concentration (for example Na^+ and $SO_4{}^{2-}$). The interest of these non-electroactive ions is double: first, by increasing the conductivity of the electrolyte, they limit the ohmic potential drop in the electrolyte and thus the voltage applied to the cell. In addition to the economic interest for industrial applications, this enables to control the interfacial potential. In addition, if the electrolyte conductivity is mainly due to the non-electroactive ions, one can neglect the effect of the electric field on the movement of the ions, which are thus driven primarily by diffusion (and possibly convection). Thus, when electrodepositing copper in the presence of a large concentration of supporting ions, one can consider that the Cu^{2+} ions move randomly in the electrolyte. When a cation comes in contact with the cathode, if the potential is sufficiently negative, the reduction will take place and the cation will deposit. This simple behavior enables to easily predict the interfacial current. In the system of interest here, there is no supporting electrolyte, and the only ions are, Cu^{2+} and $SO_4{}^{2-}$. This situation, apparently simpler, is actually much more complicated than the preceding one. The electric field in the cell cannot be neglected when one wants to describe the ionic motion. The ionic concentrations thus evolve under the combined action of the diffusion forces, proportional to the concentration gradients, and of the migration forces, proportional to the electric field. These forces will not be the same for the anions and the cations. This is particularly obvious for migration, which is proportional to the electric charge and thus will be in opposite directions for the anions and the cations. The distinct evolution of anionic and cationic species can lead to different distributions for anions and cations and hence to a departure from electric neutrality within the electrolyte.

Copper was deposited from this binary electrolyte either by linear sweep voltammetry or single step potential scan. For the linear sweep voltammetry potential was varied from – 100 mV to – 600 mV. In single step potential scan, potential steps of – 300 mV or – 450 mV were employed for 20 to 40 seconds. The detailed conditions for deposition have been explained in the respective sections of results and discussions.

3.2. Characterization methods

The possible general methods which can be used for the analysis of the coating and the base metal's structure and properties are illustrated in fig. 3.2. The following section includes a brief description of the principles of the methods and the machines with the operating condition used in the present investigation.

3.2.1. X-ray diffraction (XRD)

XRD techniques are based on the elastic scattering of X-rays from structures that have long range order. XRD is a technique used to characterize the crystallographic structure, crystallite size (grain size), and preferred orientation in polycrystalline or powdered solid samples. Powder diffraction is commonly used to identify unknown substances, by comparing diffraction data against a database maintained by the International Centre for Diffraction Data. It may also be used to characterize heterogeneous solid mixtures to determine relative abundance of crystalline compounds and, when coupled with lattice refinement techniques, such as Rietveld refinement, can provide structural information on unknown materials. Powder diffraction is also a common method for determining strains in crystalline materials. An effect of the finite crystallite sizes is seen as a broadening of the peaks in an X-ray diffraction as is explained by the Scherrer equation. XRD patterns were recorded from 30˚ to 140˚ with a Philips X-pert MPD system diffractometer using Cu K_α at an accelerating voltage of 40 kV.

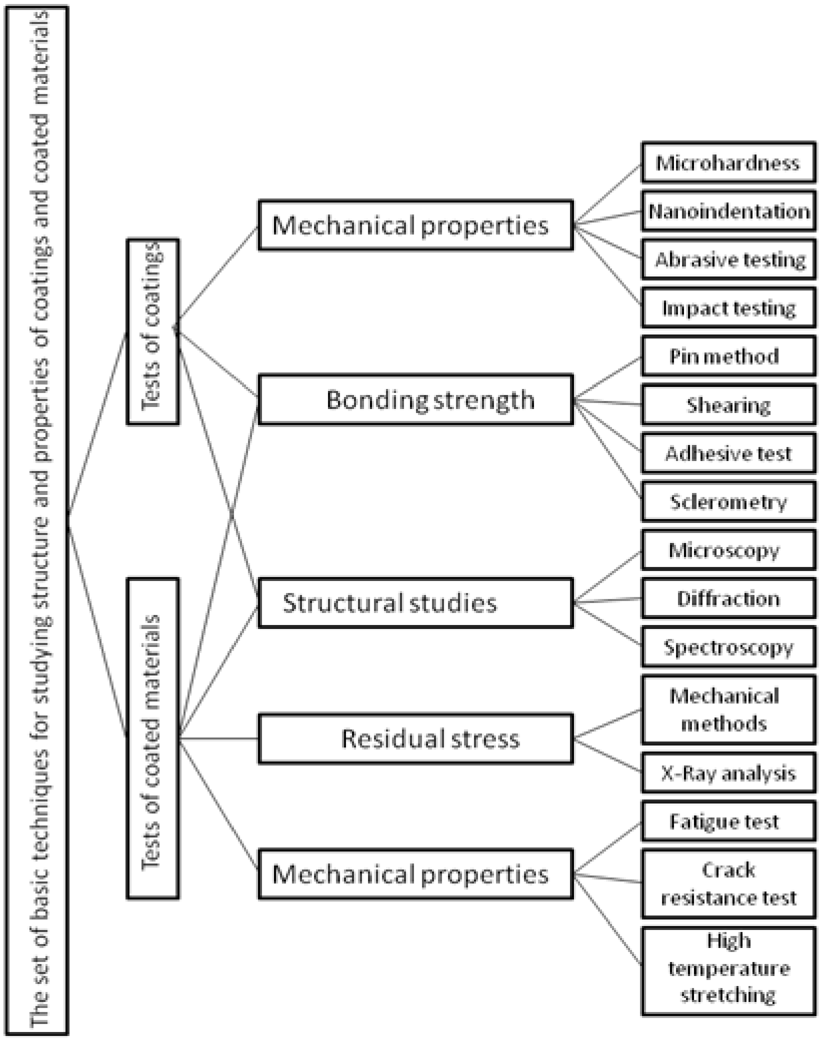

Fig. 3.2. Classification of techniques for studying coatings and coated materials

Data was collected at a counting rate of 1°/min. The K_α doublets were well resolved. Crystal size was estimated by the well established, Williamson-Hall [2] formula (As Scherrer equation is valid only for powders or loosely bound deposits but not for hard and adherent deposits).

The contribution of the particle size and nonuniform strain in the grains to the observed X-ray line broadening, β, are considered to be additive generating the formula as:

$$\beta_{total} = \beta_{particle} + \beta_{strain} = \frac{(0.94\lambda)}{(t\cos\theta)} + 4\tan\theta\frac{\Delta d}{d} \qquad (3.1)$$

The total broadening (β_{total}) is the measured FWHM in radians, corrected for instrumental broadening. The X-ray wavelength of the source Cu K_α is $\lambda = 0.15418$ nm, where t is the particle size, and 4 ($\Delta d/d$) represents the strain. Multiplying both sides of the equation by $\cos\theta$ gives the final form, $\beta_{total}\cos\theta = 0.94\lambda/t + 4\sin\theta(\Delta d/d)$, which is used to calculate the particle size and lattice strain of the copper deposit from the plot of $\beta_{total}\cos\theta$ versus $\sin\theta$.

3.2.2. Scanning electron microscopy (SEM)

SEM is a type of microscopy technique that images the sample surface by scanning it with a high-energy beam of electron in a raster scan pattern. The electrons interact with the atoms that make up the sample producing signals that contain information about the sample's surface topography, composition and other properties such as electrical conductivity. Microscopic studies to examine the morphology, particle size and microstructure were done by a JEOL 6480 LV SEM equipped with an energy dispersive X-ray detector of Oxford data reference system. Micrographs were taken at accelerating voltages of either 15 or 5 kV for the best possible resolution from the surface rather than the interior of the deposit. Energy dispersive spectroscopy (EDS) spectra were recorded at an accelerating voltage of 20 kV and the real collection time was around 1 min.

3.2.3. Atomic force microscopy (AFM)

Scanning Probe Microscopy (SPM) is a branch of microscopy that forms images of surfaces using a physical probe that scans the specimen. An image of the surface is obtained by mechanically moving the probe in a raster scan of the specimen, line by line, and recording the probe-surface interaction as a function of position. Many scanning probe microscopes can image several interactions simultaneously. The manner of using these interactions to obtain an image is generally called a mode i.e. AFM, MFM, LFM, EFM, STM, SECM and many more. AFM or scanning force microscopy (SFM) demonstrates resolution of fractions of a nanometer by feeling the surface with a mechanical probe. These images in contact mode with a conducting P(n) doped silicon tip were obtained with a SPMLab programmed Veeco diInnova MultiMode Scanning Probe Microscope. In some other graphs SIEKO SPA 400 atomic force microscope (AFM) with a silicon probe in non-contact mode was also used to take the AFM figures. The scans were taken at scan rates of 1 Hz. Images are taken to analyze the surface's physical properties in micron and sub-micron levels. However, 3D micrographs can be obtained from the analysis.

3.2.4. Surface Profilometer

This technique was used to get the real surface texture (in terms of roughness and waviness), thickness and residual stresses during the electrdeosition of the films. A diamond stylus is moved vertically in contact with a sample and then moved laterally across the sample for a specified distance and specified contact force. A profilometer can measure small surface variations in vertical stylus displacement as a function of position. A typical profilometer can measure small vertical features ranging in height from 10 nanometres to 1 millimetre. The height position of the diamond stylus generates an analog signal which is converted into a digital signal stored, analyzed and displayed. The radius of diamond stylus ranges from 20 nanometres to 25 μm, and the horizontal resolution is controlled by the scan speed and data signal sampling rate. The stylus tracking force can range from less than 1 to 50 milligrams. The analysis was carried out in a Dektak 150 surface profilometer at a force of 0.2 mg.

3.2.5. Nano-indentation

In nanoindentation small loads and tip sizes are used, so the indentation area may only be a few square micrometer or even. This presents problems in determining the hardness, as the contact area is not easily found. AFM or SEM techniques may be utilized to image the indentation, but can be quite cumbersome. Instead, an indenter with a geometry known to high precision (usually a Berkovich tip, which has three-sided pyramid geometry) is employed. During the course of the instrumented indentation process, a record of the depth of penetration is made, and then the area of the indent is determined using the known geometry of the indentation tip. While indenting, various parameters such as load and depth of penetration can be measured. A record of these values can be plotted on a graph to create a load-displacement curve. These curves can be used to extract mechanical properties of the material.

3.2.6. Differential Scanning Calorimetry

Differential scanning calorimetry or DSC is a thermoanalytical technique in which the difference in the amount of heat required to increase the temperature of a sample and reference is measured as a function of temperature. Both the sample and reference are maintained at nearly the same temperature throughout the experiment. Generally, the temperature program for a DSC analysis is designed such that the sample holder temperature increases linearly as a function of time. The reference sample should have a well-defined heat capacity over the range of temperatures to be scanned. Experiments were carried out by using a low temperature METTLER TOLEDO (DSC822) DSC, in the temperature range of 25 – 400 °C at a scan rate of 5 °/min.

3.3. References

1. G. K. Williamson, W. H. Hall, Acta Metall., 1 (1953) 22.

Chapter 4

Results and Discussions

4.1. A study on nature and character of copper films

Properties of materials are in general and deposits in particular are strongly dependent on the morphology and structure of the material. A large number of studies in statistical physics show that, out of equilibrium growth may lead to a variety of fractal morphologies. Electrodeposition of metals can produce deposits with very different morphologies by changing, sometimes slightly varying the experimental conditions. Hence, the work has started from morphological, structural and compositional investigations.

4.1.1. Introduction

The effect of low temperature may have a huge discrimination on the deposit characteristics, as discussed in chapter 2. The reduction in temperature has resulted in a change in morphology habitat as reported in [1] for Se and Cu depositions [2]. Grain refinement [3,4] as well as coarsening [5,6] of the deposits has been cited in the literature. Porous [7,8] and compact [1,9] deposits have also been observed with reduced electrolyte temperature.

This section is written based on the published article

A. Mallik, B. C. Ray, Morphological study of electrodeposited copper under the influence of ultrasound and low temperature, **Thin Solid Films**, 517 (2009) 6612.

By enlisting these diversities, there is surely a great research ahead for the seemingly simple but controversial parameter. Furthermore coupling ultrasound to the depositing bath may introduce second level of metastability with a wide variation of effects on the deposit morphology and properties [10-13], resulting primarily from acoustic cavitaion: the formation, growth, and implosive collapse of bubbles in liquids [14-17]. Electrodeposition in presence of ultrasound may have effects on the deposits in terms of appearance, adherence, grain morphology and habitats. To cite few are, reduction in grain size [18], change in grain orientation with wave orientation [19], particle agglomeration and increased dispersion [20,21], brighter surface [22] and reduction in residual stress and hence good adhesion [19,23] have been observed at constant frequency and power output. While with varying frequency and intensity, inconsistent fluctuations in the deposit behavior were also cited in the literature [19,24]. Hence the present experiment aims here to find the synergistic effects of low temperature and ultrasound on the deposit phase and morphology by different microscopic techniques and X-ray diffraction (XRD) method.

4.1.2. Experimental details

Copper was potentiostatically deposited from a simple aqueous solution of $CuSO_4$ (10 g l^{-1}) and H_2SO_4 (40 g l^{-1}) in an open cell. Double distilled water and analytical grade chemicals were used. Saturated calomel electrode was used as the reference electrode. Electrodeposition was done in a fixed cathodic potential range of 100 mV to 600 mV at a sweep rate of 1 mV/s onto rough graphite electrodes from. Temperature ranges selected for the experimentation are 25 ˚C, 19.5 ˚C, −1 ˚C and −3 ˚C. A freezer was used to maintain low temperature conditions. Experiments were performed in absence of antifreezers to avoid/minimize convoluting complications by the presence of foreign particles. An ultrasonic cleaner of 30 kHz frequency, with 60 watts power with an inbuilt thermostatic heater of 0.04 kW was used for sonication impact. Phase and structure was done by recording XRD patterns from 30˚ to 140˚ with a Philips X-pert MPD system diffractometer using Cu K_α at an accelerating voltage of 40 kV. Data was collected at a counting rate of 1˚/min. The K_α doublets were well resolved. The morphology, particle size and microstructure were done by a SEM (JEOL 6480 LV) equipped with an energy dispersive X-ray detector of Oxford data reference system. Micrographs were taken at an accelerating voltage of 5 kV for the best possible resolution from the surface rather than the interior of the deposit. Energy dispersive spectroscopy (EDS) spectra were recorded at an accelerating voltage of 20 kV and the real collection time was around 1 min. AFM (SIEKO SPA 400) study was done with a silicon probe in non-contact mode.

4.1.3. Results and Discussion

4.1.3.1. XRD analysis

To clearly illustrate the deposition temperature effects on the structure, XRD patterns of the deposits along with the annealed pure copper are represented in two parts i.e. at low (fig. 4.1.) and high 2θ (fig. 4.2.) values. All the peaks display both peak broadening and peak shift with reference to the pure copper. Decrease in either domain size or lattice strain will cause effective broadening of diffracted peaks [25]. Figs. 4.1(a&c) shows the low angle regions of the sonicated and silent deposits respectively. The peak pattern shows high crystallinity of copper along with peaks from the substrate material.

The diffraction peaks at 2θ = 43.27, 50.34 can be indexed as the (111), (200) planes of copper with cubic symmetry respectively [26]. With decreasing temperature, broadening increases where as intensity decreases. Similar XRD plateaus for decreasing crystallite size were observed by others [27,28]. Average crystallite sizes of copper deposit were determined by the Williamson-Hall formula. The obtained grain size variation is given in Table 4.1. Crystallite size got finer with decreasing temperature. The associated strain with the lattice system was increased with decreased grain size.

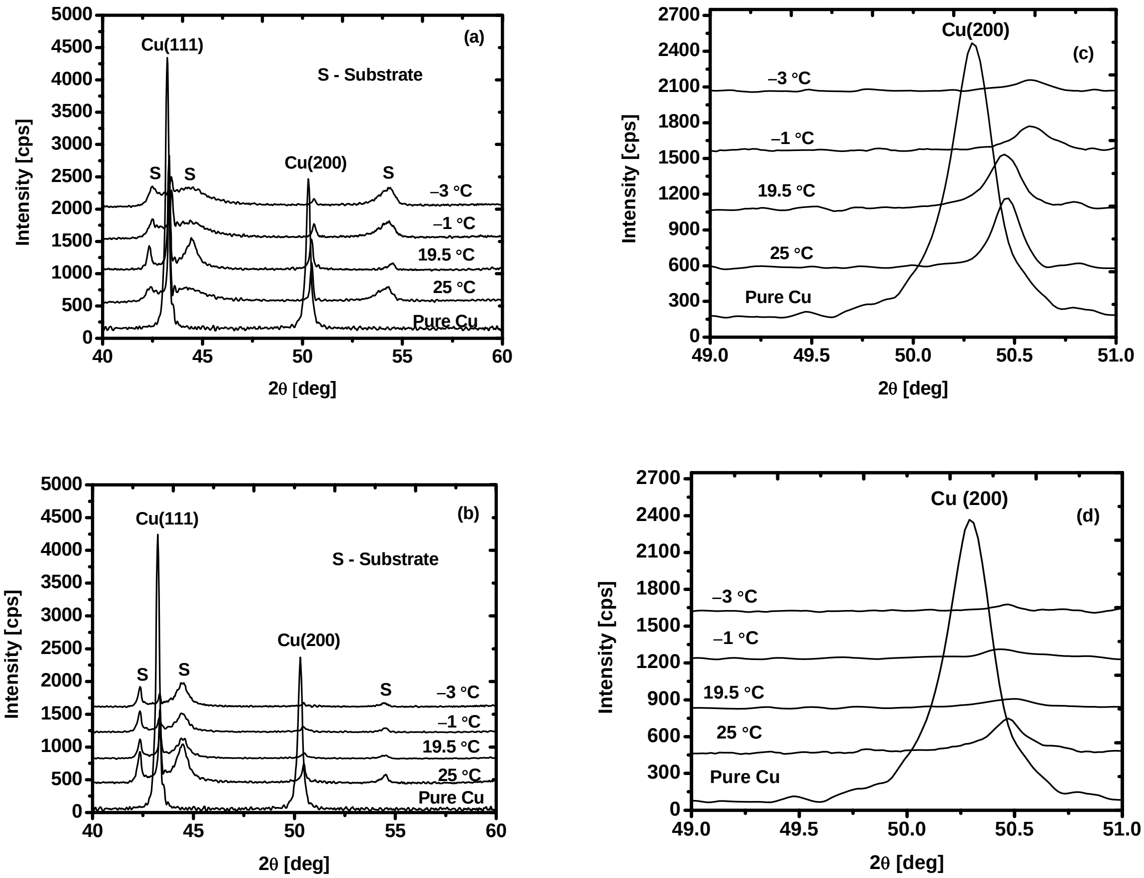

Fig. 4.1. XRD patterns of copper films (on graphite) prepared at different temperatures in (a,c) silent and (b,d) sonication conditions

The variation in grain size in silent condition is following a gradual reduction while under sonication there is an abrupt drop from 210 nm to 28 nm with reduction of temperature of 5 °C. The issues can be cleared in the next section of investigation on nucleation mechanism. The X-ray domains (defined as a volume that diffracts coherently) are usually much smaller than the microscopically observed grains [29]. The analysis on the peak shift of the patterns is done by magnifying the diffraction angle at Cu (200) as given in figs. 4.1b&d for silent and sonication conditions respectively. The magnitude of peak shift is high for silent depositions than the sonicated deposits. Peak shift in the diffraction pattern is consistent with current theories concerning the effects of stacking and twinning faults on x-ray diffraction powder patterns [30]. In addition, it is also mentioned in the open literature that the stacking fault location has a great effect on the magnitude of the peak shifts. Hence, whether the intensity or location of the crystal faults have resulted such variations in the magnitude of peak shift for the deposition conditions may not be solved at this juncture.

Table 4.1: XRD grain size and lattice strain of sonicated copper deposits

Temperature in ˚C	**Grain Size in nm**		**Lattice Strain**	
	Sonication	**Silent**	**Sonication**	**Silent**
25	210	300	0.005	**0.004**
19.5	28	150	0.021	**0.01**
–1	22	98	0.024	**0.015**
–3	**6**	**51**	**0.070**	**0.02**

Figs. 4.2a&b show the high angle peaks of the diffraction pattern for silent and sonicated deposits respectively. Diffraction peaks are compared with a pure annealed copper sample. Peaks from (311) and (222) planes are present in all deposits [26]. However, the peak corresponding to the plane (400) at 2θ of 116.923 is present only in case of pure annealed copper. The above result supports the fact that diffraction from planes at high angle is not prominent with reduced grain size [25,31].

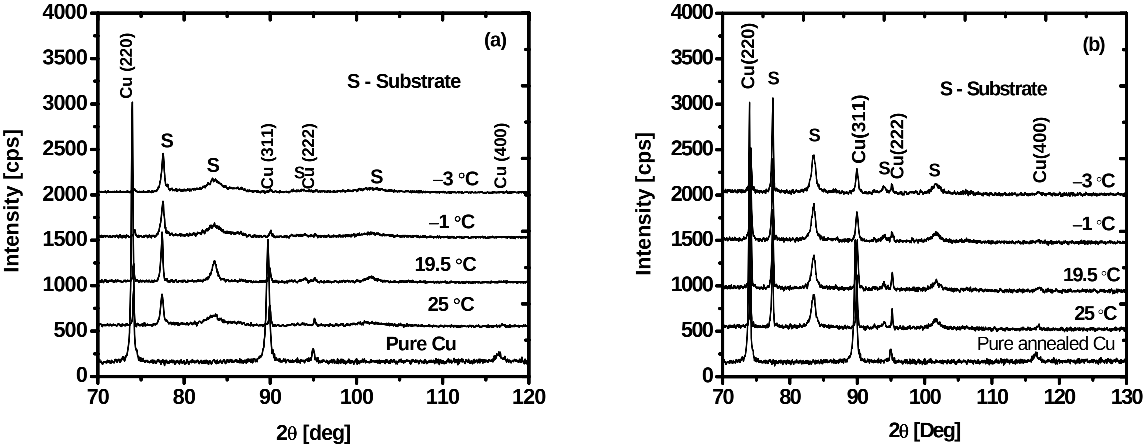

Fig. 4.2. XRD patterns of copper films (on graphite) prepared under (a) silent and (b) sonication at high 2θ values

4.1.3.2. Microscopic analysis

Fig. 4.3 shows the SEM morphologies of deposit at 25 ˚C, 19.5 ˚C, −1 ˚C and −3 ˚C temperatures.

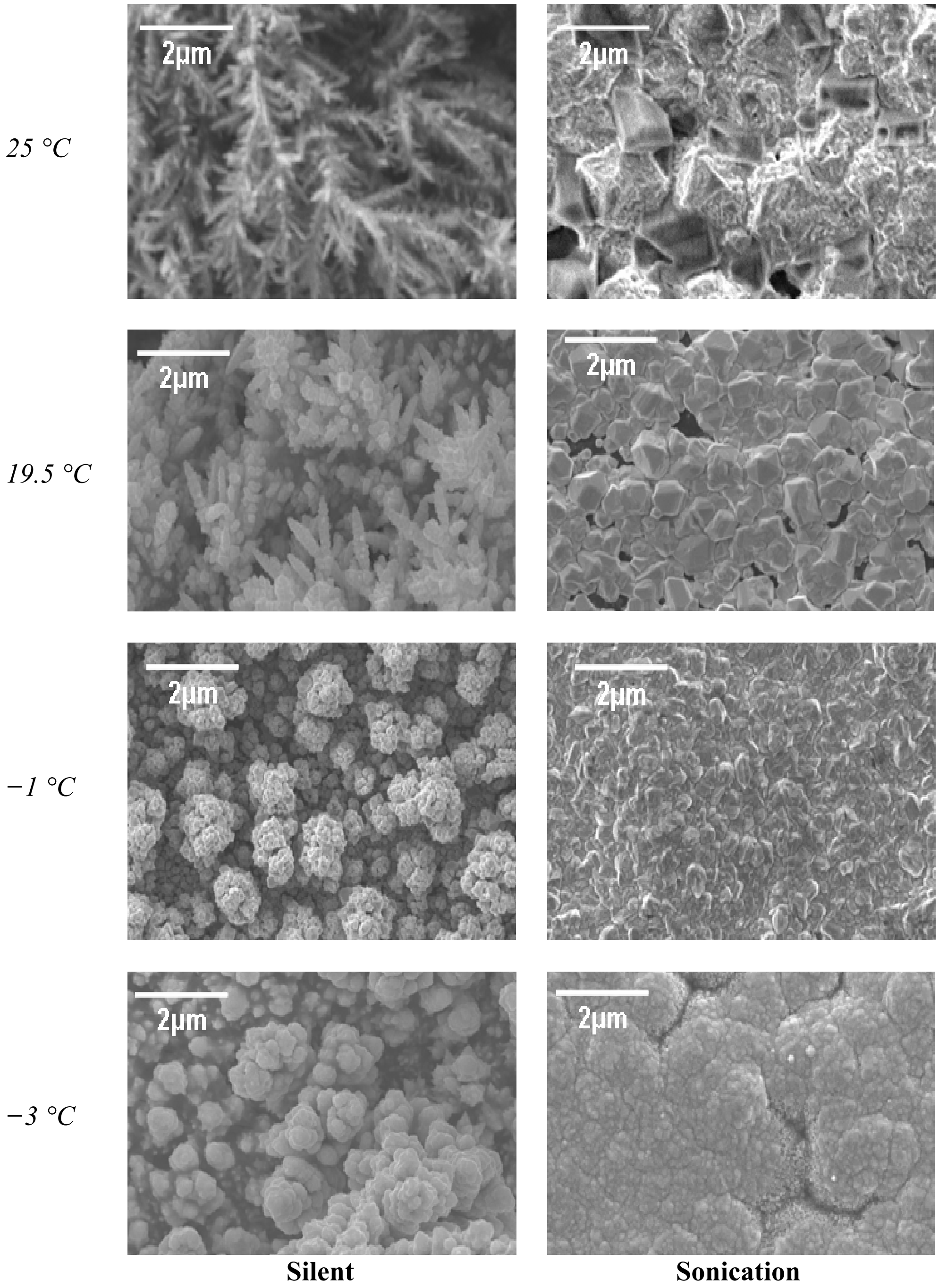

Fig. 4.3. SEM images of copper deposits (on graphite) with and without sonication at 25, 19.5, –1 and –3 ˚C

Sonicated deposit at ambient condition shows a clear impression of powdery morphology, while the grains are not so uniform. The grain boundaries are not so clear. Some regions are near granular, and some are highly distorted with few perforated grains. It is reasonable to assume that the distortion may be due to the ablating effect of the microstream jetting of ultrasound. The corresponding figure at silent condition is a highly branched sharp dendritic structure. At 19.5 ˚C temperature, sonicated substrate is covered by bimodal faceted copper structures as comparison to that of the truncated dendrites of the deposit without ultrasound. There are numerous big grains on the surface of copper deposits with a mean grain size of 2 µm. In addition many small grains are clearly found on these large grains. The above result may be attributed to the following factors. The surface concentration of Cu ions is high because of enhanced mass transportation by ultrasound. Hence the diffusion of Cu^{2+} improves the bulk deposition of Cu, resulting in well defined larger copper grains. The nucleation and grain growth have occurred simultaneously. Accordingly, the smaller copper grains are clearly observed on the larger grains and also on the substrate. Moreover, the result also suggests that the freshly deposited copper adatoms have moved to energy-favorable lattice sites during deposition, resulting in the distinct grain boundaries and faceted structures. Significant change in appearance can be observed at –1 ˚C temperature. The basic characteristic of morphology is a uniform copper covered surface with well agglomerated spheroids. The findings may reasonably be explained with the following lines. First, low temperature has resulted in high supersaturation favoring formation of smaller nuclei but in a random fashion of discharging. Second**,** ultrasound has helped in the rate of mass transportation thus creating enhanced nucleation. This effect has filled the gap between two adjacent nuclei leading to a compact mass. The above fact can be confirmed by comparing the deposit with its silent counterpart. The deposit at silent condition shows branched structures and is not dense. Third, ultrasound helps in degassing at the electrode surface [32], leading to an adherent and bright deposit [33]. The deposit at –3 ˚C shows uniform and fully coalesced fine grained copper coating on graphite with ultrasound. A comparison with the counterpart silent deposit, confirms the fact mentioned above. A comparative compositional analysis from the EDS result has given in Table 4.2.

Table 4.2: EDS compositional analysis of silent and sonicated copper deposits at various temperatures

Temperature	**Silent Composition (at%)**			**Sonication Composition (at%)**		
	Cu	**O**	**S**	**Cu**	**O**	**S**
25	76	21	3	100	-	-
19.5	72	26	2	100	-	-
–1	65	34	1	100	-	-
–3	62	37	1	100	-	-

The results show that with decreasing temperature the impurity levels, mainly of oxygen is increasing in silent deposit whereas sonication depositions have zero levels of contamination. Oxygen content has got increased roughly with decreased temperature. EDS plot of the above mentioned fact has been given in fig. 4.4. Compound analysis from the Oxford data shows that the oxides at high temperatures are mainly CuO and Cu_2O at low temperatures.

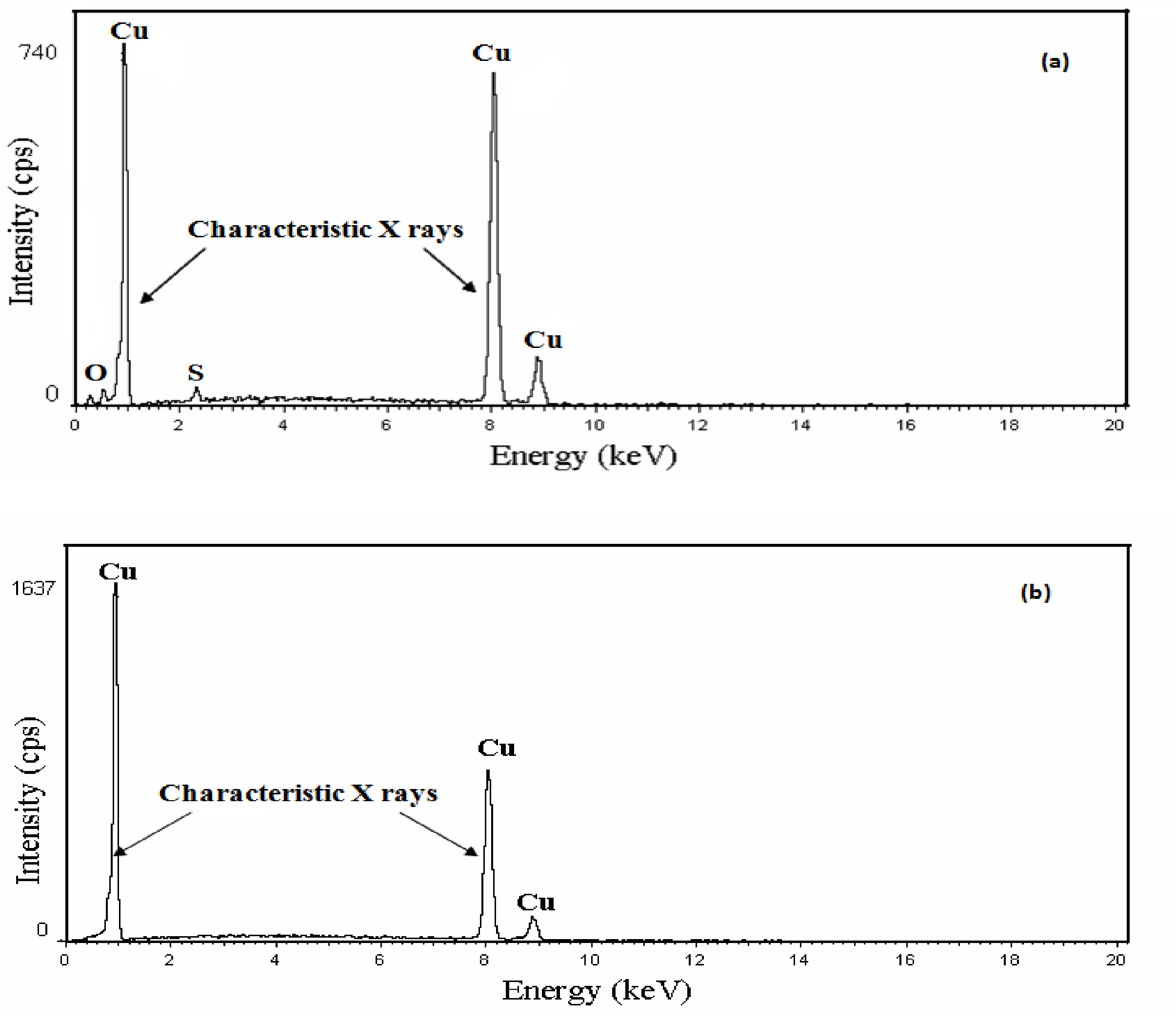

Fig. 4.4. EDS spectra of copper deposits (on graphite) prepared at 25 ˚C (a) without sonication and (b) with sonication

The fact that ionic character tends to increase [34] with reducing grain size and high symmetry structures are stable at low temperatures [35] might have resulted the above compositional variation in silent condition. conditions. Sulfur content of the deposit also shows a decreasing trend with temperature. The element usually gets adsorbed on the substrate from the electrolyte. Low temperature has reduced the adsorption tendency of the same. Due to the presence of a highly dynamic energy system, the conditions for the formation of the above weak covalent bond between copper and oxygen might have not been possible in ultrasonic field. Hence unlike the deposit in silent condition, the deposit obtained is free from adsorbed sulfur due to in-situ cavitational cleaning of the electrodes. The powdery morphology of the silent depositions did not allow engagement of the AFM tip on the substrate. Hence it was not possible to characterize the silent coatings by AFM. Height mode topographical AFM micrographs of the deposits at various temperatures are shown in figs. 4.5a-d. The surface roughness has decreased upto –1 ˚C and then has increased at –3 ˚C. Deposit morphology is not distinct in terms of grain boundaries, grain shape and size for depositions at 25 and 19.5 °C.

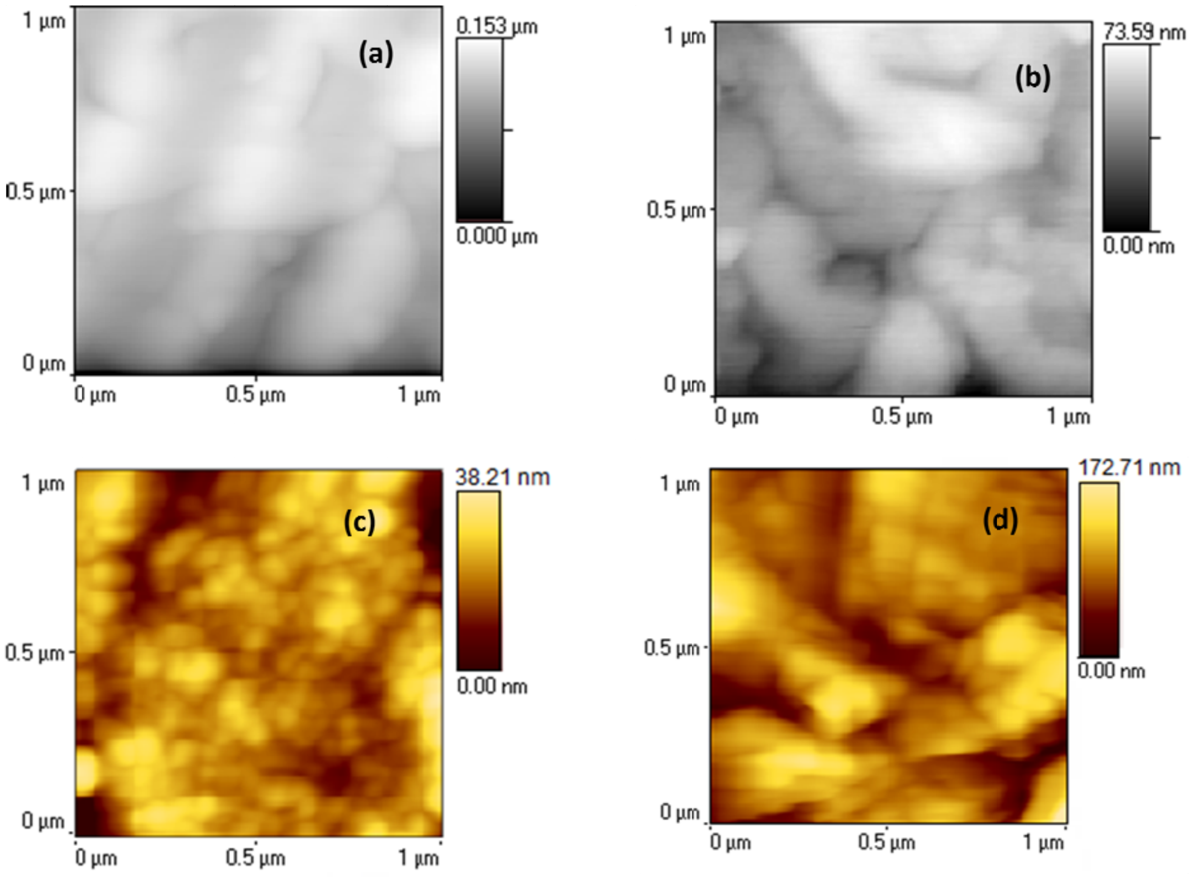

Fig. 4.5. AFM images of copper deposits (on graphite) prepared with sonication at (a) 25 ˚C, (b) 19.5 ˚C,(c) −1 ˚C and (b) −3˚C

While the deposits at –1 ˚C are copper spheroids of average height 38.21 nm and size of 30-40 nm. Furthermore the surface is nearly uniform as compared to high temperature sub-ambient depositions. Whereas the deposits at –3 ˚C show a maximum height of around 172 nm in contrast to the XRD domain size of 6 nm. The above discrepancy of the two methods is solved by a meticulous topographical analysis of the cluster and inter-cluster topographical height images. For the samples prepared at –3 °C, the clusters have grains in the size range of 20-30 nm. The high surface energy associated with the decreased size might have caused the deposits to agglomerate to a great extent. Hence, the next sections of studies for nucleation mechanisms involved and property evolutions have been restricted to temperatures of sub-ambient regions only.

4.1.4. Summary

An attempt has been made to explore the use of low temperature electrochemistry in synthesizing copper deposits in ultrasound cavitation condition. The crystallinity and morphology of the deposits have been characterized by XRD, SEM and AFM. In spite of the complicated and wide variation of morphologies and microstructures, the fact that the deposits belong to the nano range has been confirmed. A thorough compositional analysis of the deposits by EDS shows a cleaner sonicated deposit as compared to a highly oxidized silent deposit, which contains traces of adsorbed sulfur.

4.1.5. References

1. S. Zein El Abedin, A.Y. Saad, H.K. Farag, N. Borisenko, Q.X. Liu, F. Endres, Electrochim. Acta, 52 (2007) 2746.
2. Z. Zainal, A. Kassim, M. Z. Hussein, C. H. Ching, Mater. Lett., 58 (2004) 2199.
3. S. M. S. I. Dulal, H. Jin Yun, C. B. Shin, Chang-Koo Kim, Electrochimi. Acta, 53 (2007) 934.
4. L. Zhang, Z. Chen, Y. Tang, Z. Jia, Thin Solid Films, 492 (2005) 24.
5. O. Radovici, C. Vass, I. Solacolu, Electrodeposition and Surface Treatment, 2 (1973/74) 263.
6. H. E. Elsentriecy, K. Azumi, H. Konno, Electrochim. Acta, 53 (2008) 4267.
7. C. A. Marozzi, A. C. Chialvo, Electrochim. Acta, 45 (2000) 2111.
8. T. Aerts, J. B. Jorcin, I. D. Graeve, H. Terryn, Electrochim. Acta, 55 (2010) 3957.
9. E. Guaus, J. Torrent-Burgues, J. Electroanal. Chem., 549 (2003) 25.
10. S. J. Doktycz, K. S. Suslick, Science, 2 (1990) 1067.
11. L. J. McCausland, P. W. Cains, P. D. Martin, Chem. Eng. Prog., 97 (2001) 56.
12. R. Walker, Chem. Britain, (1990) 251.
13. P. Lorimer, T.J. Mason, Electrochemistry (formerly Denki Kagaku), 67 (1999) 924.
14. K. S. Suslick, Ed., Ultrasound: Its Chemical, Physical, and Biological Effects, Wiley VCH Publishers, New York, 1988.
15. K. S. Suslick, Sci. Am., 260 (1989) 80.
16. K. S. Suslick, R. E. Cline, Jr., D. A. Hammerton, J. Am. Chem. Soc., 108 (1986) 5641.
17. K. S. Suslick, E. B. Flint, Nature, 330 (1987) 553.
18. S. Floate, M. Hyde, R. G. Compton, J. Electroanal. Chem., 523 (2002) 49.
19. F. Touyeras, J.Y. Hihn, X. Bourgoin, B. Jacques, L. Hallez, V. Branger, Ultrason. Sonochem., 12 (2005) 13.
20. S. Ghasemi, M.F. Mousavi, M. Shamsipur, H. Karami, Ultrason. Sonochem., 15 (2008) 448.
21. V. Mancier, Anne-Lise Daltin, D. Leclercq, Ultrason. Sonochem., 15 (2008) 157.

22. C. T. Walker, R. Walker, Electrodeposition and Surfacte Treatment, 1 (1972/1973) 457.
23. T. Ohsaka, M. Isaka, K. Hirano, T. Ohishi, Ultrason. Sonochem., 15 (2008) 283.
24. F. Touyeras, J. Y. Hihn, M. L. Doche, X. Roizard, Ultrason. Sonochem., 8 (2001) 285.
25. B. D. Cullity, Elements of X-Ray Diffraction, Addison-Wesley Publisher, MA, 1978.
26. International Centre for Diffraction Data (ICDD), Card No. 04-0863.
27. R. P. Raffaelle, T. Potdevin, A. F. Hepp, S. G. Bailey, Mater. Sci. Semicond. Process., 2 (1999) 289.
28. M. H. Seo, D. J. Kim, J. S. Kim, Thin Solid Films, 489 (2005) 122.
29. H. M. Xu, H. G. Yan, Z. H. Chen, Mater. Charact., 59 (2008) 301.
30. J. D. Makinson, J. S. Lee, S. H. Magner, R.J. De Angelis, W.N. Weins, A.S. Hieronymus, JCPDS-International Centre for Diffraction Data, 42 (2000) 407.
31. C. Suryanarayan, M. Grant Norton, X-ray Diffraction a Practical Approach, Plenum Press, NY, 1998.
32. H. Yanagida, Ultrason. Sonochem., 15 (2008) 492.
33. E. Namgoong, J. S. Chun, Thin Solid Films, 120 (1984) 153.
34. H. Yanagimoto, K. Akamatsu, K. Gotohb, S. Deki, J. Mater. Chem., 11 (2001) 2387.
35. V. R. Palkar, P. Ayyub, S. Chattopadhyay, M. Multani, Phys. Rev. B, 53 (1996) 2167.

4.2. An understanding of nucleation mechanism of electrodeposited copper thin films

Nucleation and growth of materials are kinetically determined domains. As such, they typically lead to nonequilibrium morphologies, which relax in some fashion afterward. This set of topics nucleation and growth provides a framework for understanding many aspects of the world around us, from geological erosion to pharmaceutical sedimentation to nano-fabrication. As such, the topic is immensely important and scientifically ancient. This section deals with one small, but important, arena in which fresh insights about nucleation and growth are emerging, namely, sono-electrodeposition and a low temperature electrochemistry.

4.2.1. The impact of ultrasound during electrodeposition: The phenomena of secondary nucleation

Support for ultrasound creating extremely high level of localized supersaturation and capability of inducing crystal breakage may intensify the crystallization process. With regard to the crystallization process the study was specifically interested in the extent of impact of ultrasound on the nucleation and crystal breakage/size distribution. The new understanding of the sono-electrochemical mechanisms may clarify unclear issues and could possibly allow for the better design of sonoelectrochemical synthesis.

4.2.1.1. Introduction

Ultrasound capable of creating zones of extremely high level of localized supersaturation [1-5] should set on the nucleation process as observed in section 4.1. Now the question arises, is the level of supersaturation only which has resulted such remarkable change in morphology? To find the answer of the above unclear aspect, experimentation is done to elucidate the nucleation under ultrasound. In the process of growth, however, high indexed surface zones are transformed into atomically smooth equilibrium faces. Further phase formation needs the formation of new steps or irregularities on the substrate's surface for nucleation [6,7]. Crystal fragmentation by ultrasound may create new steps on the defect free crystal face to further supplement the crystallization process. Thus, ultrasonic energy is believed to stimulate a biphasic nucleation sequence i.e. primary (on the native substrate) and secondary (on the existing primary clusters) [8,9]. Though a limited literature have been reported on the aspects of ultrasound-induced secondary nucleation, there is an urgent pressing need of information particularly related to electrochemical phenomena. Hence, the purpose of this exploration is to investigate the impact of ultrasound on the nucleation phenomena. The study is specifically emphasized on the impact of ultrasound on the nucleation mechanism by crystal breakage.

This section is written on the published and unpublished works from the articles

A. Mallik, A. Bankoti, B. C. Ray, A study on the modification of conventional electrochemical crystallization under sonication: the phenomena of secondary nucleation, **Electrochemical and Solid-State Letters**, 12 (2009) F46.
A. Mallik, B. C. Ray, Implication of low temperature and sonication on Cu electrocrystallization mechanism: A kinetics and structural correlation, **Journal of Electrochemical Society** (JES-10-1620, revision submitted).

Researchers have employed fast linear sweep voltammetry (LSV) and cyclic voltammetry (CV) [10,11] to observe the quantitative mass transport transient The methods introduce potential driven supersaturation and hence there may not be an effortless clear prediction of the effects. However, little attention has been paid to sonoelectrochemically modified time dependent current analysis. An attempt has been made here to experiment the above effects through sono-chronoamperometric current transient (SCCT).

4.2.1.2. Experimental details

The bath composition was 6.35 g l^{-1} $CuSO_4$. $5H_2O$ + 60 g l^{-1} H_2SO_4. A 5 cm long platinum rod of 0.2 cm diameter and an Ag/AgCl electrode (Eco Chemie, Netherlands) served as counter and reference electrodes respectively. Ultrasound irradiation was accomplished by a 20 kHz ultrasonic horn with 20% output power transducer system (Sonics & Materials, VCF1500) fitted with a titanium tip. The tip was placed at a distant of 5 mm from the brass substrate. Electrochemical measurements were conducted using a potentiostat/galvanostat (Eco Chemie Netherland, Autolab PGSTAT 12) having computer interface of GPES software. A potential of – 0.45 V (100 mV more than the estimated Nernst equilibrium potential: – 0.35 V) was selected for the deposition. Experiments were performed on O_2 free brass substrates of exposed surface area of 0.25 cm^2. Experimentation was carried out for a set of time periods, 5 s, 10 s, 15 s and 20 s. the current transients were fitted to SH model [12] for the determination of standard kinetics parameters, D (Diffusion Coefficient) and N_0 (Active nucleation density). Surface morphology comparison was obtained using AFM (SPMLab programmed Veeco diInnova) in contact mode with a conducting P(n) doped silicon tip.

4.2.1.3. Results and Discussion

The sonicated chronoamperometric current transients (CCTs), after a two-point Golay–Savitzky normalization, and superimposed on the original transients, are shown in fig. 4.6a. The results disagree with the reports for cobalt deposition on a glassy carbon electrode [13] (fig. 4.6b. All the SCCTs have a sharp initial decrease in current followed by irregular troughs and crests such as current responses. The early fall is due to the double-layer charging at the electrode surface. The rest current progression may not be inferred as noise (2 s persistence). If it was the sole impact of sonication toward truncation in diffusion spheres, then the rising current should have a decreasing tail after a higher and also sharper current peak at the maximum compared to the virgin CCT. Thus, we did interpret these irregularities as a sequence of nucleation loops. The SCCTs have the initial loop at around 1.5 s, and the successive loops abounded with the same time occurrence. The preliminary loops may be due to the conventional three-dimensional (3D) nucleation and growth. The progressive loops should support the hypothesis of secondary nucleation by crystal breakage [8]. The experiment has also been extended without crystal breakage (silent condition). Fig. 4.7 shows the set of recorded virgin current transients with a typical single-current maximum. The silent CCT differs from the SCCT following a typical transient of the rising portion and then a decaying current obeying the Cottrell law.

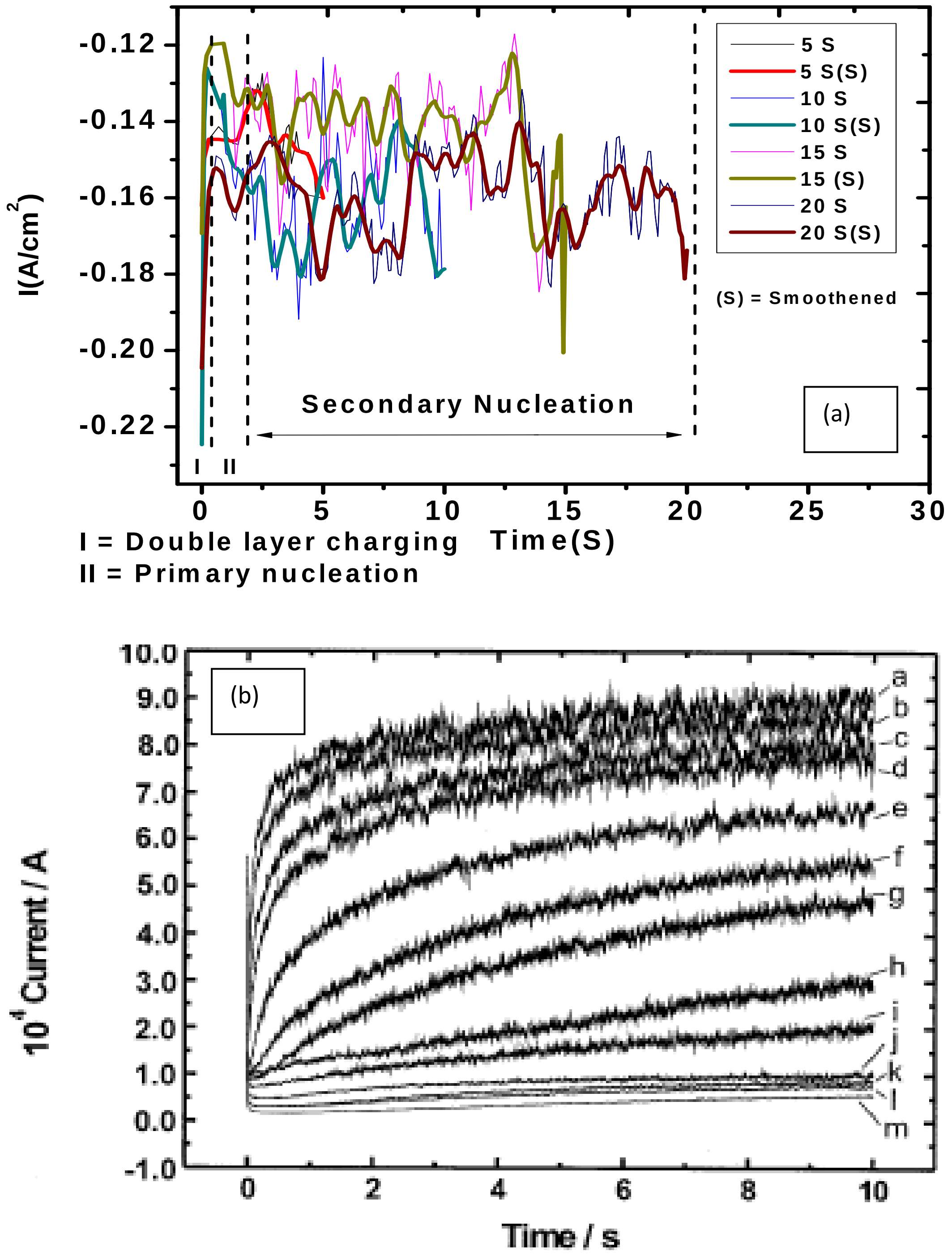

Fig. 4.6. Chronoamperometric current transients: (a) for Cu deposits for different time periods (on brass) with sonication and (b) for cobalt deposition, ref [13]

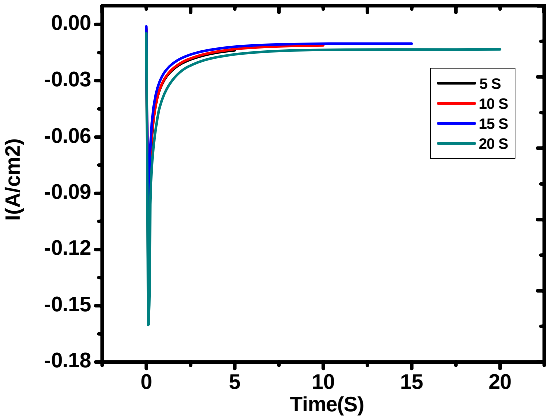

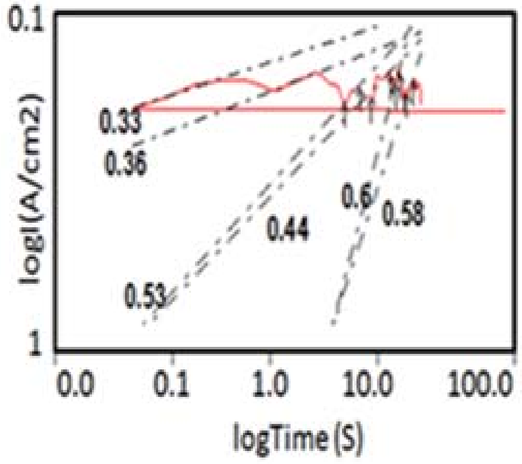

Fig. 4.7. Silent chronoamperometric current transients for Cu deposits (on brass) at different time periods

Fig. 4.8. log(current density) vs log(time) plot for sonicated Cu electrodeposition (on brass) at – 0.45 V for 20 s

The slope of log(current density) vs log(time) varied from 0.3 to 0.6, which indicates instantaneous phase appearance (as shown in fig. 4.8). Hence the kinetics parameters were calculated using Scharfiker's [12] general equation for instantaneous nucleation. Table 4.3 shows characteristic kinetics parameters along with total charge involved in the deposition process under insonation.

Table 4.3: Characteristic Kinetics Parameters of *i(t)* transients obtained for sonicated Cu deposits for different deposition time periods (The calculation is based on an equation in ref [12])

Time (Sec)	I_{max} (A/cm^2)	t_{max} (S)	D × 10^{-4} (cm^2 s^{-1})	$N_{0\ (P)}$ × 10^3 (cm^{-2})	$N_{0\ (S)}$ × 10^3 (cm^{-2})	$N_{0\ (T)}$ × 10^3 (cm^{-2})	Q_{total} (C)
5	0.146	1.5	5.2	3.82	1.85	5.67	0.18
10	0.150	1.7	6.3	2.78	4.42	7.2	0.397
15	0.149	1.5	5.3	3.25	5.75	9	0.531
20	0.164	1.4	6.2	3.4	6.06	9.46	0.791

The total charge consumed under sonication varies from 0.18 to 0.79 C as compared to the charges, 0.03–0.1 C, involved in the deposition without sonication. The difference may be attributed to the nucleation phenomena, as explained later. The table also contains the nuclei number density calculated for the secondary nucleation, $N_{0(S)}$), following the same model. The diffusion coefficient calculated in the silent condition was 4.2–3.2 × 10^{-5} cm^2 s^{-1} compared with the values of 0.8–1.5 × 10^{-5} cm^2 s^{-1} published elsewhere [14,15] while in the presence of ultrasound the diffusion coefficient increased in values, 5.2–6.3 × 10^{-4} cm^2 s^{-1}.

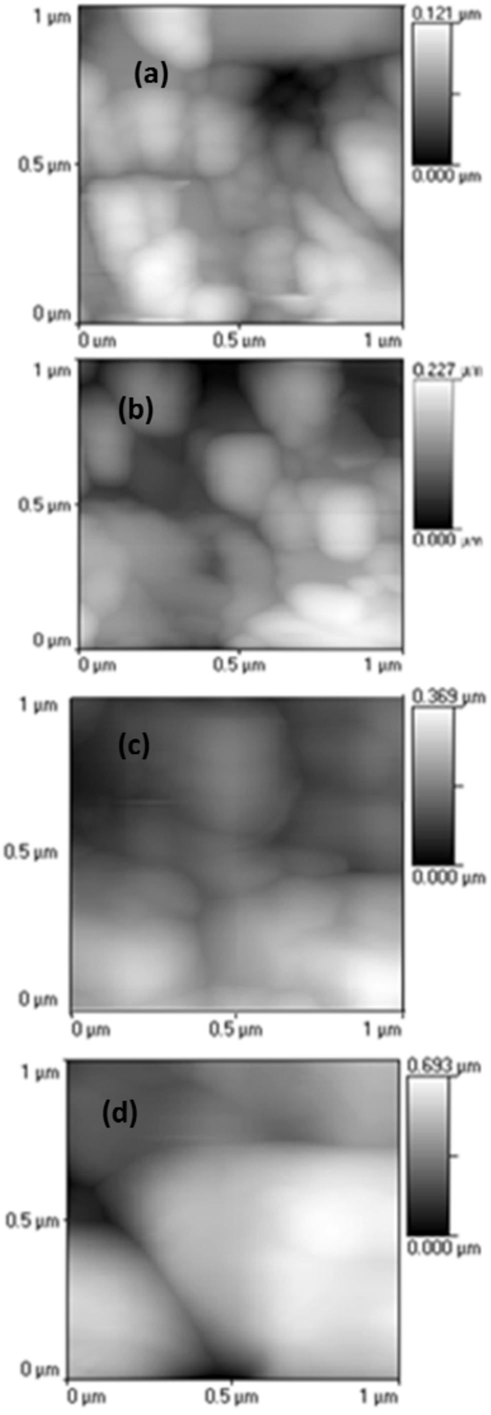

Fig. 4.9. AFM micrographs of silent Cu deposits (on brass) for (a) 5 s, (b) 10 s, (c) 15 s and (d) 20 s

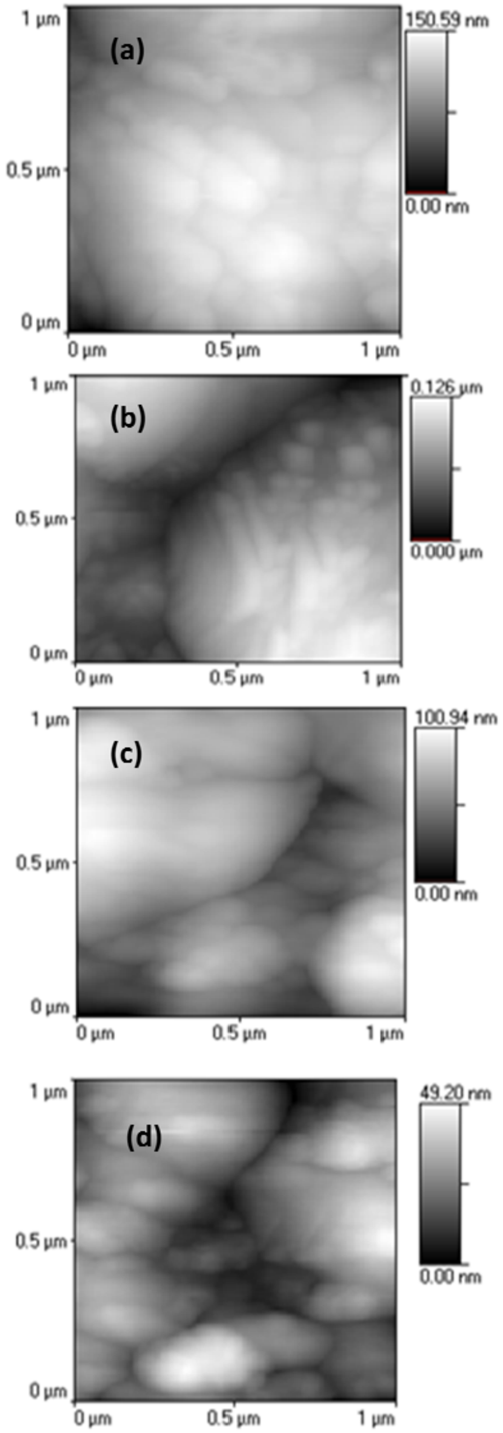

Fig. 4.10. AFM micrographs of sonicated Cu deposits (on brass) for (a) 5 s, (b) 10 s, (c) 15 s and (d) 20 s

The calculated nuclei number density for primary nucleation, $N_{0(P)}$, for all the time periods is approximately the same. The number density for the secondary nucleation increases with increasing time period, i.e., 1.8–6.06 × 10^3 cm^{-2}. However, the rate of increase in the number of secondary nuclei decreases with time. This may be explained by the fact that due to degassing at the electrodes, deposits are highly adherent under insonation [4]. Thus, the process of crystal breakage may not be possible for further protracted sonication.

Table 4.4: Roughness factor and grain size distributions of sonicated deposits from AFM measurements

Time	**Roughness factor (nm)**		**Average height (nm)**		**Thickness (nm)**	
	Silent	Sonication	Silent	Sonication	Calculated*	Measured
5	17	25	72	108	250	241
10	39	20	107	65	550	546
15	65	16	165	58	740	742
20	172	8	340	24	1100	1009

*Refer appendix

AFM micrographs for both conditions are shown in figs. 4.9 and 4.10 for 5, 10, 15, and 20 s. The total analysis of the area and volumetric analysis is given in Table 4.4. Deposition without the application of ultrasound has produced coarse grains, following the conventional trend of growth of the nuclei, at longer time periods. The average height and roughness of the deposits also increase simultaneously, whereas the grains of the sonicated films become finer for extended time periods. As the time of deposition increases, the standard deviation of the grain distribution becomes narrow and smooth. The deposit at 20 s is the finest. Most of the grains fall in the height range of 10–30 nm with an average height of 24 nm. The deposit is also the smoothest, having a roughness factor of 8 nm compared to the 172 nm value of its silent counterpart. This result can be interpreted as in the following ways: Ultrasound capable of crystal breakage produces smaller grains and balances the heights of grains. This, as a result, smoothens the surfaces at a longer period of deposition.

The peak and valley method of AFM analysis as well as surface profiler analysis have been used to measure the thickness of the films (Fig. 4.11). The micrograph, along with the line analysis, shows a nearly smooth and uniform deposit under sonication for AFM analysis. While the surface analysis by the stylus profiler shows quite surface irregularities. The average roughness was found to be around 128 nm, quite high than the value measured by AFM. The discrepancy may be due to the fact that, AFM analysis deals with specific area analysis and surface profiler scans the whole surface. The calculated film thickness from the two methods was having only 5% variations. The edge effects can clearly be observed from the analysis. The silent films are mostly irregular and are far from thickness measurements through these techniques.

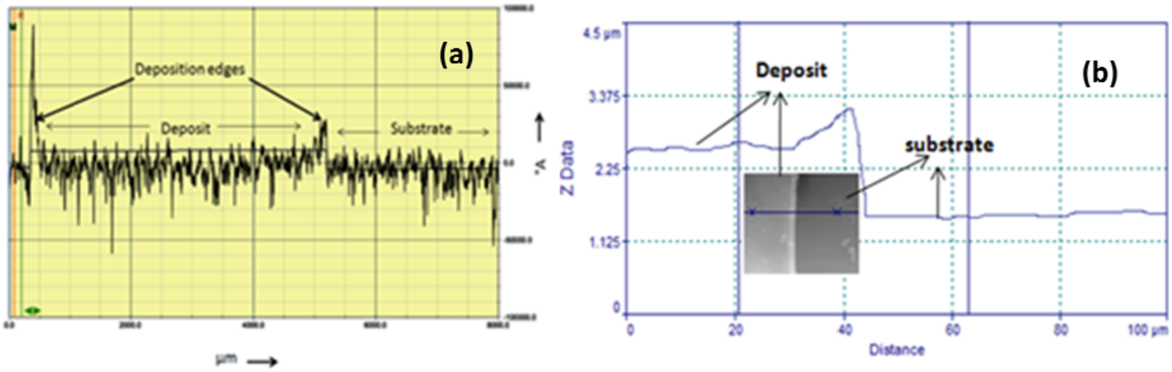

Fig. 4.11. Thickness measurement of sonoelectrochemically deposited
Cu film (on brass) by (a) surface profiler and (b) AFM

Thus, the measured and calculated (Appendix) values of the nearly uniform and smooth sonicated deposits are included in Table 4.4. Film thickness varied in between 240 to 1100 nm as the deposition time increased from 5 to 20 seconds.

4.2.1.4. Summary

The sonication possibly imparts the ambience for promoting secondary nucleation by breaking the primary nuclei. The CCT diagram is a clear indicator of the presence of secondary nucleation phenomena. Comparison with the Scharifker and Hills limiting cases indicate that at a longer period of deposition, a crystal breakage leads to higher population density. However the proposed phenomenon may not proceed for infinite period of time due to increased adherence under sonication. Contact mode AFM has been used to confirm the conclusions drawn from the CCTs. The observed microstructural morphology is in close proximity with an anticipated reduced grain size. In contrast, the deposits without sonication consist of coarse grains. Although Scharifker equations seem to demonstrate an instantaneous nucleation under sonication they are not entirely suitable to explain this behaviour and a new mathematical model should be considered. The significance of the present investigation could possibly be a new understanding on sonoelectrochemical synthesis, and following that its use in various critical and potential applications may be opened up.

4.2.1.5. References

1. S. Devarakonda, J. M. B. Evans, S. Myerson, Cryst. Growth Des., 3 (2003) 741.
2. C. A. G. Leyva, A. Q. Ramos, J. Barnard, R. R. B. Quintana, R. T. Abbud, J. J. Castro, J. Food Eng., 81 (2007) 374.
3. F. J. D. Campo, A. Neudeck, R. G. Compton, F. Marken, J. Electroanal. Chem., 477 (1999) 71.
4. E. Namgoong, J. S. Chun, Thin Solid Films, 120 (1984) 153.
5. T. J. Mason, J. P. Lorimer, S. Saleem, I. Paniwnyk, Environ. Sci. Technol., 35 (2001) 3375.

6. J. W. Christian, Transformations in Metals and Alloys, Pergamon Press Ltd., Hungary, 1975.
7. I. V. Markov, Crystal Growth for Beginners, World Scientific, Singapore, 2004.
8. R. Chow, R. Blindt, R. Chivers, M. Povey, Ultrasonics, 43 (2005) 227.
9. A. Mallik, B. C. Ray, Thin Solid films, 512 (2009) 6612.
10. G. S. Garbellini, G. R. Salzar-Banda, L. A. Avaca, Food Chem. (2009), doi: 0.1016/j. foodchem.2009.03.068.
11. C. A. Gutierrez, J. L. Hardcastle, J. C. Ball, R. G. Compton, Analyst, 124 (1999) 1053.
12. B. Scharifker, G. Hills, Electrochim. Acta, 28, 879 (1983).
13. S. Floate, M. Hyde, R. G. Compton, J. Electroanal. Chem., 523 (2002) 49.
14. D. Gruijicic, B. Pesic, Electrochim. Acta, 47 (2002) 2901.
15. O. Ghodabne, L. Roue, D. Belanger, Electrochim. Acta, 52 (2007) 5843.

4.2.2. Roles of temperature and sonication on electrocrystallization process

Fundamental aspects of electrocrystallization of metals are directly related to the mechanisms of nucleation and crystal growth. According to the thermodynamical concepts, a nucleation step is required not only for the formation of a new crystal, but also for the growth of a perfect singular crystal face by formation of new layers. Despite many years of intensive research, the theoretical description of the kinetics of nucleation and the subsequent growth is still a challenging area of research.

4.2.2.1. Introduction

At low temperature**,** the population of critical clusters increases whereas the rate of attachment of further atoms to the cluster decreases due to increased diffusion barrier [1]. Hence a net increase in nucleation rate is expected at low temperatures. Cavitation capable of creating an extremely high level of localized supersaturation and inducing crystal breakage may result in triggered nucleation [2,3]. Yet again remarkable increase in mass transport, the most distinct effect of cavitation, enables it to modify a diffusion controlled system to a charge transfer system [4-6]. Contribution of cavitation, thus, should affect nucleation more rather than growth. However increase in mass transport may also possibly affect grain growth. Hence the dominance of opposing effects of sonication and thermal environment are more likely to be contradictory, and that is far from conclusion.

Low temperature is a relative term and varies from system to system. For a Cu/Cu alloy depositing bath the vast majority of low temperature electrodeposition has been limited to 20-25 °C. Yet, Cu electrolyte temperature down to 10 °C has been maintained but for Cu_2O depositions [7]. Furthermore those investigations have been restricted to morphological and structural analysis. However, some aspects of redox kinetics have also been covered [8,9], but there is a serious lack of electrochemical characterization of nucleation and growth at such low temperatures. The first section under this chapter certainly enlists the interesting beneficial effects of temperature and sonication on the morphology and structure of deposits. However, the findings will be incompetent without proper information on the mechanism and kinetics of the phase formation. Hence the present section will investigate the effects of temperature and cavitation on the electrochemical crystallization mechanism. Electrochemical nucleation and growth phenomena have been analyzed and quantified by electroanalytical measurements including voltammetry and chronoamperometry and then correlated with morphological analysis.

4.2.2.2. Experimental details

Graphite substrates (Asbury, USA) of 0.25 cm^2 surface area were used to electrodeposit the copper films. The bath composition was 6.35 g l^{-1} $CuSO_4$. $5H_2O$ + 40 g l^{-1} H_2SO_4. Chemicals (as received) were used without further purification. A three electrode open cell with an Ag/AgCl reference electrode (Eco Chemie, Netherlands) and a platinum counter electrode (surface area of 3.14 cm^2) were used for the deposition. The depositions were carried out at temperatures of 25 °C, 20 °C, 15 °C, 10 °C and 5 °C. A high-density ultrasonic probe (Sonics & Materials, VCF1500) equipped with titanium oscillator (horn) 12.5 mm in diameter, operating at 20 kHz with a 20% output was used for ultrasonic irradiation.

Electrochemical measurements were conducted using a potentiostat/galvanostat (Eco Chemie Netherlands, Autolab PGSTAT 12) interfaced with a PC controlled with GPES software. A potential of 300 mV was selected for the deposition. The surface morphology comparisons were obtained using SEM (JEOL 6480 LV with Oxford data system) and atomic force microscope (SPMLab-programmed Veeco diInnova) in the contact mode with a conducting p(n)-doped silicon tip.

4.2.2.3. Results and discussions

4.2.2.3.1. Ultrasonic Power calculation

Recently Margulis and Margulis [10] have improved the most widely accepted calorimetric technique for determining the power from an acoustic horn in an aqueous solution. This method involves taking a known volume of water (or the working solvent) and applying ultrasound for a time period (t_{us}) upto a suitable rise of temperature while monitoring the change in temperature with time. Then the ultrasonic source is switched off with the solution being monitored as it cools down. Fig. 4.12(a) shows the sets of temperature vs. time graphs for various ranges of temperatures.

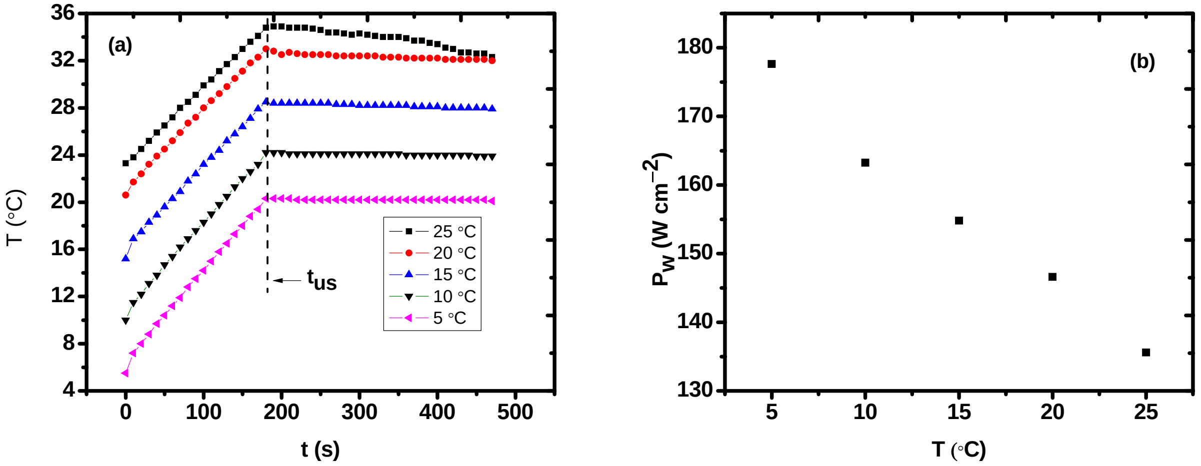

Fig. 4.12. (a) Change in solvent temperature under sonication as a function of time and (b)the calculated ultrasonic power at various temperatures

The power in the system is calculated using the following equations:

$$P_W = C_{sys} m \frac{\Delta T}{t} \qquad (4.1)$$

where Pw is the ultrasonic power, m is the mass of the solvent used, t is time, C_{sys} is the specific heat capacity of the system, which is described by $C_{sys} = C_W M_W + C_g M_g$, where C_g and M_g are specific heat capacity and mass of the container used (in this case glass) respectively. ΔT is the difference in temperature between the liquid and environment. The change in temperature above ambient (ΔT) is described by the following equations:

$$\Delta T(t) = \frac{P_W t}{C_{sys} m}\left(\frac{1-e^{-\alpha t}}{\alpha t}\right) \quad (t \leq t_{us}) \qquad (4.2)$$

$$\Delta T(t) = \frac{P_W t_{us}}{C_{sys} m}\left(\frac{1-e^{-\alpha t_{us}}}{\alpha t_{us}}\right) \; e^{-\alpha(t-t_{us})} \; (t > t_{us}) \qquad (4.3)$$

where α is a parameter which characterizes heat exchange between the liquid under insonation and its exterior. Following equation (4.3) a plot of $ln\ \Delta T\ versus\ (t - t_{us})$ will yield $-\alpha$, which is a parameter which characterises heat exchange between the liquid under insonation and its exterior (from the downward portion of the graph in fig. 4.12(a)). Assuming that this is unchanged over the experimental range of temperatures explored, the attenuation coefficient can be used to create a plot of $\Delta T(at)/(1 - e^{-\alpha t})$ *versus* t, time to yield a slope of $P_W / C_{SYS} m$, allowing P_W to be found. The effect of reducing the bulk water temperature from 20 °C to 5 °C, in steps of 5 °C, clearly shows ultrasonic power amplification, as depicted in fig. 4.12(b).

Two phenomena could support the above observations. In the first instance reduction in temperature will drop off the vapor pressure of the liquid, hence the cushioning effect will get hindered [11] causing efficient cavitation. The second factor of contribution probably stands on the utilization of ultrasonic energy in stretching the bonds and not increasing the degree of freedom of vibrations of atoms (energy indulgence as heat) for effective cavitation at decreasing temperatures.

4.2.2.3.2. Cyclic voltammetry (CV)

Fig. 4.13 shows two of voltammograms recorded during copper electrodeposition onto graphite substrates in absence (a) and presence (b) of ultrasound at a scan rate of 10 mV/s. The scanning ranges are − 0.6 V to + 0.6 V and −0.6 V to +1 V for silent and sonication conditions respectively to ensure complete dissolution of the deposited mass. The silent scan has both cathodic and anodic peaks, while insonated CV has only the dissolution peak. In the cathodic scan, the figure shows that, 20 kHz (136 Wcm−2) [curve (b)], the reduction of copper ions under sonication has an onset potential near +50 mV *vs*. SCE. Figure 4.13 also shows that, in the anodic scan, anodic peak current for the stripping or dissolution of copper on graphite is increased by 4-fold under insonation (b) compared to silent conditions (a). The stirring of solution by the acoustic streaming during the sono-oltammetric scan might have hindered the depletion of electroactive species in the vicinity of the electrodes during deposition which have resulted the increase in cathodic and anodic currents.

Also, the anodic peak potential is shifted to more positive values under ultrasound (20 kHz), $E_{\mathrm{pa,U}}$ = +693 mV *vs*. Ag compared with $E_{\mathrm{pa,S}}$ = +344 mV *vs*. SCE, in otherwords a ΔE of approximately +349 mV under sonication. This displacement of the anodic peak potential is most likely due to the Ohmic drop in the solution. This may be manifested by the sonication effect on the rate of mass transport and other associated effects in the electrochemical bath.

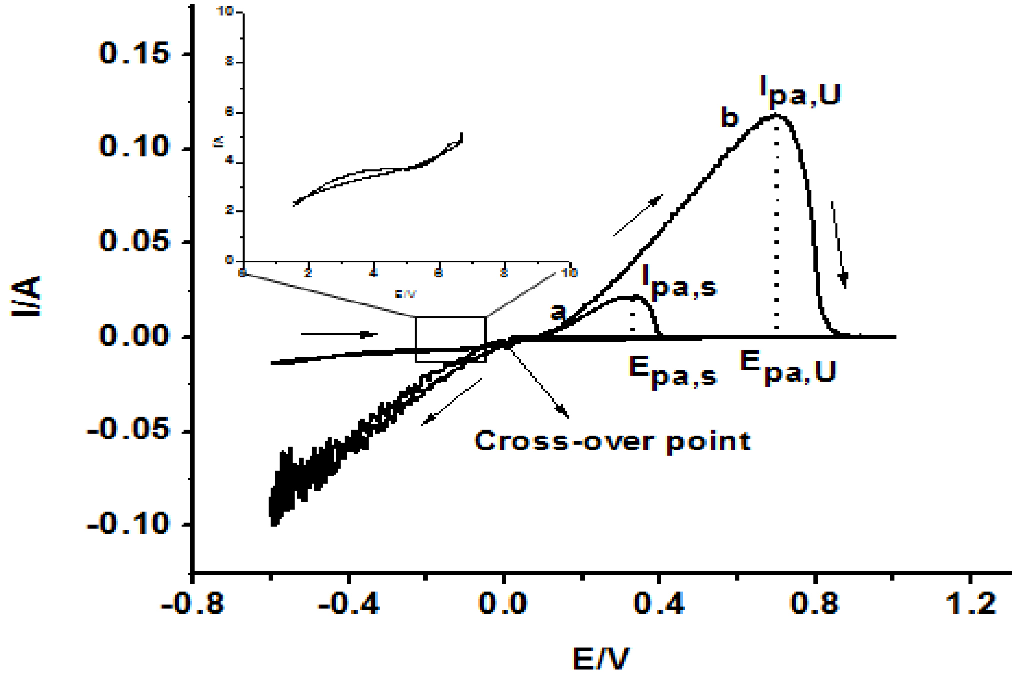

Fig. 4.13. Cyclic voltammetry (Scan rate of 10 mV/s) of copper redox reaction (on graphite) from a solution of 6.35 $\mathrm{g\ l^{-1}}$ ***Cu (II) sulfate and 40*** $\mathrm{g\ l^{-1}}$ ***sulfuric acid at 25 °C in (a) silent and (b) sonication conditions***

In order to identify the kinetics and rate-controlling steps of the electrodeposition of copper, the investigation is now focused on the effects of reducing temperature and ultrasound on the variations of the voltammograms. In the cathodic zone (E < 0 V) of these voltammograms, the Cu(II) reduction process produced different voltammetric characteristics depending on the dynamics of the electrolytic bath. Note in fig. 4.14 that, during the reverse potential scan a crossover on the cathodic branches in silent condition was observed. This feature indicates that copper deposition proceeds via a nucleation and growth phenomena. Apart from the phase kinetic characterization, the cross over potential can be related to the equilibrium potential, in this case $Cu^{2+}(aq)/Cu(s)$, when it is independent of the inversion potential. Equilibrium potential in silent condition has turned out to be a function of temperature, shifting towards more negative values as the temperature decreased.

Similar trend has also been observed by Claudia *et al* [13] for deposition of silver at high temperatures. The silent copper deposition process has developed well-resolved two cathodic (E_{pc1},E_{pc2}) and two anodic peaks ($E_{pa1,}$ E_{pa2}). These peaks may be due to the sequential Cu(I) and Cu(II) redox reactions as observed by [14]. In addition, the overpotentials corresponding to the silent anodic process are practically independent of temperature (see Fig. 4.14); however, the overpotential corresponding to the cathodic peak, η_c is not. Yet again the reduction potential of the starting Cu(I) ions has become more anodic with reduction of bath temperature. It is reasonable to believe that the initial high availability of ions in the ionic atmosphere, because of the opposition on the chaotic atom movement at low temperature values, has increased the tendency of reduction of ions.

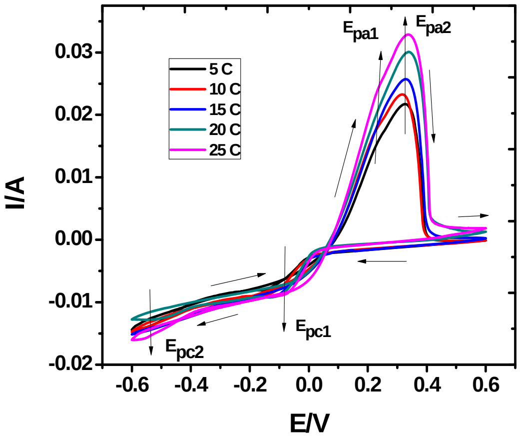

Fig. 4.14. Cyclic voltammetry of copper redox reaction (on graphite) from a solution of 6.35 g l^{-1}*Cu (II) sulfate and 40* g l^{-1} *sulfuric acid at different temperatures in silent condition*

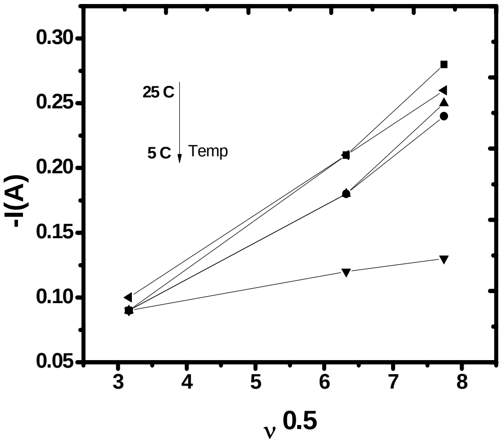

Fig. 4.15. Current density vs. (scan rate)$^{-0.5}$ at different temperatures for silent conditions

Table 4.5: Experimental values for the reversability test obtained from cyclic voltammograms for the electrochemical behavior of Cu/Cu(II) redox couple

Temperature (°C)	ΔE_p (mV) ($E_{pa1} - E_{pc1}$)	$E_p - E_{p/2}$ (mV)	I_{pa}/I_{pc}
25	225	13	0.28
20	200	14	0.30
15	200	14	0.32
10	170	31	0.33
5	160	22	0.45

Along with the diagnostic crossovers, silent voltammograms have two crossover points at higher temperatures. This could be an indication of mixed mass and charge transport limited electrodeposition. However, the dominating phase kinetics phenomena were then better comprehend by performing a set of voltammatric study with different scanning rates. For each redox peak, the peak current I_p is related to scan rate ν by Randles-Sevick [15] equation (2.11). For an ideal reversible system, a plot of I_p vs. $v^{1/2}$ should be linear. These plots were constructed for the graphite electrode at different temperatures and are shown in fig. 4.15. It can be seen that the relationship are mostly linear at all deposition temperatures in silent conditions. This could be an indication of mixed (quasi-reversible) rate kinetics of the process. Applying the criteria detailed in [16], the reduction couple is in fact quasi-reversible as the separation between the anodic and cathodic processes are greater than *59/n* mV, where *n* is the number of electrons transferred in the process. The list of diagnostic parameters for the kinetics study of the silent process is given in Table 4.5. The initial reduction (E_{pc1}) and dissolution peak (E_{pa1}) values and their data are used for the reversibility characterization. It was also noted that the quantity of Cu deposited increased with temperature, such that at 25 °C the amount was four times larger than that obtained at 5 °C.

All sono-voltammograms (Fig. 4.16) have tended to area of stability at high potentials i.e. a limiting current, which depends on the magnitude of the diffusion layer thickness [17,18], according to, $I_{lim} = {nFADC^*}/{\delta}$. Where I_{lim} is the limiting current (A), n is the number of electrons transferred during the electrochemical process, F is the Faraday constant (96,500 C mol^{-1}), A is the electrode area (cm), D is the diffusion coefficient (cm^2 s^{-1}), C^* is the concentration of the species in the bulk solution (mol cm^{-3}) and δ is the diffusion layer thickness (cm).

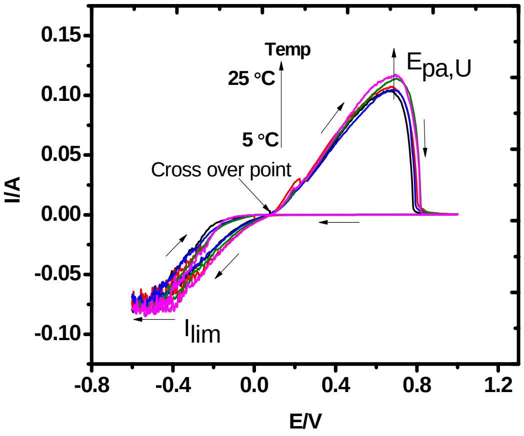

Fig. 4.16. Cyclic voltammetry of copper redox reaction (on graphite) from a solution of 6.35* g l^{-1} *Cu (II) sulfate and 40* g l^{-1} *sulfuric acid at different temperatures in sonicated condition

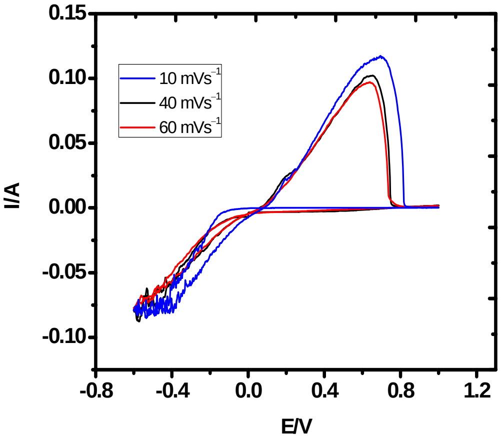

Fig. 4.17. Cyclic voltammetry for the electrochemical behaviour of 6.35* g l^{-1}*Cu (II) sulfate and 40* g l^{-1} *sulfuric acid (on graphite) under insonation at 25 °C at sweep rates: (i) 10 mVs^{-1}, (ii) 40 mVs^{-1} and (iii) 60 mVs^{-1}

Further this value can be used to calculate the mass transfer co-efficient k_d from the formula, $k_d = \frac{I_{lim}}{nFC}$, which characterizes the mass transport conditions from and/or towards electrode surface and, therefore, denotes a local measurement of the hydrodynamic conditions. The quantity varies from 5.9 – 6.54 × 10^{-3} with increase in temperature. The copper reduction process in presence of ultrasound has occurred without formation of cathodic peaks. The absence of cathodic peaks for the insonated working electrodes may indicate an ample availability but slow discharge of reducing ions at the electrode surface. And the potential crossovers are present in the positive potential region in CV curves. This is consistent with no significant depletion of the active species at the electrode surface, and, therefore may imply charge (or interfacial) control kinetics. Moreover the scans with increasing scan rates (Fig. 4.17) show a decrease in peak height (I_{paU}) in contrary to the conventional increase in peak values. This may further compliment the charge transfer controlled sonicated reactions. Further the scans have two effects on the deposition part of the transient. The potential required for deposition to begin becomes less negative, and the amount of charge transferred increases steadily. The scans also have irregularities. This can be explained by a combination of rapid random changes in the surface ion concentration and ablation of material at the electrode surface.

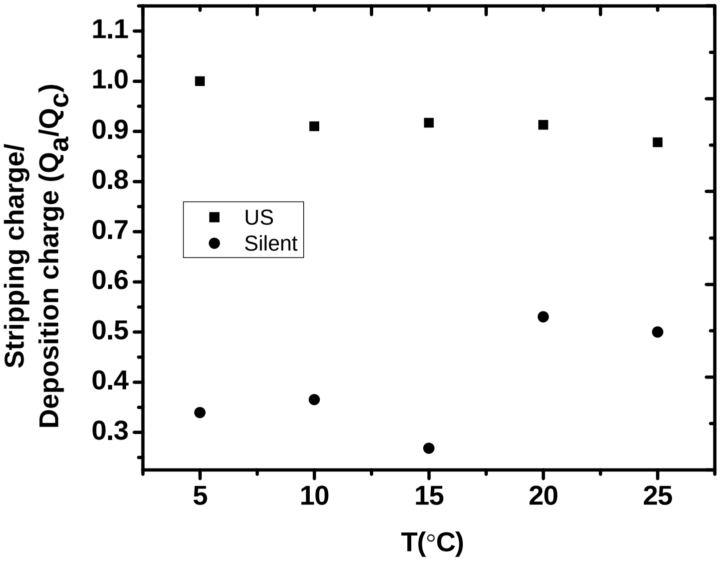

Fig. 4.18. Stripping charge/Deposition charge (Q_a/Q_c) for silent and sonicated deposits (on graphite) as a function of temperature.

To analyze the deposition efficiency of the process, charges due to the cathodic (*Q*c) and anodic (*Q*a) processes can be obtained from integration of the cathodic and anodic branches of the *I-E* curves, respectively. Fig. 4.18 shows plots of the *Q*a/*Q*c ratio as a function of temperature for Cu deposition from solutions with and without sonication. In case of sonicated copper formation, the *Q*a/*Q*c ratio reached a value of 1 as temperature became lower. This indicates that copper deposited during the cathodic sweep potential has dissolute only by electrochemical anodic scan. And as all the deposited Cu has got dissoluted by Faradic reaction (not by ablation), the deposit should have good adherence with the substrate. In contrast, the *Q*a/*Q*c ratio for silent copper formation reached a maximum value of 0.5 for the temperature range considered. The difference between the anodic and cathodic charges (*Q*a and *Q*c) observed in this case could be explained in terms of some process coupled to the cathodic reaction. In other words, this result supports the presence of simultaneous cathodic processes or side reactions (that can consume electrons) besides Cu^{2+} reduction. The main characteristic of these side reactions are that the product cannot undergo oxidation during the anodic scan.

Since the only difference between the deposition baths is the presence of ultrasound, it is likely that an interaction between newly deposited copper and sulfate ions in solution is occurring in silent bath. Thus the total set of reactions taking place at the cathode may include a direct copper reduction reaction, interaction of sulfate ion with the copper ions forming complex compounds and/or sulfate reduction on the surface of the copper nuclei. The interaction of sulfate ion with the copper ions would consume the copper deposit and sulfate ion would provide electrons to the external circuit. The presence of sulfur and oxygen in silent deposits and corresponding cleaner depositions in presence of ultrasound is confirmed in section 4.1. Hence, together or separately, these reactions explain the low Cu recovery efficiency recorded for silent copper formation.

4.2.2.3.3. Nucleation and growth mechanism of copper formation

The nucleation phenomenon corresponds to the initial stage of copper electro-formation. It can be considered as the most critical stage of growth for definition of the final film properties [19]. The most widely used technique to capture and quantify the kinetics is a single step constant over voltage scan, chronoamperometry (CA). Based on the cathodic zone of the CV experimentation the reduction potential, $E_c = -$ 300 mV, was chosen. The effect of temperature on *i(t)* curves were recorded during silent and sonication copper formation. The current-time evolution associated with the two conditions differed depending on the association of ultrasound with the electrolytic bath. This feature indicates that different crystallization mechanisms could be associated with Cu deposition from the two baths. Hence the two cases have been discussed separately and comparisons are made accordingly.

(i) Silent electrodeposition

The silent current transients (fig. 4.19) are similar to those observed for copper deposition involving nucleation and growth processes on different electrodes [20-22]. At very short time, an increase in the current density is observed and a maximum value, I_{max}, is reached at the time t_{max}. The current peak is followed by a decreasing part of the transient, which corresponds to the current limited by the diffusion of Cu(II) species. The crystallographic misfit between the graphite and Cu atoms may favor a 3D nucleation and growth behavior, since the surface of vitreous carbon consists of randomly oriented sp^2 carbon atoms, while copper atoms require ordered cryastallization in face-centered cubic geometry [15]. Hence the Scharifker and Hills (SH) model was considered first in order to characterize the nucleation process [23]. When the deposition temperature is varied from 25 °C to 5 °C, there is a sharp gradual increase of I_{max}, from 8 to 12 mA and t_{max}, shifts from 2.4 to 1.6 s. Accordingly the nucleation rate is believed to be enhanced with decreased temperature. However, from the CV experiments the amount deposited has a reverse trend than that of the constant overpotential experiments. To explain the above discrepancy, we hereby serve our logic based on the model proposed by D'Ajello *et al* [24], for the critical radius of reaction. The whole system can be separated into two regions, the Brownian and non-Brownian (fig. 4.20). Non-Brownian region is either the exact or the close proximity to the reaction radius. Here the reaction takes place by the migration of the ions and not by diffusion.

The reduction in bath temperature would have probably increased the availability of ions inside the non-Brownian or the actual ion reduction zone, where only the mass transfer by migration predominates. For this reason, the progress in temperature towards lower values will have non-Brownian dominated nucleation phase kinetics. As a result the lowest temperature should have the lowest rate of growth (because growth of the nucleated atoms needs Brownian mass transport from the bulk of solution to the interphase) and highest rate of nucleation because of the initial high level of supersaturation near the electrode surface. From a thermodynamic point of view the effect can be explained on the fact that, the energy barrier that the ions have to surmount for an adatom formation is an obvious function of temperature. Decreasing temperature increases the level of supersaturation. Hence, the activity of ions will increase and the critical nucleating condition will occur at low temperature. Supersaturation determines the degree of metastability in the parent phase. This non-equilibrium cluster energetic will increase the nuclei population density, which can lead to a high nucleation rate. The growth kinetics of the clusters past the critical cluster size will get reduced as attachment of further atoms to the cluster decreases due to increased diffusion barrier. This decorum can readily be observed from the plots (fig. 4.19). Higher temperatures have low nucleation currents while low temperature depositions transients have low growth currents. Moreover these low temperature growth currents have decreasing tails and are lower than the growth current at 25 °C for longer periods of depositions.

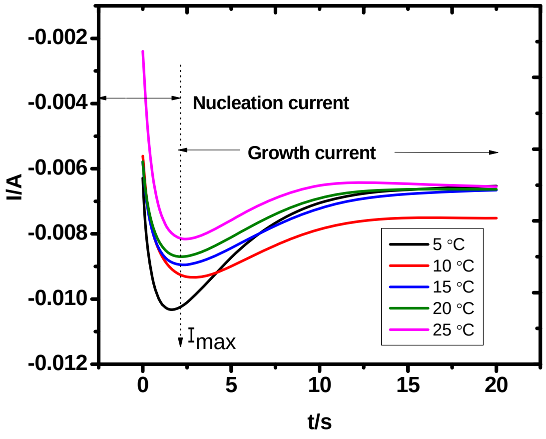

Fig. 4.19. Chronoamperograms of silent copper deposits (on graphite) as a function of temperature

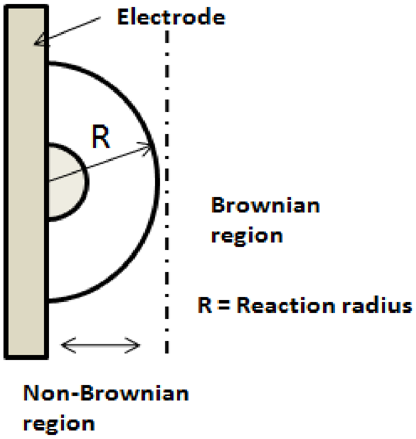

Fig. 4.20. Reaction regions at the electrode/electrolyte interphase

To validate the above hypothesis the mode of appearance of the nuclei on the depositing substrate should be modeled. The SH model [23] allows simple classification of the experimental transients into two limiting nucleation mechanisms, instantaneous or progressive. Instantaneous nucleation (equation (4.4)) activates the substrate surface at a time, while progressive nucleation (equation (4.5)) corresponds to activation during the course of electro-reduction. The non-dimensional plots of $(I/I_{max})^2$ versus t/t_{max} coordinates fall at either of these two limiting cases.

Fig. 4.21 presents the experimental transients plotted in reduced current-time coordinates, together with the theoretical curves for instantaneous and progressive, for different temperatures. As indicated in fig. 4.21, the fit of the experimental data with the theoretical curves are much better for instantaneous nucleation at all temperature ranges. The established model explains the two limiting cases on the basis of availability of substrate's active sites and concentration of depositing species near the interphase.

$$(\frac{I}{I_{max}})^2 = \frac{1.9542}{(\frac{t}{t_{max}})}\{1 - \exp\,[-1.2564(\frac{t}{t_{max}})]\}^2 \quad (4.4)$$

$$(\frac{I}{I_{max}})^2 = \frac{1.2254}{(\frac{t}{t_{max}})}\{1 - \exp\,[-2.3367(\frac{t}{t_{max}})^2]\}^2 \quad (4.5)$$

The active sites on the cathode factor can be assumed to be constant if proper surface treatment measures have taken prior to deposition, whilst the second factor may vary depending upon the bath thermodynamics and electrochemical potential. Presuming that nucleation sites are same for all the bath conditions, the derived mode of instantaneous phase appearance seems to be quite convincing.

For an instantaneous nucleation, the nuclei number density may be calculated from eq. 4.6:

$$N = \frac{186.245}{(I_{max}t_{max})^2} \quad (4.6)$$

Cottrell equation was used for calculation of D. When the individual diffusion zones eventually overlap, encompassing the entire electrode surface area, the reaction comes to a steady state as described by the Cottrell equation.

$$I(t) = \frac{nFD^{1/2}C_0}{\pi^{1/2}t^{1/2}} \quad (4.7)$$

According to the equation the diffusion of the reacting species can be determined from a slope of chronoamperograms in I versus $t^{-0.5}$ coordinates. Since the initial part of the current transient deviates from the Cottrell equation because of the nucleation process, linearization can be performed only after the reduction reaction becomes limited by planar diffusion i.e. beyond the peak stage of chronoamperogram. Table 4.6 summarizes the values of N and D obtained for various temperature ranges. The effect of temperature driven supersaturation and diffusion limited growth can clearly be observed from the calculated data.

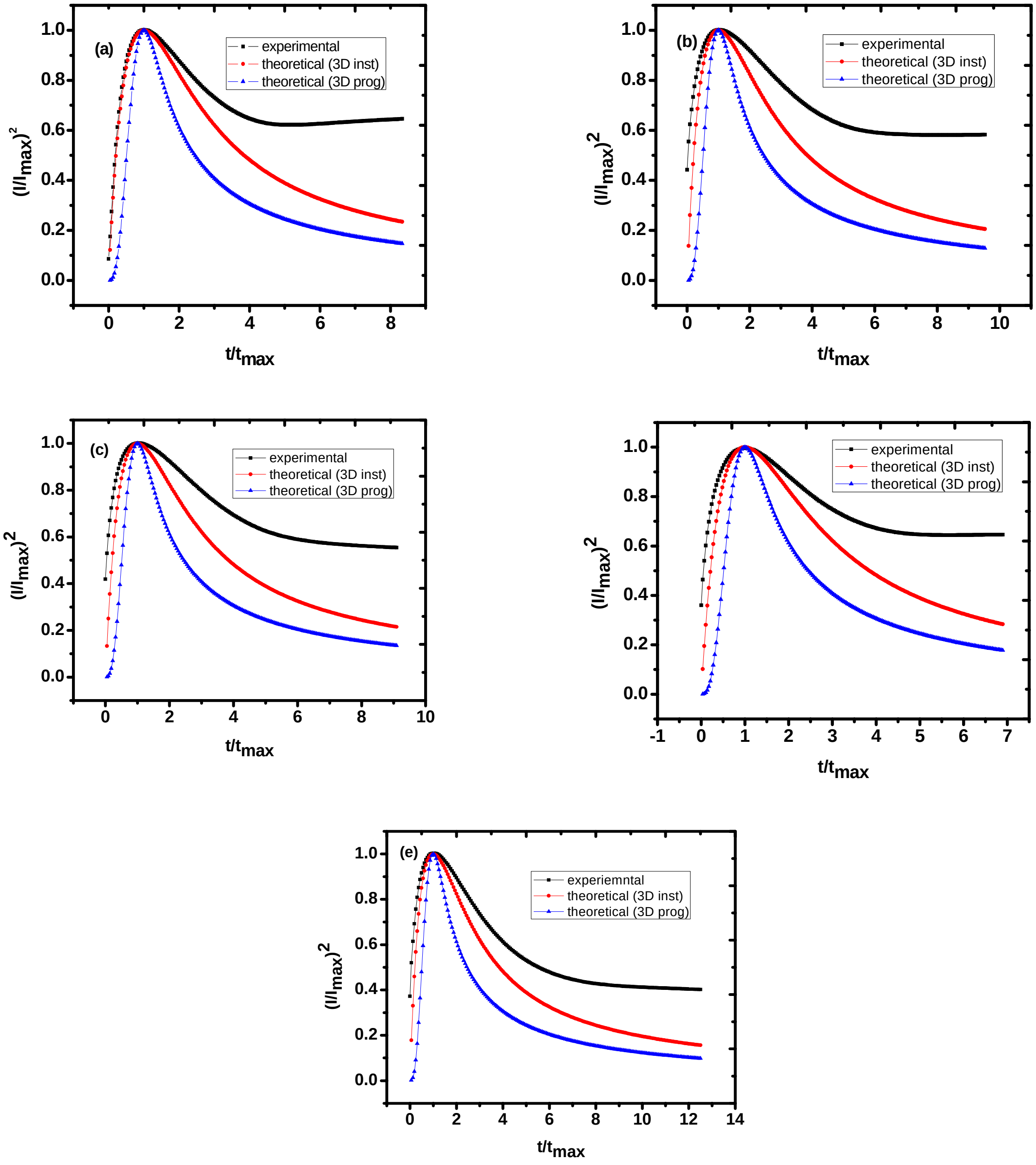

Fig. 4.21. Reduced time vs. reduced current plots for the chronoamperometric data in fig. 4.19; (a) 25 °C, (b) 20 °C, (c) 15 °C, (d) 10 °C and (e) 5 °C temperatures

Figs. 4.22(a-e) shows the topographies of the graphite electrodes modified at different temperatures of 25, 20, 15, 10 and 5 °C respectively. From a fixed solution a clear change in the morphology, uniformity and density of Cu nuclei of deposits was observed as a consequence of the variation of temperature. There is an adaptation of dendritic structures to non-dendritic and spherical grain morphology for low temperature depositions.

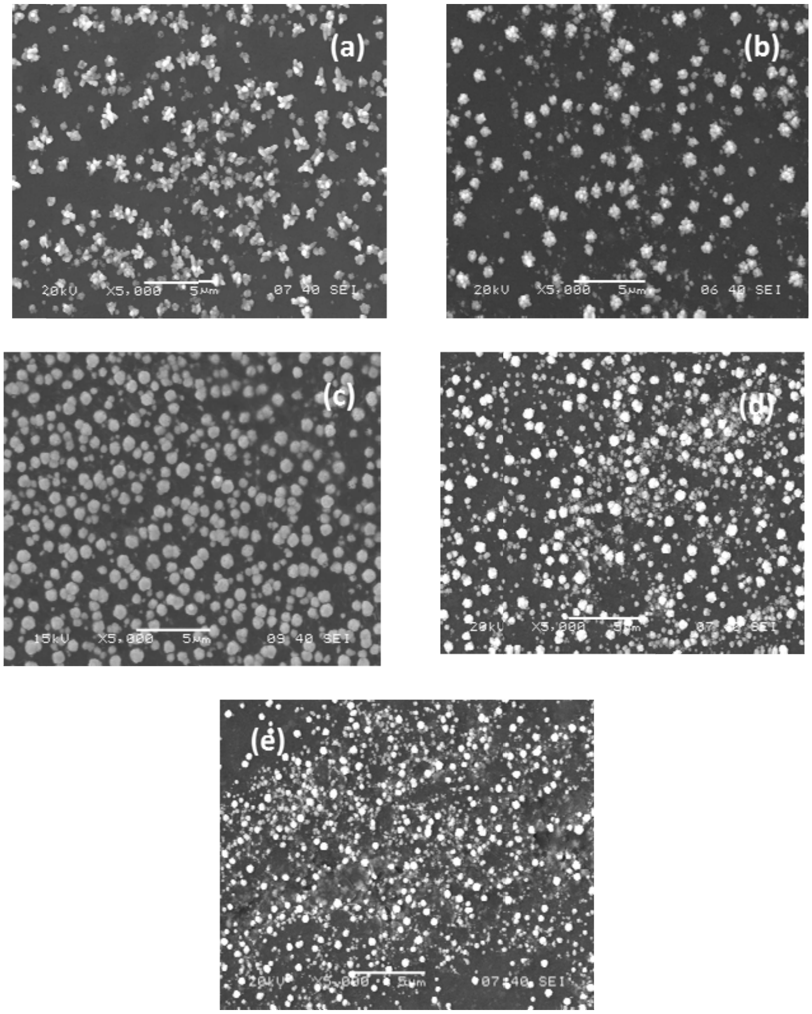

Fig. 4.22. SEM micrographs of silent copper deposits(on graphite) at (a) 25 °C, (b) 20 °C, (c) 15 °C, (d) 10 °C and (e) 5 °C temperatures

This morphological transition can be an indication of changeover of a muddled system to a more stable one, because dendritic growth is an isothermal and isoconcentrated type of surface movement stabilized by the anisotropy in the surface tension and phase kinetics [25].

Indeed, an increase in the number of nuclei is observed upon shifting the temperature to low values. The values of nuclei population density are summarized in Table 4.6. The nuclei population density increases from about 7.5×10^{3} cm^{-2} (Fig. 4.22a) to 2.6×10^{4} cm^{-2} (Fig. 4.22c) upon changing the deposition temperature from 25 °C to 5 °C. For the former, the Cu deposit covers about 30% of the surface (Fig. 4.22a) and for low temperature depositions the coverage has increased very nominally. The increase in nuclei population, observed when the temperature is made low, results in a decrease in the distance between two neighboring nuclei and allows an early overlapping of diffusion zones. The eventual overlap will inhibit the total amount of material available to a nucleus. This in turn might have resulted fine copper spheroids. To get the beneficial effects of this fine symmetrical grains the films should have adequate continuity and ultrasound is experimented in that line as discussed in the next section.

(ii) Sono-electrodeposition

Two-Point Golay–Savitzky normalized sono-chronoamperometry transients are shown in fig. 4.23.

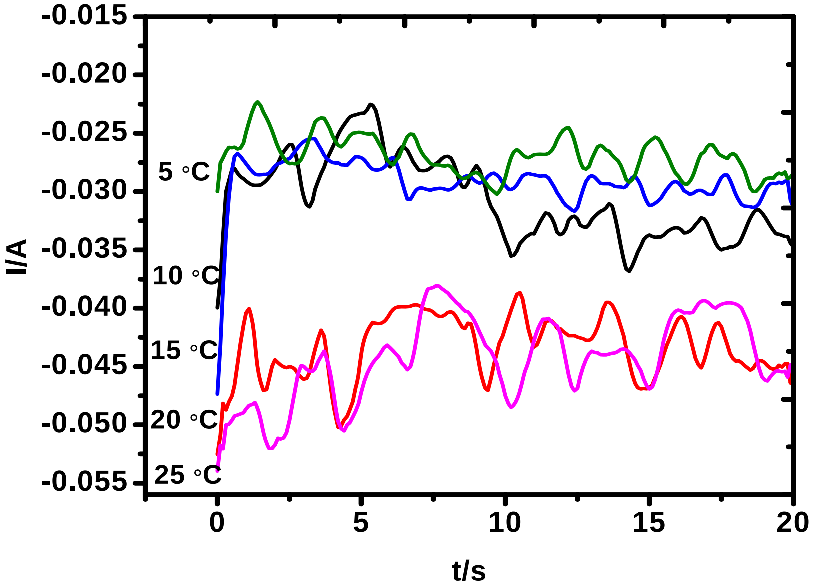

Fig. ***4.23. Chronoamperograms of sonicated copper deposits (on graphite) as a function of temperature.***

In the presence of ultrasound emitted from a horn probe at a 5 mm distance from the working electrode, sonication was found to have three distinct effects on the current transients: (1) increase in deposition currents (2) random fluctuation in the observed current, and (3) opposite trend then that of the silent potential scans i.e. 25 °C temperature CA has the maximum initial nucleation current.

Increase in current attributed to enhanced mass transport has been investigated and established [26-28] by various researchers. The indiscriminate current variation results are similar to that of our previous work on the mechanism of nucleation in presence of ultrasound [3]. These current fluctuations are because of sequential nucleation and growth cycles, the first being the primary nucleation and the rest are secondary nucleation on the existing primary nuclei due to crystal fragmentation. At higher temperatures the number of these current fluctuations has decreased. The variations of this mechanism with temperature can be explained on the applied ultrasound intensity and the effects associated there in. At sufficiently high intensities (~ 300 W cm^{-2}) the effect of power ultrasound on the mass transport becomes temperature independent [29]. But what if the intensity is low and the system itself utilizes the ultrasonic energy more towards the transient cavitation and not into kinetic and thermal energy with decreasing temperature? The ultrasonic intensity delivered to the bath increases from 134 – 177 W cm^{-2} as the temperature decreased from 25 °C to 5 °C. In agreement with other reported trends [30,31], current spikes are found to be increased with increasing ultrasound intensity (and hence decreasing temperature). Hence the cavitation process becomes more violent at low temperatures. As a result there possibly will be intense crystal fragmentation and localized supersaturation at reducing temperatures. Consequently the deposits may have better surface coating and comparable grain morphology to their silent counterparts, as both the effects of increased level of supersaturation and crystal fragmentation will trigger primary and secondary nucleation respectively. This possibility is better comprehended in the next section of morphological analysis. Moreover these logics could make us able to correlate the opposite effects of silent and sonication on the experimental transients. A quantitative comparison between the cavitation driven nucleation mechanism to that of silent is presented in Table 4.6. Nuclei number density (*N*) and diffusion coefficient (*D*) of the primary nucleation is taken into consideration as secondary nucleation will add obvious data. In all the temperature ranges sonicated bath has nucleated more number of nuclei. Small fluctuations in the number densities may be due the ablation effect of ultrasound. Now comparing the cathodic charge generated in the due process, it is high at low temperatures which might be because of the increased number of intense nucleation cycles.

Table 4.6: Kinetic parameters of copper deposition under silent and insonation conditions

Temperature (°C)	**$D \times 10^{-5}$ (cm^2 s^{-1})**		**N (cm^{-2})**		**Charge consumed (C)**	
	Silent	Sonication	Silent	Sonication	Silent	Sonication
25	2.07	87	7.50×10^3	5.10×10^6	0.137	0.538
20	1.77	35	1.26×10^4	8.70×10^6	0.145	0.584
15	1.71	19.5	1.30×10^4	1.70×10^6	0.150	0.611
10	1.55	18	1.63×10^4	1.57×10^6	0.162	0.867
5	1.08	13	2.60×10^4	3.50×10^6	0.153	0.887

It is known that the morphology of deposits is affected by the extent of mass transport control, and that often the quality of films deposited under charge transfer control is better than under mass transport control [32]. Thus the effect of ultrasonic wave on deposit topography was investigated.

Fig. 4.24 shows the SEM micrographs of the sono-electrodeposited thin films. The original morphology of the particles is approximately spherical with the diameter varying between 400 nm and 1 µm. It also seems that each particle is composed of a series of small particles (in the range of 30–50 nm.) which could not grow separately and aggregated to each other to form particles of larger size. Decrease in temperature results in a series of aggregated particles. Investigating on the surface coverage aspect, sono-electrochemically deposited films have good uniformity than the silent depositions. A nearly absolute coverage of the surface is achieved at 5 °C. In the case of a complete continuity of the deposits, the electrodeposition of Cu may follow two different mechanisms [33]. Firstly, the deposition occurs on the bare graphite surface and the first Cu nuclei are formed. In the initial stage, Cu is deposited preferentially on the surface steps and on the defects of graphite.

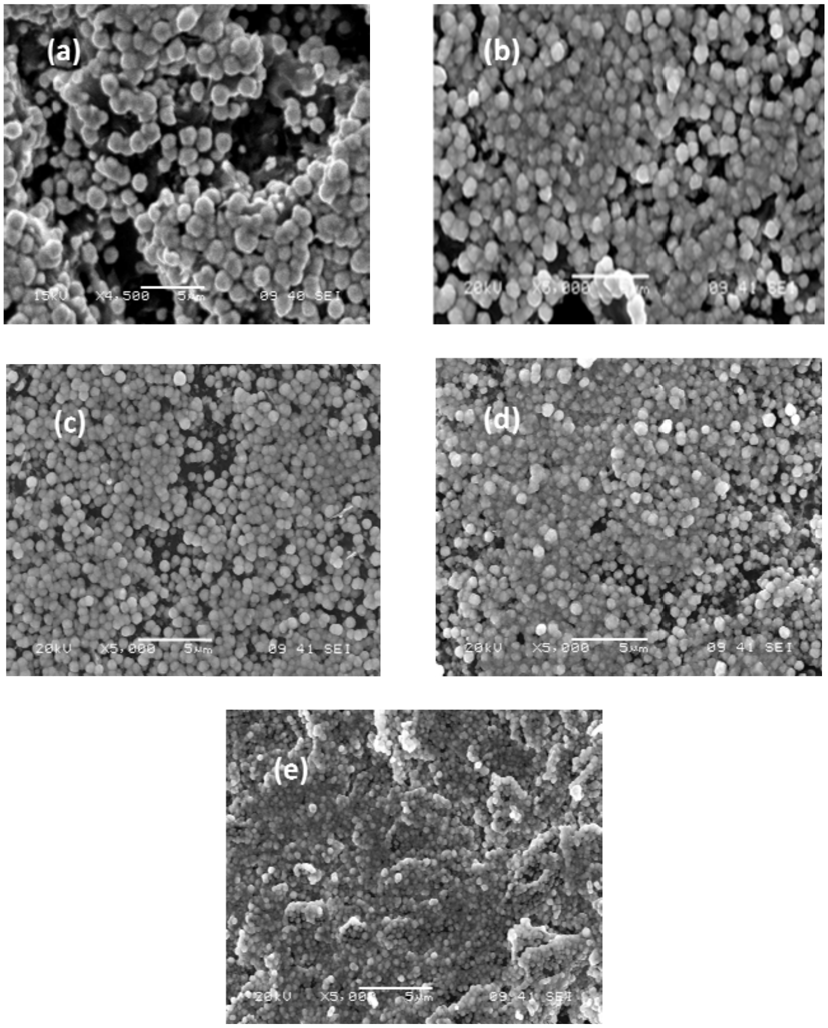

Fig. 4.24. SEM micrographs of sonicated copper deposits (on graphite) at (a) 25 °C, (b) 20 °C, (c) 15 °C, (d) 10 °C and (e) 5 °C temperatures

Afterward, the nuclei population density increases and the Cu deposit expands on the totality of the surface. Secondly, a continuous deposition of Cu occurs on the freshly deposited Cu particles. Likewise these processes result in smoother uniform surface. Such control of the Cu particles distribution on vitreous graphite is only feasible if there is a continuous mass (ions) supply to the electrode/electrolyte interface (double layer). Hence the two path-ways are quite possible from a depositing bath where there is continuous stirring, extreme level of supersatuation (due to both temperature and sonication), possibility of secondary nucleation and surface activation. However, the continuous surface cleaning (ablation) effect under insonation may rule out both the mechanisms and thus creating a zone of intricacy for uninterrupted instantaneous Cu phase nucleation and distribution.

Now the nucleation path way followed in the due process can be explained from the data presented in Table 4.6. The percentage of primary nuclei in sonicated conditions is two orders higher, which might have certainly increased the surface uniformity from 30% in silent conditions to 60% in sonication condition. The rest surface occupancy may possibly have been contributed by secondary nucleation. Hence insonation would have induced a nucleation mechanism which is combinations of the above two mechanism either occurring sequentially or simultaneously to from a superior deposit in terms of grain size, shape and distribution. Accordingly the best morphology with fine particles and good distributions was obtained for the deposit at 5 °C temperature. The surface profile and critical grain information are performed by phase mode (−90° to +90°) AFM studies (Fig. 4.25). The appearance of the deposits is similar to that obtained by SEM experiments. Phase imaging goes beyond simple topographical mapping to detect variations in composition, adhesion, friction, viscoelasticity, and numerous other properties. Here we have coupled the phase mode micrographs with the z height instead of phase angle to visualize the surface uniformities in terms of their properties as well as profile. The aggregation of fine particles to form the big spherical clusters can better be clarified from the figures. Except the cluster boundaries the inter-cluster regions are in phase, which means the surface is free of discontinuities in terms of contaminants and preferential growth (dendritic growth). Further a single particle scan for the deposition at 5 °C (fig. 4.25d) has been performed for a detailed study of the surface texture.

Table 4.7: AFM analysis parameters of sonicated copper deposits at different bath temperatures

Temperature (°C)	**R_a(nm)**		**Critical dimension (nm)**		**Z level (95% BR) (nm)**	
	Whole	Single	Whole	Single	Whole	Single
25	248	89	680	116	593	861
15	194	51	500	103	382	582
5	90	30	390	60	316	439

The single particle of 360 nm size was found to be a coalescence of large number of small particles (of 40-60 nm size) with average roughness (R_a) of 30 nm. Bearing ratio (BR) analysis shows that, 96.5% of the total particle height is above 439 nm and only 2% above 800 nm which results a R_a of 90 nm for the whole surface. The definition of bearing ratio is the percentage of total data appearing above the selected Z level, hence higher the BR for the minimum Z level will be an analysis of smooth surface. Average roughness factor, Z level corresponding to 95% BR and critical dimension of bigger as well as the aggregating small particles for all deposition surfaces are presented in Table 4.7.

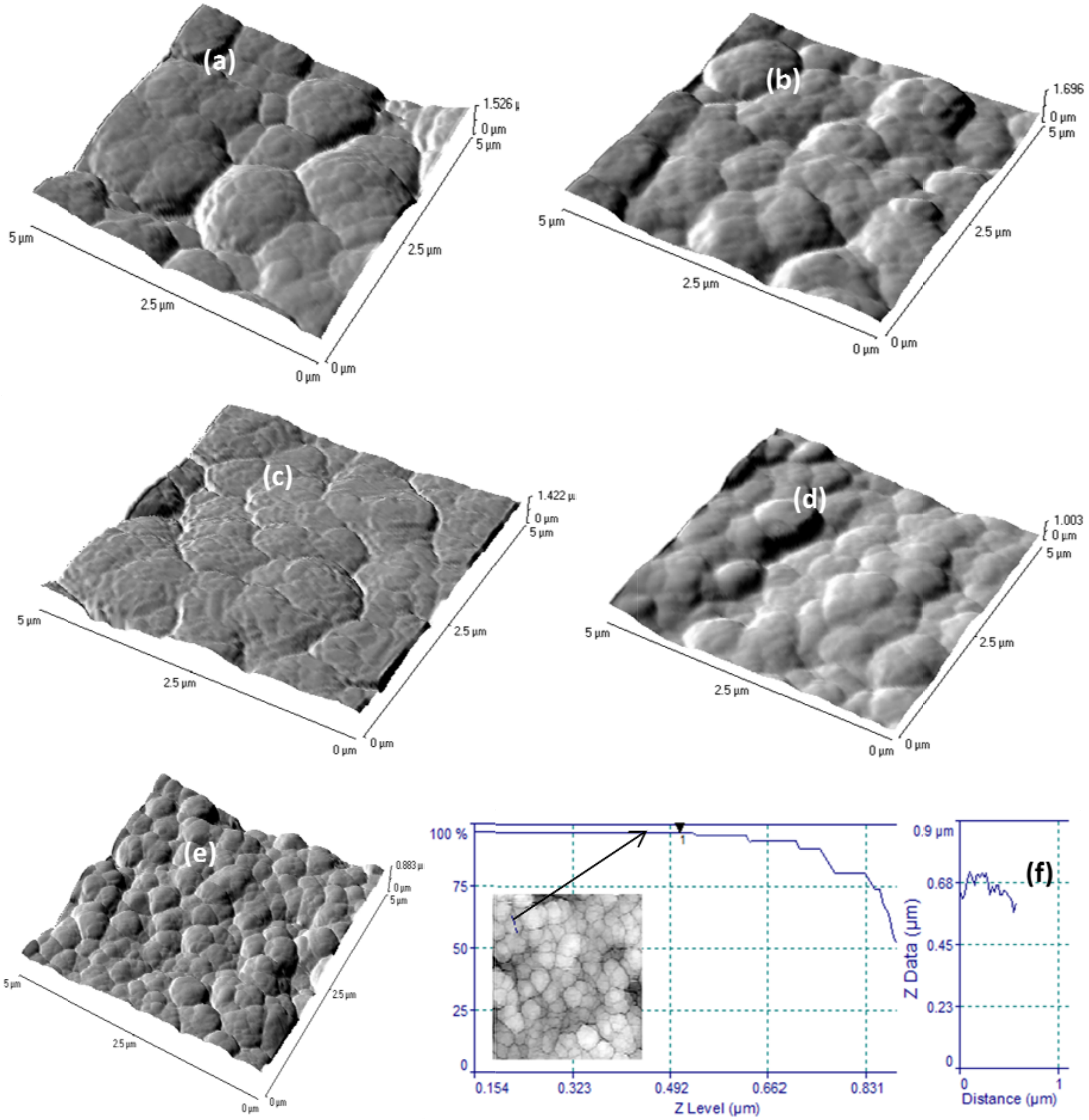

Fig. 4.25. AFM phase micrographs of sonicated copper deposits (on graphite) at (a) 25 °C, (b) 20 °C, (c) 15 °C, (d) 10 °C (e) 5 °C temperatures and (f) 2D micrograph with calculated BR and height profile at 5 °C

R_a varies from 220 nm to 90 nm as the deposition temperature decreases. The table confirms the deposition at 5°C to be of the highest surface finish. These observations may affect the state and intensity of depositing residual stresses and hence the de-lamination characteristics of the deposited films onto the substrate, which is discussed in the following sections.

4.2.2.4. Summary

It has been shown to be beneficial to employ power ultrasound to assist electrochemical deposition of copper at low temperatures. The Cu deposits were formed potentiostatically and characterized by electrochemical methods, scanning electron microscopy, and atomic force microscopy. It was found that the deposition of copper in the absence of ultrasound had mixed mass and charge transfer kinetics. Copper nucleated according to 3D instantaneous mechanisms for all temperature ranges. The extent of nucleation was found to be increased at low temperatures with a transition of dendritic type morphology to spherical copper deposition. On the other hand, the deposition kinetics was mainly dominated by charge transfer in presence of ultrasound. Diffusion coefficients and nuclei population density were calculated for each temperature range for both presence and absence of ultrasound, both the quantities increased in presence of ultrasound. Although Scharifker equations seem to demonstrate an instantaneous nucleation under sonication they are not entirely suitable to explain this behaviour and a new mathematical model should be considered. Furthermore sonicated deposits with good surface coverage were found to consist of spherical copper agglomerates of nanosized particles. The results suggest that the effect of power ultrasound on electrochemical systems under a wide range of conditions is non-conventional.

4.2.2.5. References

1. D. M. Stefenescu, Ed., Metals Handbook, Vol. 15, ASTM International, Ohio, 1988.
2. S. Devarakonda, J. M. B. Evans, A. S. Myerson, Crys. Growth Des., 3 (2003) 741.
3. R. Chow, R. Blindt, R. Chivers, M. Povey, Ultrasonics, 43 (2005) 227.
4. M. E. Hyde, R. G. Compton, J. Electroanal. Chem., 531 (2002) 19.
5. C. E. Banks, R. G. Compton, A. C. Fischer, I. E. Hanley, Phys. Chem. Phys. Chem., 6 (2004) 3147.
6. C. E. Banks, R. G. Compton, Electroanalysis, 15 (2003) 329.
7. P. E. de Jongh, D. Vanmaekelbergh, and J. J. Kelly, Chem. Mater., 11 (1999) 3512.
8. J. S. Santos, R. Matos, F. Trivinho-Strixino, E. C. Periera, Electrochim. Acta, 53 (2007) 644.
9. S. Zein El Abedin, A.Y. Saad, H.K. Farag, N. Borisenko, Q.X. Liu, F. Endres, Electrochim. Acta, 52 (2007) 2746.
10. M. A. Margulis, I. M. Margulis, Ultrason. Sonochem, 10 (2003) 343.
11. T. J. Mason, J. P. Lorimer, D. M. Bates, Ultrasonics, 30 (1992) 40.
12. B.G. Pollet, S.S. Phull, Recent research developments in electrochemistry, Transworld Research Network Publisher, India, 2001.
13. C. Ramı´rez, E. M. Arce, M. Romero-Romo, M. Palomar-Pardave, Solid State Ionics, 169 (2004) 81.
14. B. G. Pollet, J-Yves Hihn, T. J. Mason, Electrochim. Acta, 53 (2008) 4248.
15. Southmpton Electrochemistry Group, in: T. J. Kemp (Ed.), Instrumental Methods in Electrochemistry, Ellis Horwood Ltd., Chicster, UK, 1985.
16. J. Bard, L. R. Faulkner, Electrochemical methods: Fundamentals and applications, John Wiley and Sons, USA, 2001.
17. E. L. Cooper, L. A. Coury, J. Electrochem. Soc., 145 (1998) 1994.

18. J. P. Lorimer, B. Pollet, S.S. Phull, T.J. Mason, D.J. Walton, U. Geissler, Electrochim. Acta, 41 (1996) 2737.
19. A. Milchev, Electrocrystallization: Fundamentals of Nucleation and Growth, Kluwer Academic Publishers, Massachusetts, USA, 2002.
20. A. Milchev, T. zapryanova, Electrochim. Acta, 51 (2006) 2926.
21. N. Tantavichet, S. Damronglerd, O. Chailapakul, Electrochim. Acta, 55 (2009) 240.
22. M.R. Majidi, K. Asadpour-Zeynali, B. Hafezi, Electrochim. Acta, 54 (2009) 1119.
23. Scharifker, G. Hills, Electrochim. Acta, 28 (1983) 879
24. P. C. T. D'Ajello, M. A. Fiori, A. A. Pasa, and Z. G. Kipervaser, Journal of The Electrochemical Society, 147 (2000) 4526.
25. H. Fredriksson, Mater. Lett., 5 (1987) 414.
26. A. Ye. Baranchikov, V. K. Ivanov, Y. D. Tretyakov, Ultrason. Sonochem., 14 (2007) 131.
27. A. Durant, H. Francois, J. Rrisse, A. kirsch-Demesmaeker, Electrochim. Acta, 41 (1996) 277.
28. H. Li, H. Li, Z. Guo, Y. Liu, Ultrason. Sonochem., 13 (2006) 359.
29. A. Beckmann, B.A. Coles, R.G. Compton, P. Gru¨ ndler, F. Marken, A. Neudeck, J. Phys. Chem. B, 104 (2000) 764.
30. F. J. Del Campo, A. Neudeck, R. G. Compton, F. Marken, J. Electroanal. Chem., 477 (1999) 71.
31. J. L. Hardcastle, J.C. Ball, Q. Hong, F. Marken, R.G. Compton, S.D. Bull, S.G. Davies, Ultrason. Sonochem., 7 (2000) 7.
32. R. Winand, Electrochim. Acta, 39 (1994) 1091.
33. O. Ghodbane, Lionel Rou´e, Daniel B´elanger, Electrochim. Acta, 52 (2007) 5843.

4.3. A study on growth behavior of deposited thin films

Materials in this form, micropolycrystalline films, are unstable and their properties change if the temperature is changed. Imperfections are gradually eliminated and the component crystallites increase in size. At high temperatures with materials having a relatively high surface mobility and a low adhesive energy to the substrate, aggregation may occur with the formation of discrete crystallites and the appearance of discontinuities in the films. Hence the inherent instability of these films must always be taken into account when physical measurements are made with them.

4.3.1. Introduction

Growth is liable to corrupt the properties of a deposit and defeat the purpose of deposition at the first place. In as-deposited polycrystalline Cu thin films an order of magnitude increase in grain size, a reduction of electrical resistivity by ~20% towards the bulk value, lowering of Vickers' micro-hardness by ~40%, stress relaxation and change of texture have been observed [1-3]. However, as-plated Cu films are unstable at room temperature, exhibiting a property known as self-annealing [4]. These growth driven detrimental effects may be attributed by the structure or stress or both. The microstructural components contributing towards the above said growth behavior may include grain boundaries, stacking faults, dislocations, surface energy, elastic strain, pinning particles. However, the stored energy at the stacking faults, dislocations, elastic strain do not make a significant contribution in driving the growth phenomena [3,5,6] as comparison to grain boundaries and surface energy. Then again, depending upon the size and grain habitats there are quite a few established phenomena guiding the growth parable enlisted in Harper *et. al* [1] and the references there in. The mechanisms may lead two modes of grain growth i. e. normal and abnormal decided by the size and film relationship. The normal grain growth is characterized by the steady state behavior for which grain size distribution remains mono-modal, self similar and has a time invariant shape. If the grains grow just twice the thickness of the film, then the normal growth can be expressed for an isothermal temperature treatment as [7-9]

$${G_f}^2 = G_0^2 + Kt \qquad (4.8)$$

where G_f is the mean grain diameter of the grains of grown films treated at different temperatures, G_0 is the mean grain diameter of the as-deposited film and t is the annealing time.

This section is written based on the unpublished articles

A. Mallik, B. C. Ray, An understanding of the non-isothermal growth behavior of sono-electroplated Cu thin film, **Thin Solid Films (TSF-D-10-02791)** .

A. Mallik et. al. A study on ex-situ non-isothermal grain growth behavior of sono-electrochemically deposited Cu thin films, **International Journal of Materials Science (Accepted).**

The parameter K is written as [8]

$$K = \left(\frac{K'}{T}\right) \exp\left(-\frac{\Delta G^a}{KT}\right) \qquad (4.9)$$

where K’ is a constant related with the interface energy density γ. The exp term and the T^{-1} dependence are related with the mobility M of the grain boundary. $\Delta G^a$is the activation energy for atomic migration between grains, k is the boltzmann’s constant, T is the absolute temperature. To determine the activation energy for the atomic diffusion across the grain boundary during the grain growth, Kissinger equation act as a requisite tool [10]

$$\frac{E\Phi}{RT_m^2} = An(1-x)_m^{n-1} e^{-E/RT_m} \qquad (4.10)$$

where E is the activation energy, R is the gas constant, T_m is the peak temperature, Φ is the constant heating rate of temperature rise, x is the fraction reacted, A is a constant, n is the empirical order of reaction. There exists another type of grain growth in which the grains grow abnormally, film’s grain are many fold larger than the thickness value. This rapid and abrupt grain growth can only be explained in terms of a significant increase of grain boundary mobility. The grain boundary velocity behavior can be expressed as [8]

$$\upsilon = \left(\frac{C\Delta G}{TV_m}\right) \exp\left(-\frac{\Delta G^a}{RT}\right) \qquad (4.11)$$

where C is a constant, R is the gas constant, T is the annealing temperature, ΔG is the difference in free energy between neighbor grains, $\Delta G^a$is the activation energy for atomic migration between grains and V_m is the molar volume.

Systematical investigations have already emphasized the preferred candidature of sono-electrodeposition for thin film synthesis, but the ex-situ grain growth characteristics of deposited films are yet to be established for future generation circuit applications. In this section an attempt has been made to study the growth behavior of sono-electrochemically deposited copper thin films, as sonication has a definite impact on the film’s physical properties. The growth thermodynamics and kinetics have been correlated with the structural studies to establish and propose the guiding mechanisms involved in the growth process.

4.3.2. Experimental details

The growth analysis was done for the post-synthesized films. For initial experimentation the growth study was done for a film deposited at − 400 mV and 25 °C from a bath of 10 g l^{-1} Cu(II) concentration in order to get a continuous film. Then for effect of deposition temperatures on the growth kinetics, copper films have been electrochemically deposited onto graphite substrates on an exposed surface area of 0.25 cm^2 at different electrolyte temperatures (25, 20, 15, 10 and 5 °C).

The films were deposited on as received fresh substrates without any further treatment. Analytical grade $CuSO_4.5H_2O$ (6.35 g l^{-1}) and H_2SO_4 (40 g l^{-1}) were used for the preparation of electrolytes for copper deposition. The solution is prepared with doubly distilled water. The Electrochemical experiments were performed with a potentiostat/galvanostat (Eco Chemic Netherland, Autolab PGSTAT 12) system having computer interface of GPES software. A standard three- electrode cell was assembled with a counter electrode of Pt rod (3.5 cm^2, Eco chemie) and an Ag/AgCl reference electrode. The non-isothermal growth analysis was carried out using DSC (Mettler Toledo-DSC822). Experiments were performed at a temperature range of 25 – 400 °C at a temperature ramp of 5 °/min. For the calculation of activation energies, scanning rates of 10°/min, 20 °/min were used. Morphological studies of prepared samples were performed by means of SEM (JEOL 6480LV) and AFM (Veeco diInnova). The phase analysis was done with XRD (Philips X-pert MPD), and the patterns were recorded from 40-100° at a scanning rate of 2°/Min with CuKα radiation. The surface energy analysis was done by contact angle instrument (OCA-20 Data Physics).

4.3.3. Results and Discussions

Fig. 4.26 shows the net non-reversing heat flow of 790 nm thick sono-electrodeposited Cu film along with its silent counterpart.

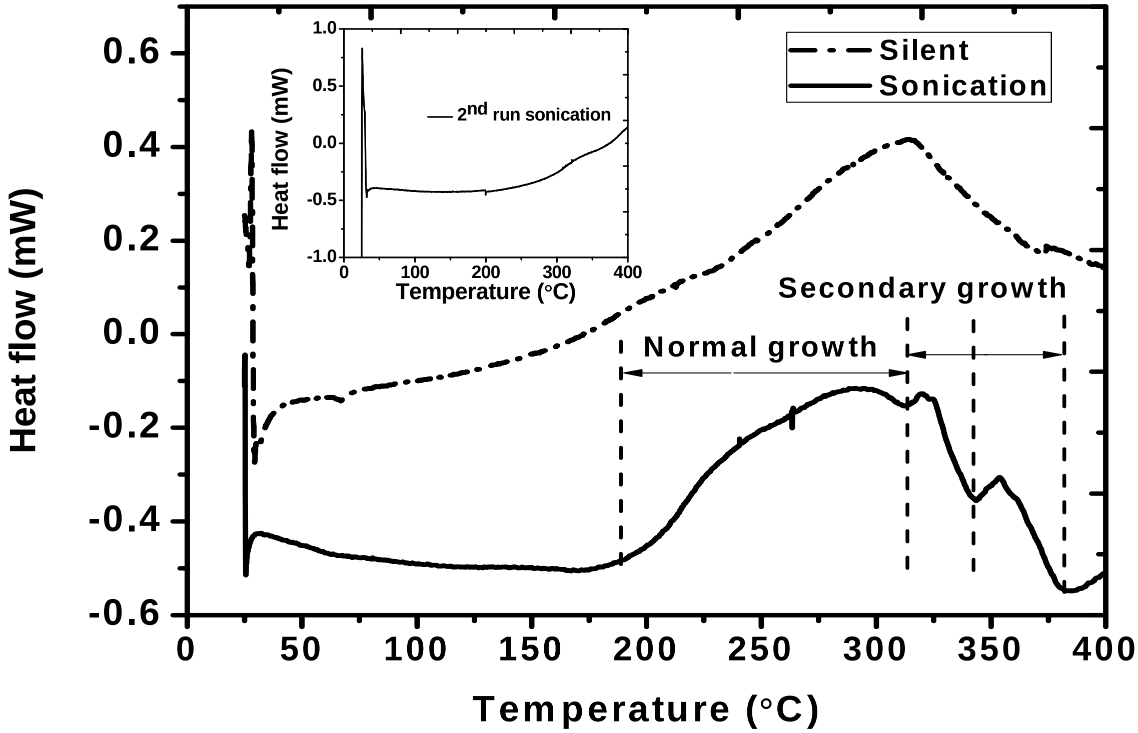

Fig. 4.26. DSC thermographs of the heating cycles at 2 °C/min for silent and sonicated films deposited on graphite

The silent deposit had a quite normal growth behavior and did not form continuous film even at the experimented high deposition potential and concentration as shown in 4.28. Hence further analysis deals with the sonicated films only. It can be observed that two low energy exothermic reactions set in at 310 °C and 360 °C, preceded by the main heat release peak at 275 °C for the sonicated depositions. Such multi regional but pre-shoulder heat release peaks and a main peak have been observed for several other electrodeposited nanocrystalline materials unlike our post-shoulder peaks [11,12]. Further the grain growth kinetics can be estimated from the knowledge of the activation energy. The effective activation energy for the initiation of grain growth can be determined from equation (4.10). A straight line is obtained by plotting $ln(\frac{\Phi}{T_m^2})$ versus ($1/T_m$) as indicated in fig. 4.27.

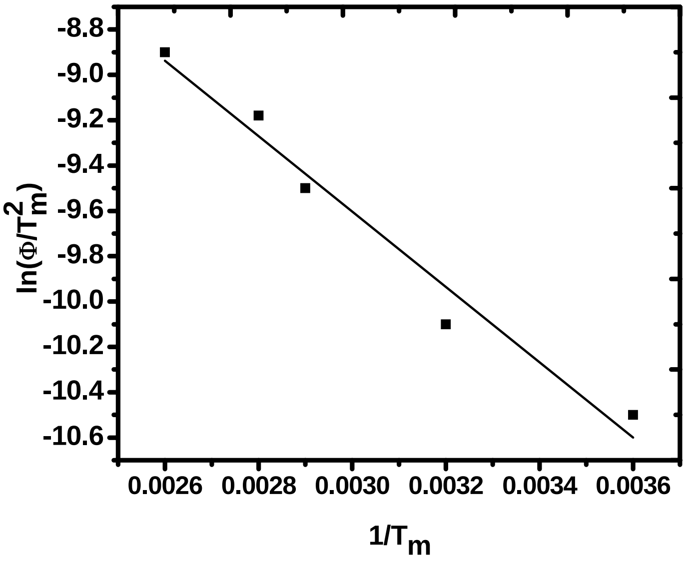

Fig. 4.27. Kissinger plot for the calculation of activation energy for atomic diffusion

Thus the activation energy for the grain growth and hence the underlying primary growth mechanism can be derived from the slope of the graph. In this work five heating rates (2, 5, 10, 15 and 20 °C) were used. The activation energy derived from this data is 1.02 eV/atom, which is close to the reported activation energy for grain boundary-self diffusion [13,14]. To relate distinct parts of DSC-curve to the microstrutural development of the materials upon heating, ex situ SEM and AFM analysis have been performed. The analysis were carried out at temperatures at which exothermic peaks were observed in DSC-curve, i.e. at 275 °C (peak) and 360 °C temperatures (post-shoulder). The original morphology of the particles in the as-deposited film (fig. 4.28c) is approximately spherical with grain sizes of 1 μm. In fig. 4.28d the shape preserved but grown and blurred grain boundaries can be observed. Longer thermal treatment (360 °C), results in the formation of a bimodal microstructure (fig. 4.28e) with a few nanocrystalline grains in the grown matrix.

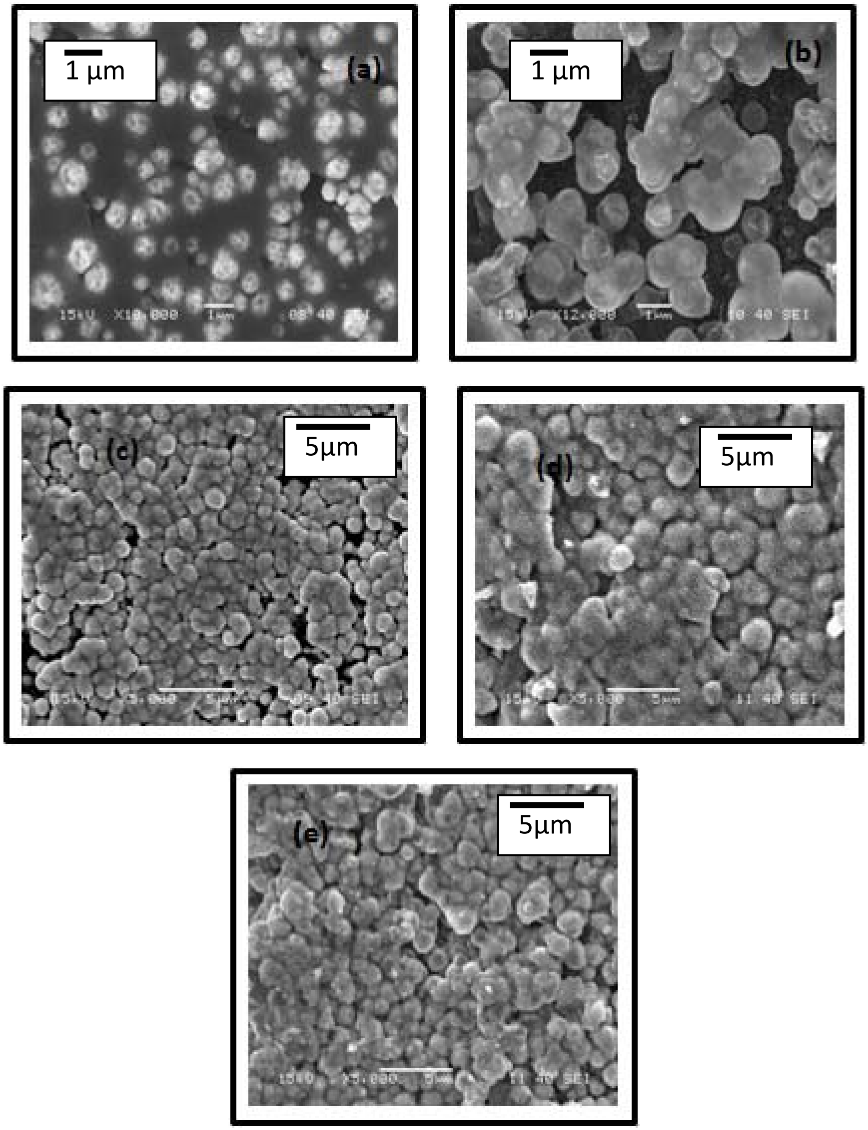

Fig. 4.28. SEM micrographs of Cu films (on graphite) in silent (a) as-deposited and (b) treated upto 360 °C and sonication (c) as-deposited, (d) treated upto 275 °C and (e) 360 °C temperatures

It can further be noticed that large grains already present have not noticeable grain growth, while the new fine grains have grown from the matrix. This implies that the microstructure of large grains, once formed, is relatively stable. To elucidate the uncommon grain contrast after thermal transients, a 25 degree rotational SEM is done for samples before and after DSC (360 °C) treatment (figs. 4.29a & b). Uniform distribution of spherical copper clusters (fig. 4.29a) before thermal treatment are easily distinguishable from the dual structural architect of Cu phases of the post-shoulder DSC thermal transient in fig. 4.29b.

It can also be observed form fig. 4.29b and c that the grains of the electroplated Cu film have grown to an average grain size of about 2 μm. The energy stored in the grain boundaries can be calculated by using the equation, $E = 3\gamma/2R$, where $\gamma = 0.625$ J m^{-2} is the high angle grain boundary energy and R is the average grain radius. The stored energy in the grain boundaries of the as-deposited self annealed Cu film is about 7.13 J mol^{-1}. After DSC measurement the energy stored in the grain boundaries is about 2.6 J mol^{-1}. The change of grain boundary energy is about 4.56 J mol^{-1}, which is similar to the energy release in the main exothermic peak (4.67 J mol^{-1}) area in the first heating cycle of the DSC curves. It is reasonable to conclude that the exothermic peak corresponds to the energy released during the grain growth by grain boundary motion. The energy released during the post peaks are 0.001 and 0.037 J mol^{-1}.

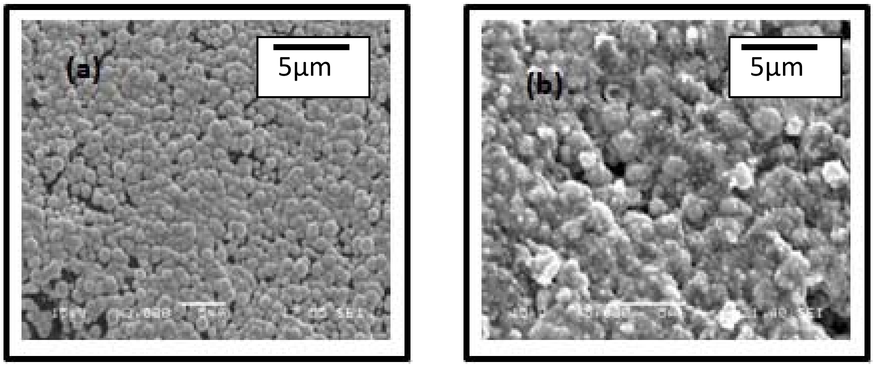

Fig. 4.29. SEM micrographs of sono-electrodeposited Cu films (on graphite) at rotation of 25° degree of (a) before and (b) after DSC scan upto 360 °C temperature

To augment the DSC and SEM data already discussed concerning growth behavior of the film, AFM images (figs. 4.30a-c) have been recorded to provide topographic textural evidence for the treated as well as untreated surfaces. Uniform grain distribution with distinct grain boundaries is observed for untreated samples. After thermal treatment of the film to the temperature of 275 °C, the indistinct grain boundaries of bigger sizes (fig. 4.30b) can be observed. While the film treated upto the temperature of 360 °C has a uniform surface topography with small grains on the surface of the deposit. The surface roughness (R_a) of the films decreased to 140 nm (at 275 °C) from 212 nm (untreated) and then increased to 262 nm (at 275 °C). To ascribe the possible growth mode for these sono-electrochemically deposited films, surface energy analysis was done. Surface energy of the film was found to be increased from a value of 40.73 mN/m to 55.56 mN/m after the DSC run upto 360 °C. The grain growth may be attributed to abnormal growth category as observed for nanocrystalline materials [4,11]. Abnormal grain growth is mostly surface energy driven mechanism [15], and hence a net alteration in the surface energy is expected. Further the film did show a tendency for grain growth in the second DSC run as shown in fig. 4.26 (inset). This could promote a second phase of abnormal grain growth of the copper grains, favorable after the completion of the stable and normal grain growth. The above unusual observations can be explained in the following lines.

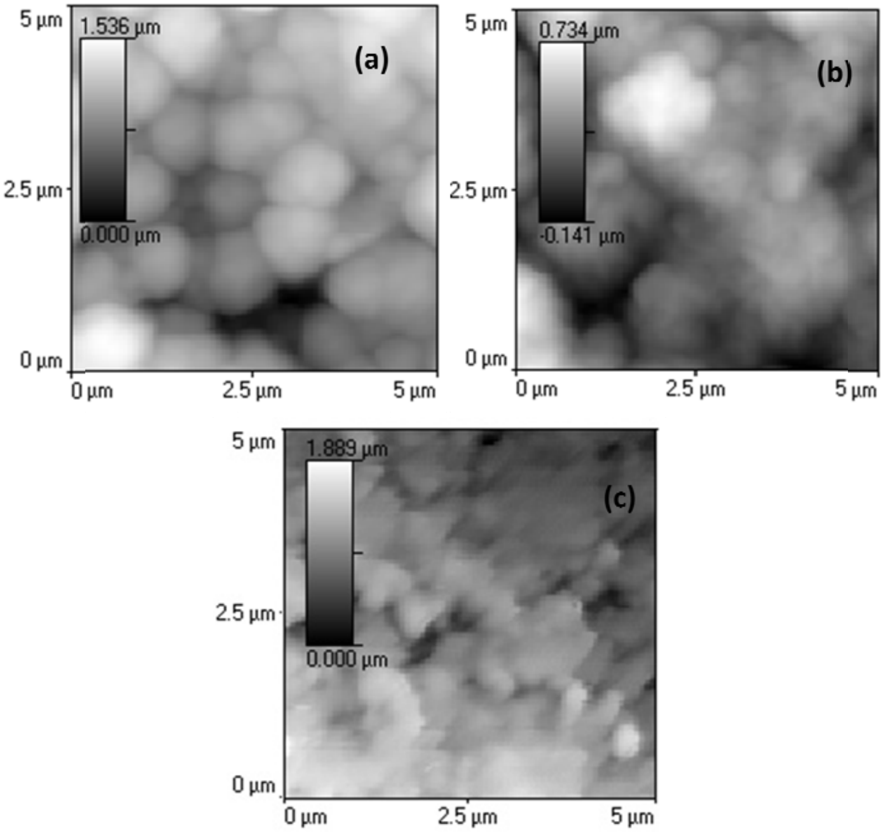

Fig. 4.30. AFM micrographs of films (on graphite) (a) before and after DSC scan upto (b) 275 °C and (c) 360 °C temperature

The concept of secondary nucleation on the existing primary nuclei matrix due to particle fragmentation in presence of ultrasound has been proposed (Chapter 4.2.1). As the secondary nano-grains are finer, they should have grown preferably both during self annealing as well as temperature treatment periods. But the constrictions imposed by the primary grain matrix dimension might have not endured the high energy grain boundaries to move for energy reduction and hence stabilization. Hence, the main exothermic peak would have lead to the grain boundary diffusion driven normal grain growth. Then the clustering of the secondary grains would have been unobjectionable after the primary matrix relaxation following the temperature transient. This further solves the assertion related with the increase in surface energy past the normal grain growth.

4.3.3.1. Thermal analysis

With the above observations, investigation is now focused on the effect of deposition temperature. Fig. 4.31 shows the thermograph of electrodeposited samples at scanning rate of 5°/min from 25°C- 400°C.

The entire DSC traces exhibit either one or two exothermic heat release peaks at around temperature of 300 °C. The exothermic peak signifies the occurrence of grain growth where due to the average increase of the grain size decreases the grain boundary area or the grain boundary energy. The associated heat release is higher for the film deposited at 5 °C as compared to the films deposited at high temperatures. Also the peak temperature has shifted to higher values. This may be due to the fact that majority of the grains are small sized, so require higher temperature to attain equilibrium for their growth and simultaneously will release more heat than the coarse grained deposits. Along with exothermic peaks some unsystematic endothermic peaks have also been observed for 10 °C, 15 °C and 25 °C at various heating rates. The energy consumed for these depressions in the DSC scan can possibly be due to the reaction of nitrogen (the reacting atmosphere in the DSC furnace) with the carbon substrate resulting in an amorphous product during DSC experimentation [16]. The presence of nitrogen in the samples after DSC run was confirmed from the EDS elemental analysis as shown in fig. 4.32.

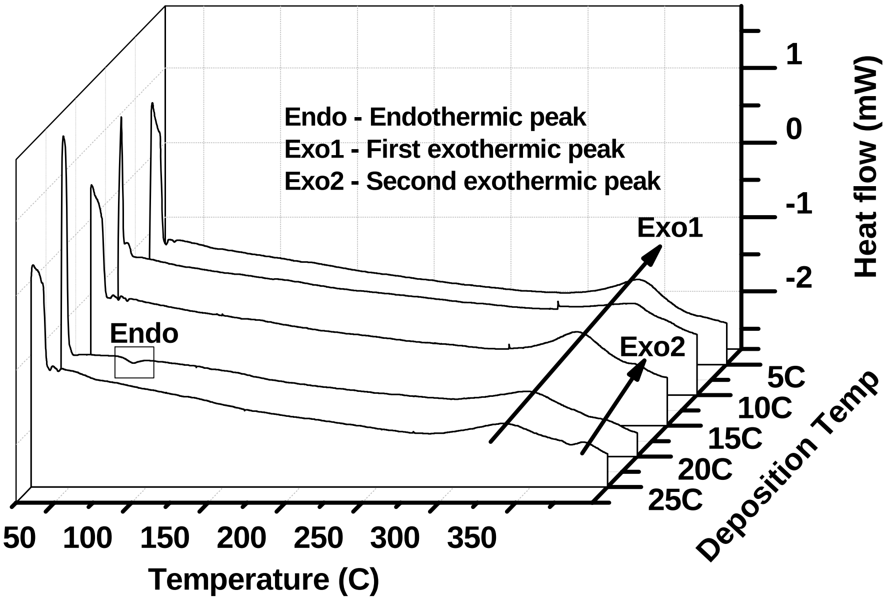

Fig. 4.31. DSC scans of copper deposited (on graphite) at different temperature at scan rate of 5°/min from 25 °C – 400 °C

Activation energy for the grain growth process was determined by heating the films at different heating rates. The DSC thermographs are shown in fig. 4.33a for the temperature of 25 °C. As illustrated in fig. 4.33a, the exothermic peaks of crystallization shift to higher temperature gradually with increasing heating rate. This observation reveals that the growth behavior is kinetic in nature. At low heating rates, the systematic orientation controlled growth will ease the early attainment of equilibrium. While at high heating rates the random grain growth will be far from equilibrium because of lack of any order. So the peak temperature for the high heating rates is generally greater than for low heating rates.

The calculated effective activation energies for grain growth (from eq. 4.10) is given in fig. 4.33b. The values signify a grain boundary self diffusion growth mechanism as observed earlier.

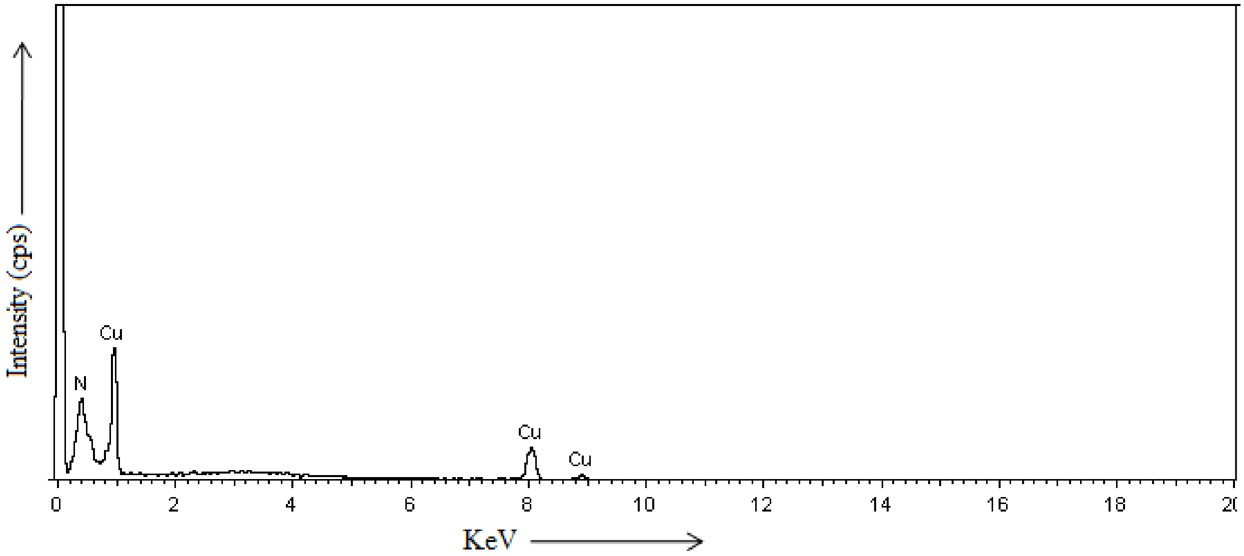

Fig. 4.32. EDS plot of Cu film (on graphite) after thermal treatment

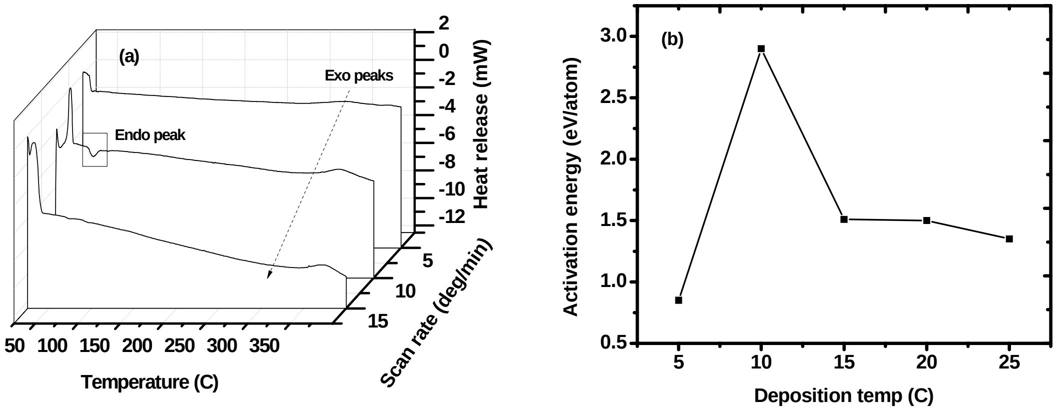

Fig. 4.33. (a) DSC scans at heating rate of 5°/min, 10°/min, 20°/min of Cu electrodeposited(on graphite) at 25 °C and (b) calculated activation energies for different deposition temperatures

However the variation in the energy values is not uniform. This variation of the activation energy might be attributed to the grain size and orientation even though it is not known how they can induce such fluctuations. Each thermal analysis was scanned at least twice to ensure authenticity. No definitive answer can be found at this point.

To elucidate the growth mode for the grain boundary driven self diffusion growth, a set of surface energy analysis was done before and after DSC treatment and are given in fig. 4.34. Surface energy of the post treated films was found to be increased for temperatures 25, 20 and 15 °C whereas for the other temperatures there is a decrease of the values. The above discrepancy may be attributed to a transition from abnormal grain growth to normal growth with reduction of temperature, which can be correlated with the multi peak observations in the DSC scan for the above temperatures. These growth kinetic observations are then correlated with structural evolution to envisage and explain the issues further.

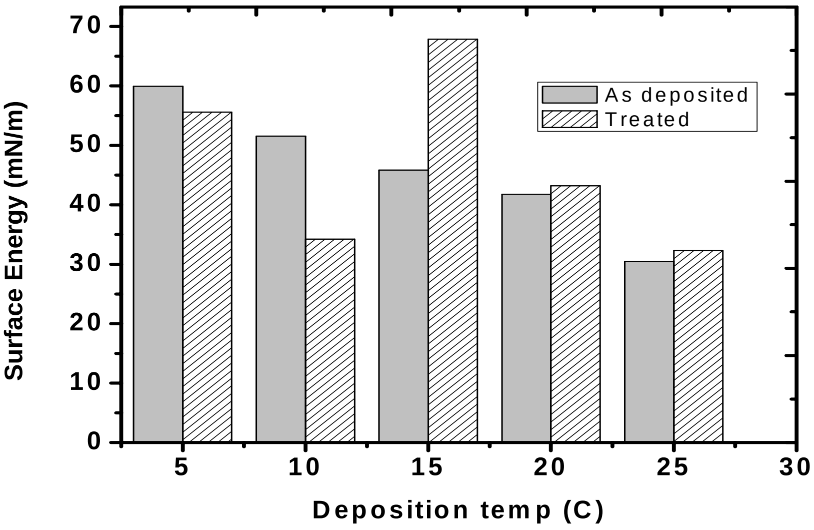

Fig. 4.34. Variation of surface energy for Cu films (on graphite) in as-deposited and treated conditions deposited at different bath temperatures

4.3.3.2. XRD analysis

The XRD patterns of the as-deposited and after DSC scan of copper films have been illustrated in fig. 4.35 and fig. 4.36. The sharp peaks show the crystallinity of the copper deposits. The diffraction peaks at 2θ = 43.27, 50.34 74.132 and 89.934 can be indexed as the (111), (200), (220) and (311) planes of copper with cubic symmetry respectively [17]. The intensity of peaks decreases with decrease in bath temperature as shown in fig. 4.35. This attributes to the formation of smaller sized grains at lower bath temperature compared to the higher one. Although after thermal treatment the spectrum is quite noisy, peaks corresponding to copper lattice systems can be observed. The intensity of the peaks corresponding to copper has been reduced and has broadened too. An interesting finding can be observed here that the peaks have shifted towards left of 2θ (from 43.27° to 43.436° for Cu(111)) values to that of observed values in case of as-deposited copper.

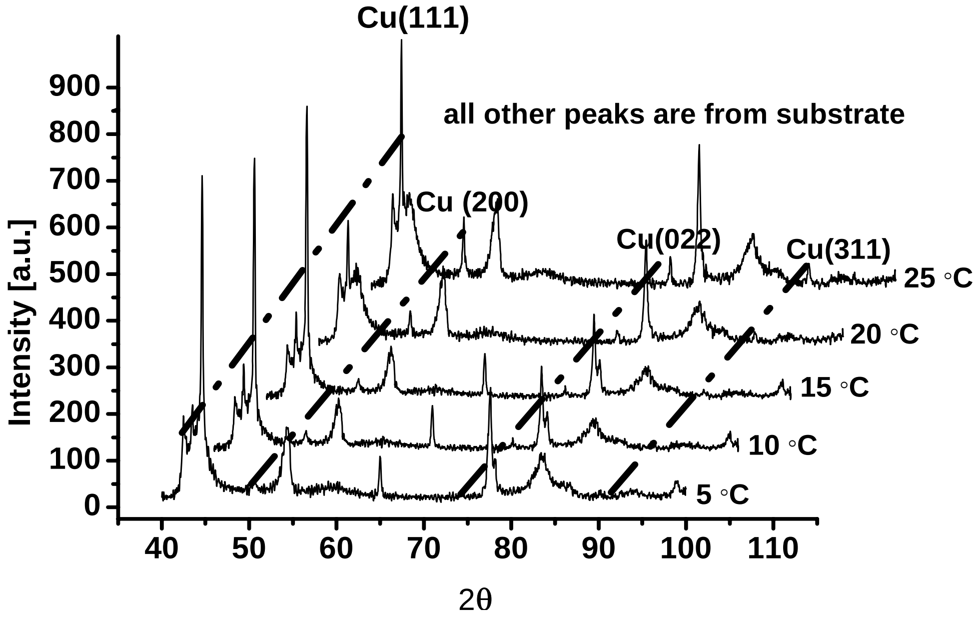

Fig. 4.35. XRD patterns of copper deposits (on graphite) under sonication condition

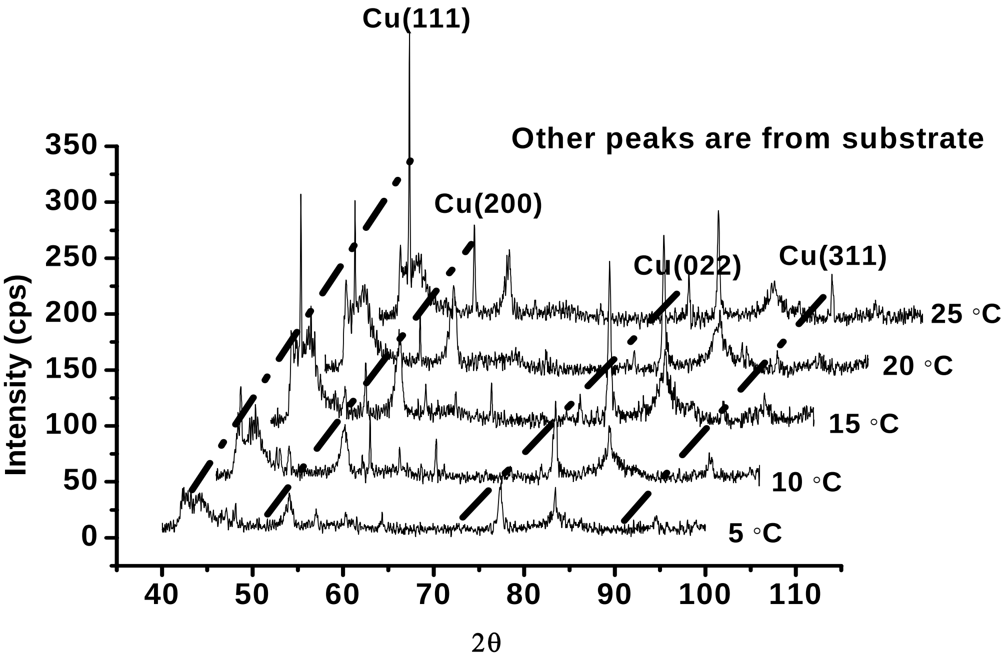

Fig. 4.36. XRD patterns of sono-electrochemically deposited copper films (on graphite) after DSC scan

The reduction in intensity and broadening of the peaks may not be contributed by the particle size reduction. However, the reason for the inverted growth is not clear, but this may be the consequence of the strain developed due to the growth of the grain. The crystallite size and lattice strain calculated from the XRD plots by using the Williamson- Hall formula is presented in fig. 4.37. The analysis of the XRD pattern reveals that the crystallite size decreases (from 160 nm to 20 nm) and the associated strain increases as the synthesis temperature of the films was lowered. After thermal treatment all the grain size was observed to be increased and the lattice strain has got decreased.

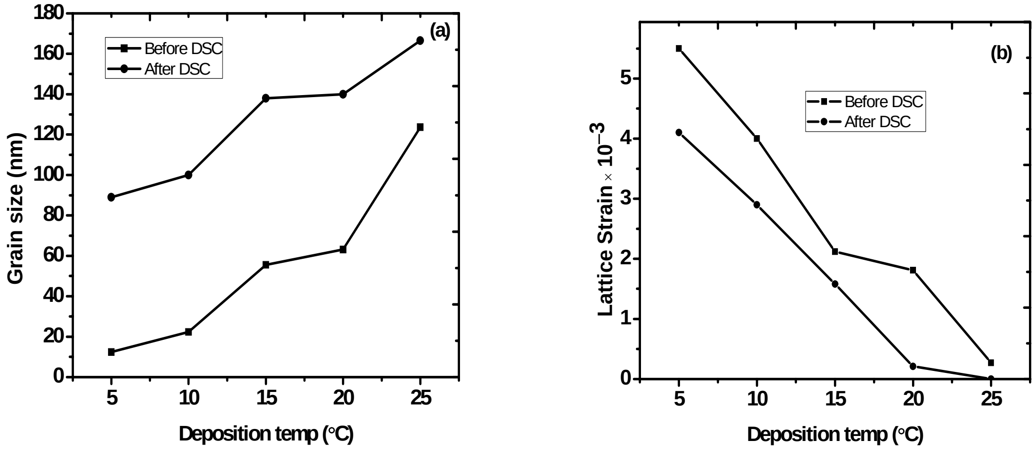

Fig. 4. 37. Variation of (a) crystallite size and (b) lattice strain with deposition temperature for treated and untreated conditions

4.3.3.3. Morphological analysis:

Fig. 4.38 shows the SEM topographies of copper films before and after thermal treatment for the deposits prepared under sonication at – 300 mV for different bath temperatures. The deposited copper nuclei bear the spherical shape with varying grain distribution (figs. 4.38a-c). The size of the grains decreases with decreasing bath temperature. Now concentrating on the SEM micrographs (figs. 4.38d-f), of the samples heated upto 400 °C at a temperature ramp of 5°/min, it can be seen that after the thermal treatment, grains are bigger than their untreated counterparts with blurred grain boundaries. The distinct features of the surfaces of the treated films prepared at 25 and 15 °C are a bimodal grain distribution, small grains of 100 to 200 nm are observed on the very large grains. Whereas the low temperature film, at 5 °C after DSC treatments have nearly uniform grain distributions on the surfaces. To enumerate the above observations, a detail study was then done by AFM (figs. 4.39a-d) for temperatures of 25 °C and 5 °C with two magnifications after thermal treatment. The surface of 25 °C film at 20 μm^2 scan area is seen to have higher elevation (max. 5.317 µm) than the 5 °C deposit (max. 4.856 µm).

The corresponding images (figs. 4.39b&d) at high magnifications show dispersed nano-grains on the micro-grained matrix at 25 °C while uniform big grains can be observed in the treated film deposited at 5 °C. Hence smoother topography at 5 °C temperature was observed. The roughness values of the treated surfaces vary from 771 to 128 nm. The possible reasons can be conjectured at this point: the abnormal growth of fine grained smooth layer has not happened for films deposited at low temperature because of nominal size variations in the primary and secondary grains in as-deposited film.

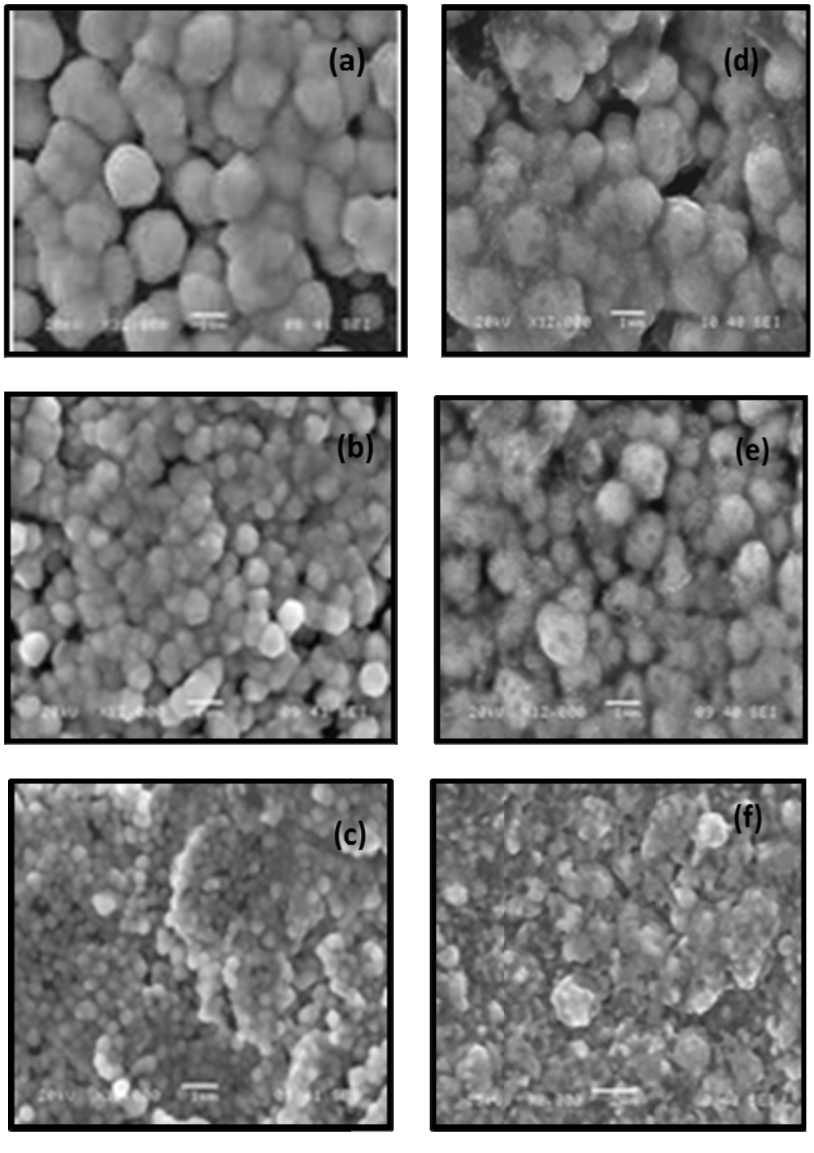

Fig. 4.38. SEM images of as-deposited copper (on graphite) at (a) 25°C, (b) 15°C and (c) 5 °C temperatures and their corresponding micrographs (d) – (f) after DSC at heating rate of 5 °C /min

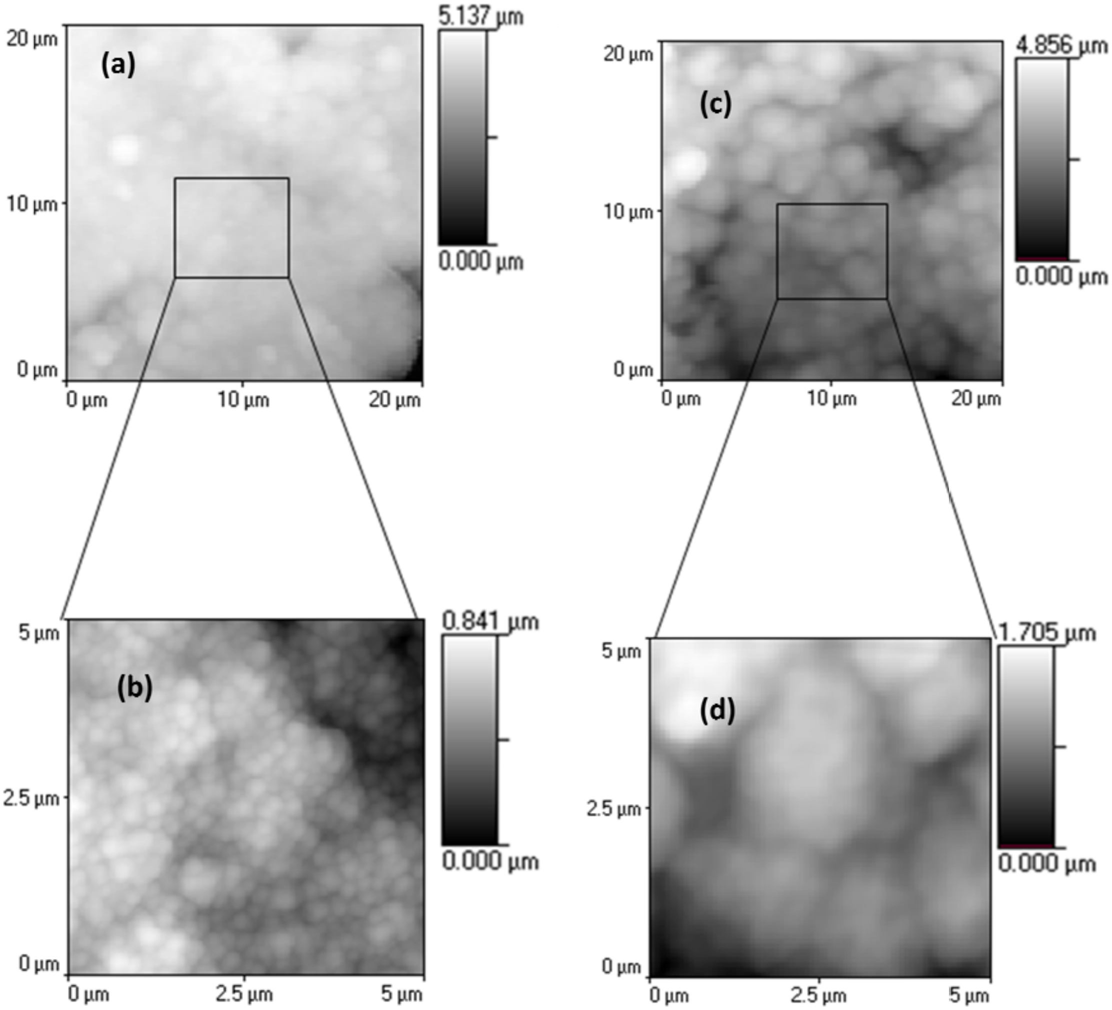

Fig. 4.39. AFM micrographs of Cu deposits (on graphite) of (a,c) 25 °C and (b,d) 5 °C temperatures after DSC scan

4.3.4. Summary

Thin films of Cu were prepared by sono-electrodeposition at low bath temperatures. The effect of bath temperatures and sonication on the non-isothermal post deposition growth behavior was investigated by examining the growth kinetics and condition of the surface microstructure by DSC and SEM and AFM. DSC thermograms were found to have multi peaks for high temperature films. An exclusive study for the high temperature deposit was done to enumerate the growth behavior. A bimodal grain distribution and increase in surface energy was found for the post temperature transient film from an untreated film with uniform spherical copper topography. This did lead us to introduce a second phase of abnormal grain growth of the copper grains, favorable after the completion of the stable and normal grain growth for the high temperature films. Further the applications of Kissinger method at several heating rates allowed to estimate the activation energy for growth, and was found to be controlled by grain boundary self diffusion for all the film crystallization temperatures. Results obtained for XRD and surface energy estimations of the films for both the conditions of as-deposited and post thermal treatment, have unusual variations. Comparisons between the DSC, surface morphology and texture analysis by SEM and AFM may suggest a transition of abnormal growth to normal mode of growth behavior as the film synthesis temperatures were reduced.

4.4.5. References

1. J. M. E. Harper, C. Jr. Cabral, P. C. Andricacos, L. Gignac, I. C. Noyan, K. P. Rodbell, C. K. Hu. J. Appl. Phys., 86 (1999) 2516.
2. E. M. Zielinski, R. P. Vinci, J. C. Bravman, Mater. Res. Soc. Symp. Proc., 391 (1995) 103.
3. C. Detavernier, S. Rossnagel, C. Noyan, S. Guha, C. Jr. Cabral, J. Lavoie, J. Appl. Phys., 94 (2003) 2874.
4. S. C. Chang, J. M. Shi, B. T. Dai, M. S. Feng, Y. H. Li, J. Electrochem. Soc., 149 (2002) G535.
5. K. B. Yin, Y.D. Xia, C. Y. Chan, W. Q. Zhang, Scr. Mater., 58 (2008) 65.
6. W. Dong, J. Zhang, J. Zheng, J. Sheng. Mater. Lett., 62 (2008) 1589.
7. C. V. Thompson, R. Carel, J. Mech. Phys. Solids., 44 (1996) 657.
8. F. P. Luce, P. F. P. Fichtner, L. F. Schelp, F. C. Zawislak, Mater. Res. Soc. Symp. Proc., 1150 (2009) RR06.
9. P. R. Rios. Scr. Mater., 40 (1999) 665.
10. H. E. Kissinger, Anal. Chem., 29 (1957) 1702.
11. P. Choi, M. da Silva, U. Klement, T. Al-Kassab, R. Kirchheim, Acta. Mater., 53 (2005) 4473.
12. G. Hibbard, K. T. Aust, G. Palumbo, U. Erb, Scr. Mater., 44 (2001) 513.
13. S. K. Donthu, M. M. Vora, S. K. Lahiri, C. V. Thompson, S. Yi, J. Electron. Mater., 32 (2003) 531.
14. K. B. Yin, Y. D. Xia, C. Y. Chan, W. Q. Zhang, Q. J. Wang, X. N. Zhao, et. al. Scr. Mater., 68 (2008) 65.
15. V. M. Dubin, G. Morales, C. Ryu, S. S. Wong, Mater. Res. Soc. Symp. Proc., 505 (1998) 137.
16. **http://www.osti.gov/bridge/purl.cover.jsp;jsessionid=F1E21227A31853547660AB83A5C635E3?purl=/591090-PoUOmr/webviewable/**
17. International Centre for Diffraction Data (ICDD), Card No. 04-0863.

4.4. Evaluation and assessment of residual stress and nano-mechanical properties

The purpose of the present study is to gain a basic understanding, through investigation, of internal stresses in copper films deposited on graphite substrate. Knowledge of internal stresses in thin copper film structures is essential in understanding the film properties, such as stress migration, adhesion, hardness and elasticity.

4.4.1. Introduction

Films or coatings on a substrate are usually in a stressed state, addressed as residual stress. The film wants to be smaller or larger than the substrate allows it to be, hence the film is in tensile stress (film wants to shrink) or compressive stress (film wants to expand). Residual stresses are basically caused by interface coherency, thermal cycling, and/or change in deposition parameters and applications of films [1-4]. These stresses play a significant role in the mechanical performance and reliability of thin films. Large tensile and compressive stresses may lead to cracking and buckling of the film respectively [5-8]. A high resistance to mechanical damages/ control of residual stresses is thus strongly demanded, and it is essentially important to clarify the mechanical properties of thin films before practical applications. Therefore, to measure the residual stresses and its effects on thin-film mechanical properties is especially important. And the conventional wisdom is to strive for a compressive stress of a few hundred MPa, as it will make the film adhered to the substrate.

Application of ultrasound during electrodeposition is believed to affect the film synthesis in terms of good adhesion, deposition uniformity, compactness and brightness [9-11]. However, the impact of the parameter on the residual stress and mechanical properties of the films has rarely been studied. Hence this study addresses the important issue of residual stresses by using the well established techniques. Most importantly, this study clarifies the variation of residual stress and mechanical properties with variation of film morphology by alterations in the deposition temperature. We have knowledge of stress in thin films in two ways: (1) by directly measuring the crystal lattice strain in the film using X-ray diffraction [12,13] and (2) by measuring the elastic deformation of the substrate [13,14]. The second method has been used in this investigation to study the state and intensity of residual stress.

4.4.2. Experimental details

Graphite substrates (Asbury, USA) of 0.25 cm^2 surface area were used to electrodeposit the copper films. All the experiments were carried out onto fresh graphite electrodes. The bath composition was $CuSO_4.5H_2O$ (6.35 g l^{-1}) and H_2SO_4 (40 g l^{-1}). Chemicals were procured from Merck Chemical Co. and used without further purification.

This section is written based on the unpublished work

A. Mallik, B. C. Ray, Residual stress and nano-mechanical properties of sono-electrodeposited Cu films, **Surface Engineering (Accepted)**.

A three electrode open cell with an Ag/AgCl reference electrode (Eco Chemie, Netherlands) and a platinum counter electrode (surface area of 3.14 cm^2) were used for the deposition. The depositions were carried out at temperatures of 25 °C, 20 °C, 15 °C, 10 °C and 5 °C. A high-density ultrasonic probe (Sonics & Materials, VCF1500) equipped with titanium oscillator (horn) 12.5 mm in diameter, operating at 20 kHz with a 20% output was used for ultrasonic irradiation. The intrinsic stress of copper supporters was measured using a surface profilometer (Veeco Dektak 150) equipped with stress analysis software, which calculated the stress based on the substrate's radius of curvature before and after copper electrodeposition. The mechanical properties of Cu films were measured by a UMIS nanoindenter with a Berkovich diamond indenter (tip radius ~100 nm). During each test, the load was applied to a maximum value of 10 mN. The surface adhesion study was done in AFM by analyzing the force-displacement curve in contact mode. The tip details are, P(n) doped Silicon Nitride with a spring constant of 0.9 N/m.

4.4.3. Results and discussion

4.4.3.1. Residual stress

The XRD pattern of the films deposited at various temperatures are shown in fig. 4.40. The sharp peaks show the crystallinity of the copper deposits. The diffraction peaks at 2θ = 43.27, 50.34 74.132 and 89.934 can be indexed as the (111), (200), (220) and (311) planes of copper with cubic symmetry respectively [15]. The intensity of peaks decreases with decrease in bath temperature. This attributes to the formation of smaller sized grains at lower bath temperature compared to the higher one. The measured residual stresses in as-deposited copper films as a function of deposition temperature and calculated grain size (by XRD) are shown in fig. 4.41a.

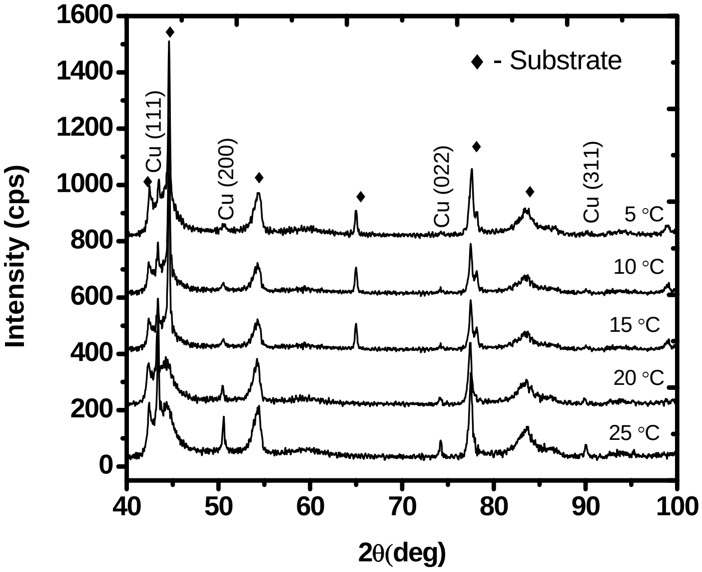

Fig. 4.40. XRD pattern of sono-electrodeposited Cu thin films (on graphite) at different temperatures

Film thickness was varying in between 750 nm to 3 µm for deposition temperatures 5 °C to 25 °C respectively. Residual stress in the copper films was always compressive regardless of film deposition temperature. The nature of the stress may vary with materials systems, deposition methods, thickness of deposit and deposition temperature. It has been reported by other researchers that they can possess different internal stresses of various magnitude, when the copper films were produced by different methods. Okolo and Yu *et. al.* have showed compressive stresses in Cu films [16,17]. While Takao et. al. [18] and Sunjung et. al [19] have observed tensile residual stresses in sputtered and electrodeposited Cu films respectively. All these variations were explained on the fact that coalescence of individual islands leads to tensile stress and compressive stress was due to relief of these coalescence stress in the due process of film formation. Other parameters e.g. volumetric distortion, thermal stress and presence of impurity atoms have also been mentioned as reasons for these stress variations.

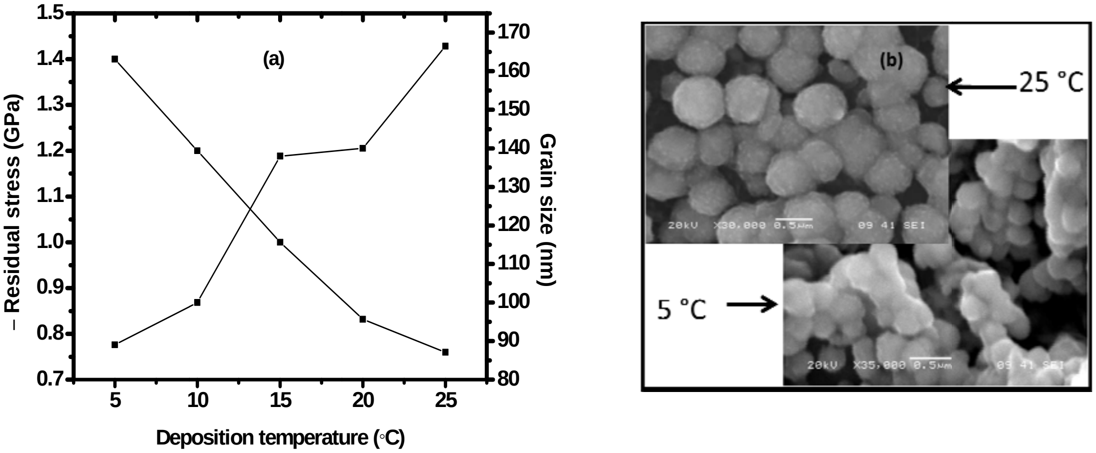

Fig. 4.41(a) – Residual stress of Cu thin films (on graphite) at various deposition temperatures and (b) SEM micrographs of deposits at 25 °C and 5 °C temperatures

In view of these many parameter affected alterations in the stress, our explanation is given in the following lines. The film growth process can be divided into three stages: (i) island growth before coalescence, (ii) island coalescence, and (iii) film growth after coalescence. The general trend of stress development during the three phases follows an early compressive stress during the first stage of metallic film growth, prior to the film becoming continuous. A physical picture for the generation of a compressive intrinsic stress during island growth can be based on the following two effects [20,21]. First, surface stresses acting on an unconstrained island induce an equilibrium lattice spacing different from that of the bulk that scales inversely with the island size. Second, there is a critical size at which an island effectively becomes firmly attached the substrate. As a result of this second effect, an island larger than the critical size is no longer able to change its in-plane lattice spacing during further growth.

Since the equilibrium lattice spacing will change as the island increases in size, the substrate must impose traction on the island to keep it from attaining its equilibrium spacing. If a post-critical island has a smaller in-plane lattice spacing relative to the bulk, corresponding to a net positive surface stress (typical of most low index metallic and alkali halide free surfaces), this traction will result in a compressive intrinsic stress. This compressive stress can become very large in magnitude. As the growing crystallites contacted each other at their bases, the side-walls zipped together and the tradeoff between surface and grain boundary energies can drive crystallite coalescence and generate tensile stresses [22-24]. The corresponding microstructures of the deposits at the early stage of deposition are shown in fig. 4.41b. The extent of coalescence of the grains at the highest and lowest temperature of deposition in the present investigation can clearly be observed from the figures. Hence a net tensile stress should be expected instead of the observed compressive stress. This may be due the fact that, if the metal being deposited has high adatom mobility, the post-coalescence intrinsic stress may decrease with further film growth. In many cases, particularly face-centered-cubic (fcc) metals with lower melting temperatures, the stress eventually becomes compressive. Another factor may contribute to the evolution of compressive stress is surface stress. In addition to a change in surface energy, island coalescence will lead to a change in surface stress equal to $h_{\mathrm{gb}}/2 - h$, where h is the surface stress of the free surface and h_{gb} is the interface stress associated with the grain boundary. This change in surface stress will lead to an instantaneous change in the intrinsic stress of [20]

$$\Delta\sigma_{d,imp} = \beta\,(h_{gb} - h)/d_{imp} \quad (4.12)$$

As can be observed from the equation, the stress can only be negative (compressive) if the free surface stress is higher than the grain boundary stress. And the magnitude of this stress will in part, be determined by how strongly attached the island to the substrate [20,21]. Ultrasound increases both the parameters i.e. adatom mobility [25] and the attachment of the islands with the substrate [9,10]. The level of the compressive stress will be further high with decreasing grain size as can be depicted from the equation.

4.4.3.2. Hardness and elasticity

Fig. 4.42a shows the load-penetration depth curves of nanoindentation tests of Cu films deposited at different bath temperatures. The maximum load used was 10 mN. No evidence of substrate effects in forms of either kick-back or elbows in the unloading curves can be observed. It was found that the mechanical properties varied with temperature of deposition. The deposition at 5 °C is the hardest as the depth of penetration of the indenter is less. By the Oliver–Pharr relation [26], the hardness and elastic modulus of the Cu films were obtained as plotted in fig. 4.42b. The hardness values observed are in the range from 0.78 – 1.86 GPa. Copper films at temperatures below 15 ºC have hardness above the hardness values for pure crystalline copper (1-1.5 GPa) [27]. This can be attributed both to grain size strengthening (small grains compared to the grain size of pure crystalline copper) and/or strain hardening. The grain size strengthening is determined by the strength of Cu grains (H_0) and the average grain size (d) of Cu according to the Hall-Petch relation ($H = H_o + kd^{-1/2}$), where k, Hall-Petch coefficient accounting the grain boundary resistance to dislocation movement. Thus, the increased dislocation piled up with decreasing size has resulted such high strength in films.

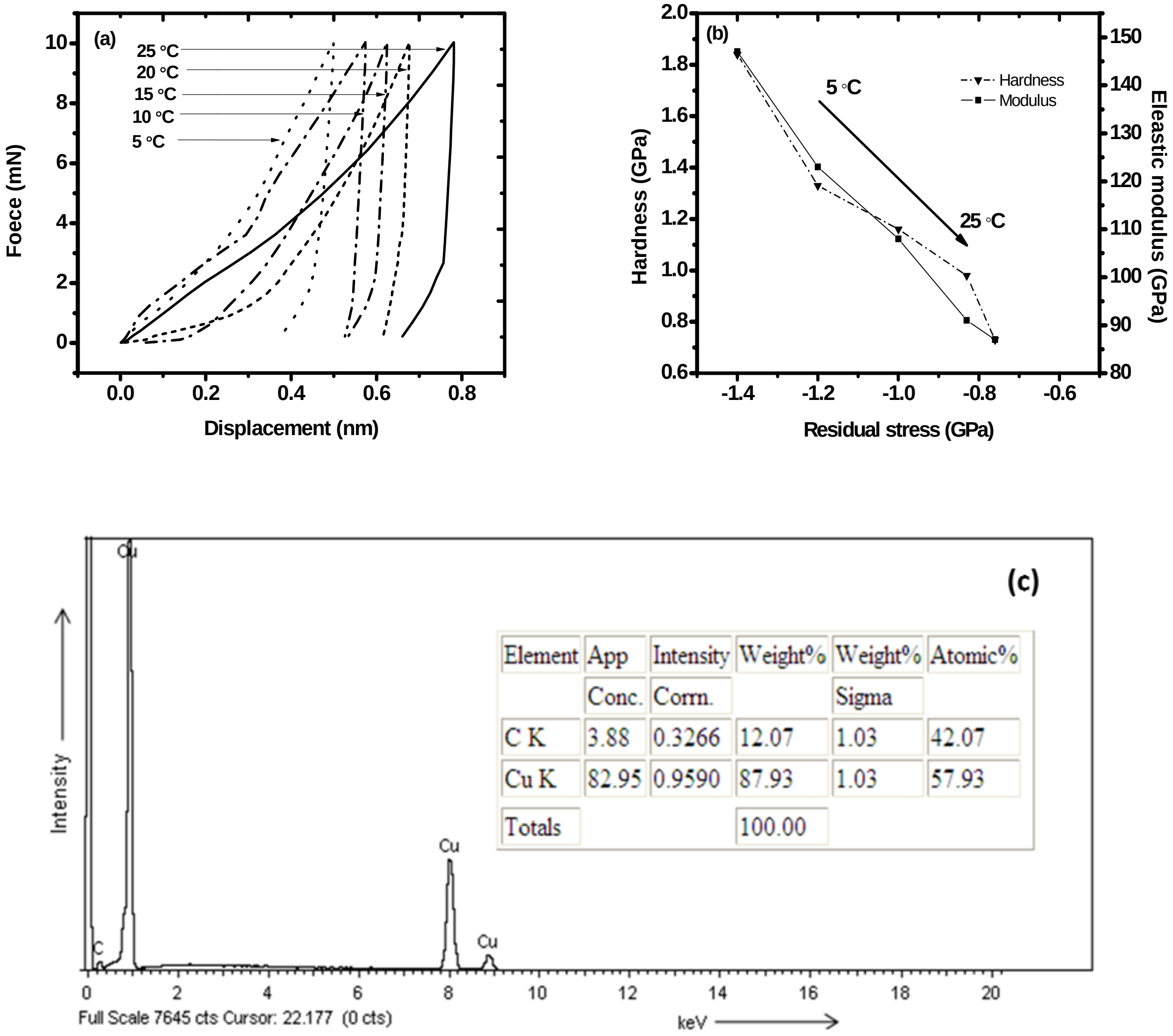

Element	App Conc.	Intensity Corrn.	Weight%	Weight% Sigma	Atomic%
C K	3.88	0.3266	12.07	1.03	42.07
Cu K	82.95	0.9590	87.93	1.03	57.93
Totals			100.00		

Fig. 4.42. (a) Load-displacement curves of Cu films (on graphite) at various deposition temperatures (b) Variation of hardness and elasticity of Cu films with residual stress (c) EDS plot of Cu deposit at 25 °C temperature

The determined Young's modulus values range from 87 -147 GPa. The variation of these parameters with compressive stress is also given in fig. 4.42b. With increasing compressive stress, the hardness and modulus increased from 0.78 and 87 GPa, respectively, to 1.86 and 147 GPa. During nanoindentation tests, it was known that both normal compressive stresses and radial shear stresses were mainly applied to the films. Basically, the radial shear stresses were much easier to induce cracking of the films. Residual compressive stresses in the films would retard the work of applied shear stresses, thus inhibiting crack initiation and propagation. Therefore, the highest mechanical properties were measured for the film containing the largest compressive stress.

In addition the intrinsic properties of thin films, such as microstructure and chemical composition, are believed to affect their mechanical properties. However in this study, all deposited Cu films containing different residual stresses had no special structures like textures or preferred orientations from XRD analyses and SEM observations. In addition, by SEM/EDS analyses, all the Cu films were identified to be of 100 at% copper (fig. 4.42c). Therefore, all the Cu films investigated in this study are believed similar from the viewpoint of their intrinsic properties. Similar relation has also been observed by other authors [28]. Moreover, the hardness and modulus of the Cu films prepared in this study were lower than the values of conventional Cu films as reported in some literatures [29].

From the viewpoint of atomic bonding force to interatomic spacing [30], the difference in the mechanical properties of Cu films containing different residual stresses can be realized as well. It is known that atoms locate at a balanced interatomic separation r_0, and the spacing changes under a force. Ideally, atomic bonds will not break, and deformation will not initiate until the interatomic separation exceeds the maximum value r_{max} under a force over the maximum atomic bonding force F_{max}. Although residual stresses in thin films will not affect the relation between the bonding force and interatomic spacing, however they change the spacing and meanwhile the force required to break bonds. Under the effect of residual compressive stresses, the interatomic spacing is compressed, and a larger applied force is needed to break bonds. In contrary, under residual tensile stresses, the spacing is enlarged, and the required force for plastic deformation may get lowered.

4.4.3.3 Surface adhesion

In addition to the topographical imaging, however, the AFM can also probe nanomechanical and other fundamental properties of sample surfaces, including their local adhesive or elastic (compliance) properties by measuring the forces on the AFM probe tip as it approaches and retracts from a surface. Fig. 4.43 shows a set of force-displacement curves for grain boundary for all the deposition temperatures respectively. The data in fig. 4.43(a) show a typical force curve for the sample probed at the grain boundary of the deposit at 25 °C. The results presented are an average of 20 readings. The approach curves show irregularities for the deposits at low temperatures. These may be due to the presence of long range force in the samples. The retraction curve estimates a rupture force of around 100 mN. Similar data were obtained for experiments performed at 20, 15, 10 and 5°C (data are shown in figs. 4.43(b–e), respectively). The data indicate that the tip-sample interaction is relatively small at low temperatures (minimum 54 mN at 5 °C). Hence, a strong decrease in the rupture forces is observed and achieving a maximum at 25 °C. The curves also indicate formation of multiple interactions between the tip and surface. The data for the surface's grain interaction with the AFM tip are shown in figs. 4.44(a-e). Unlike the force at rupture for grain boundaries, the rupture force at grains increases monotonously with decrease in deposition bath temperature. The above discrepancy may be due to the level of surface energy and interfacial tension present at the grains and grain boundaries of the deposit surface. However, the atoms present at the grain boundaries will contribute more to surface energies than the inter-grain atoms.

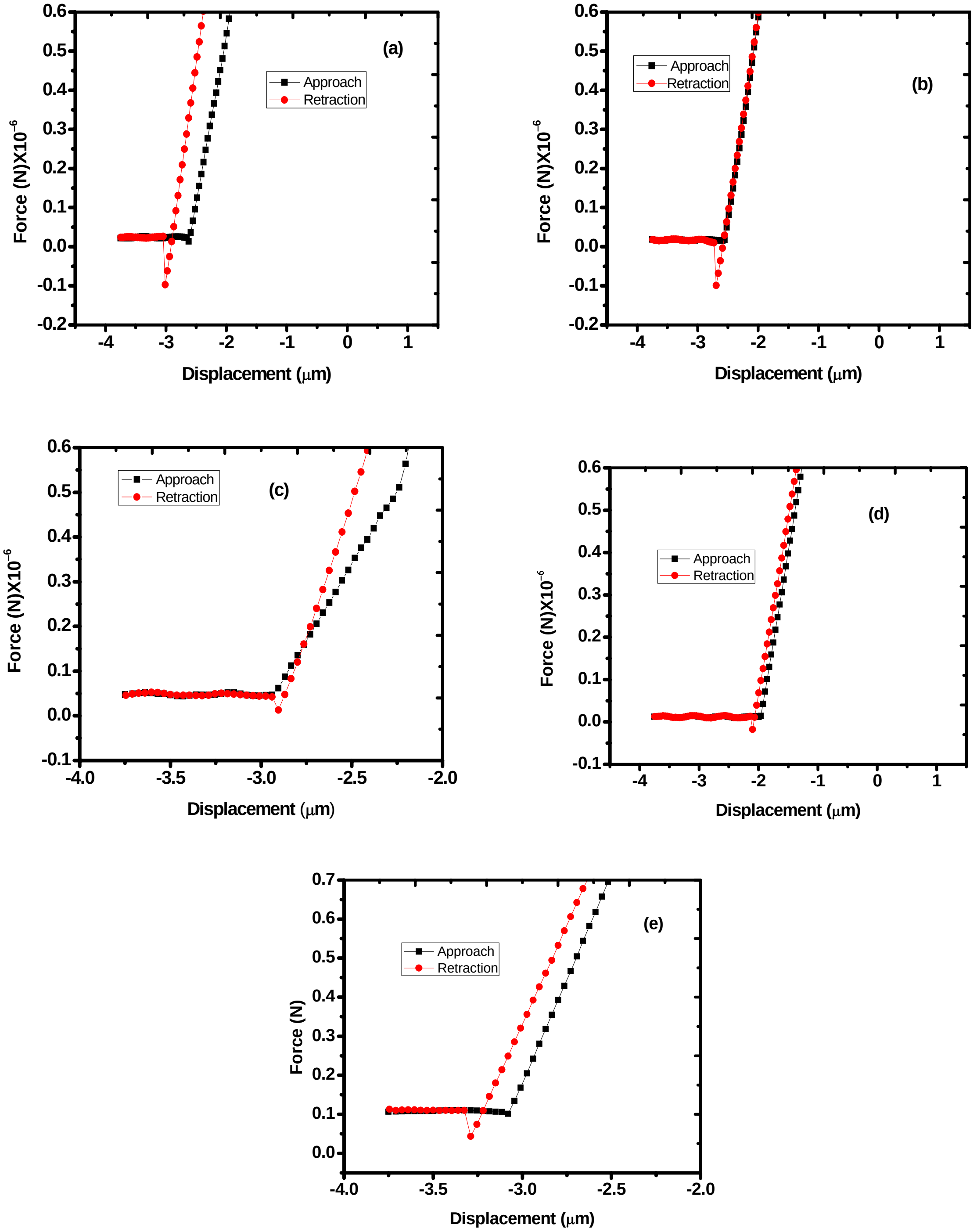

Fig. 4.43. Force-displacement curve at grain boundaries for Cu films (on graphite) deposited at (a) 25 °C,(b) 20 °C, (c) 15 °C, (d) 10 °C and (e) 5 °C temperatures

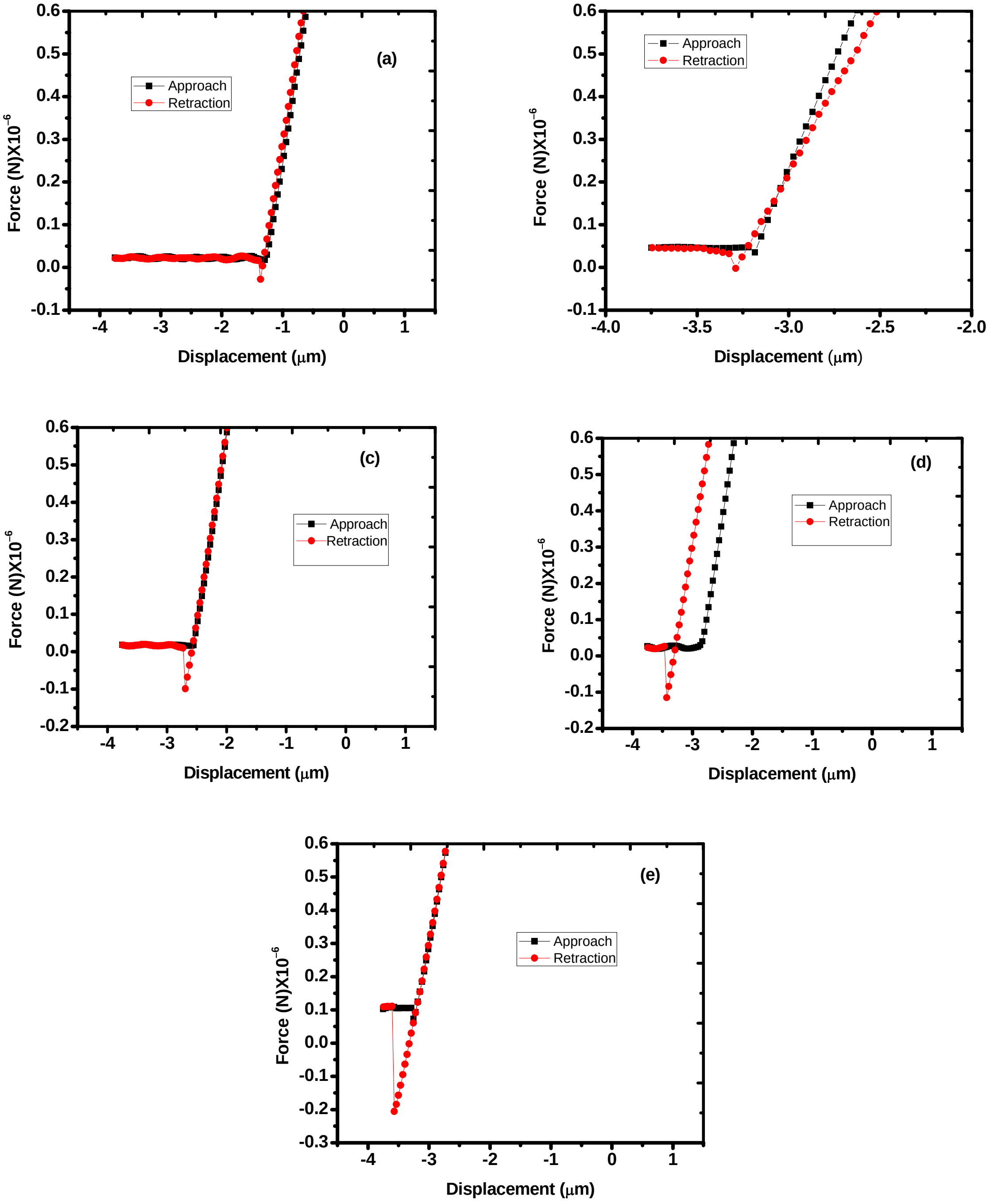

Fig. 4.44. Force-displacement curve at grain for Cu films deposited (on graphite) at (a) 25 °C, (b) 20 °C, (c) 15 °C, (d) 10 °C and (e) 5 °C temperatures

Figs. 4.45(a-b) shows the contact angle of water on the deposited surface at 25 °C and 5 °C respectively for surface energy measurements. The calculated values were found to vary in between 34.28 mN/m to 59.92 mN/m for films deposited at 25 °C to 5 °C respectively.

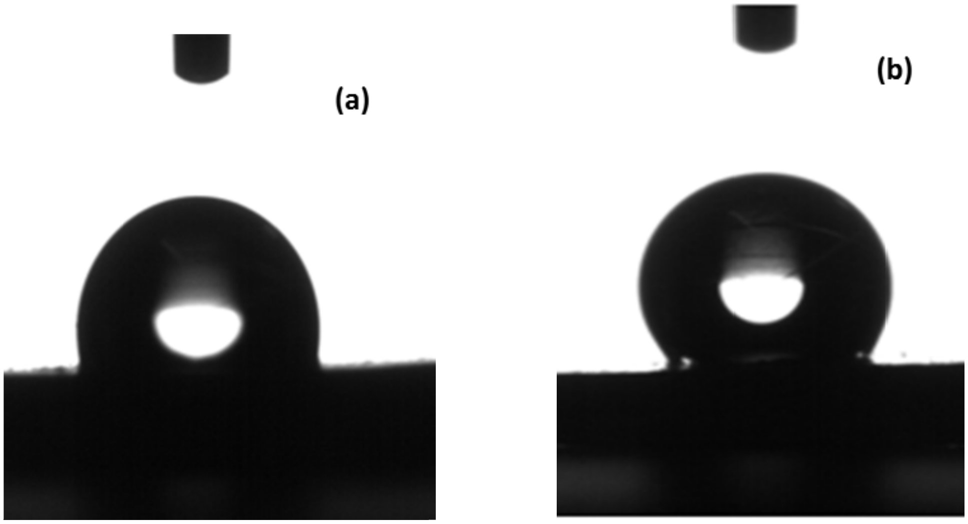

Fig. 4.45. Contact angle measurement with water droplets for Cu films deposited (on graphite) at 25 °C and (b) 5 °C

Hence, as the deposition temperature decreases, the amount of surface energy increases. If surface energy is high, then each atom finds it favorable to cohere while in contact with a foreign atom. Accordingly the maximum deflection of the tip/adhesion force at grains was for the deposit at 5 °C. If this is true, then it follows that when the interfacial tension is high, the force of adhesion is weak, since each species does not find it favorable to bond to the other. As the AFM tip approaches to the grain boundaries, the surfaces of tip and film will experience interfacial tension. With increase in approach of the tip the interfacial tension increases. This tension may be maximum for the atoms at finest grain boundaries, as they posses highest amount of surface energy.

This argument can be extended to the idea that when a surface is in a medium with which binding is favorable, it will be less likely to adhere to another surface, since the medium is taking up the potential sites on the surface that would otherwise be available to adhere to another surface. The explanation may support to the observations of increased deflections in the approaching curves for the grain boundaries. These data suggests that adhesion is more at grain boundaries for deposit at 25 °C and more at grains for 5 °C depositions. Hence as the volume fraction of grain boundaries increase for deposits obtained from low bath temperatures, the surfaces will be comparatively clean and chemically stable.

4.4.4. Summary

In this study, the effect of deposition temperature on the state and level of residual stresses in sono-electrochemically prepared copper thin films have been investigated. The mechanical properties including hardness, elasticity and surface adhesion and the relationship of residual stress with the mechanical properties in the deposited films have also been studied. The reduction of synthesis temperature reduces grain size of the films. Irrespective of deposition temperature, the stress was observed to be compressive and increased at low deposition temperatures (maximum −1.46 GPa at 5 °C). The refined grain size with the added effects of high adatom mobility and surface stress in presence of ultrasound might have resulted the above observation. The mechanical properties (*H, E*) show a reverse linear variation with the deposition temperature. The maximum of hardness and elasticity, 1.86 GPa and 147 GPa, occurs at 5 °C due to the Hall-Petch effect. A strong dependence of hardness and elasticity with compressive residual stress exists, which can be ascribed to the effects of residual compressive stresses to blunt crack tips and suppress crack propagation. In addition to the hardness and elasticity the surface adhesion at the grain surfaces were also increased with decreased bath temperature. However, the adhesion at grains boundaries was decreased. The discrepancy might have controlled by the variation of surface energy of the grains and grain boundaries and the interfacial tension between the AFM tip and the film's surface. Thus, a cleaner and chemically stable surface with good interface adherence may be expected for the films deposited at low bath temperatures.

4.3.5. References

1. M. Ohring, The Materials Science of Thin Films, Academic, Boston, MA, 1992.
2. R. Koch, The intrinsic stress of polycrystalline and epitaxial thin metal films, J. Phys. Condens. Mater., 6 (1994) 9519.
3. G. Hass, R. E. Thun, Eds., Physics of Thin Films, Academic, New York, 1966.
4. W. Buckel, J. Vac. Sci. Technol., 6 (1969) 606.
5. A. Bagchi, A.G. Evans, Interface Sci., 3 (1996) 169.
6. M.W. Moon, H.M. Jensen, J.W. Hutchinson, K.H. Oh. A.G. Evans, J. Mech. Phys. Solids, 50 (2002) 2355.
7. L.B. Freund, S. Suresh, Thin Film Materials: Stress, Defect Formation and Surface Evolution, Cambridge University Press, Cambridge, 2003.
8. M.D. Thouless, Thin Solid Films,181 (1989) 397.
9. F. Touyeras, J.Y. Hihn, X. Bourgoin, B. Jacques, L. Hallez, V. Branger, Ultrason. Sonochem., 12 (2005) 13.
10. M. Amin Alavi, A. Morsali, Ultrason. Sonochem., 15 (2008) 833.
11. T. Ohsaka, M. Isaka, K. Hirano, T. Ohishi, Ultrason. Sonochem., 15 (2008) 283.
12. U. Welzel, J. Ligot, P. Lamparter, A.C. Vermeulen, E.J. Mittemeijer, J. Appl. Crystallogr., 38 (2005) 1.
13. P. J. Withers, H. K. D. H. Bhadeshia, Materials Science and Technology, 17 (2001) 355.
14. G.C.A.M. Janssen, Thin Solid Films, 515 (2007) 6654.
15. International Centre for Diffraction Data (ICDD), Card No. 04-0863.
16. B. Okolo, Thin Solid Films, 474 (2005) 50.
17. M. Yu, J. Zhang, D. Li, Q. Meng, W. Li, Surf. Coat. Technol., 201 (2006) 1243.
18. T. Hanabusaa, K. Kusakaa, O. Sakatab, Thin Solid Films, 459 (2004) 245.

19. S. Kima, Jun-Ho Jang, Jeong-Soo Lee, D.J. Duquette, Electrochim. Acta, 52 (2007) 5258.
20. R.C. Cammarata, T.M. Trimble, D.J. Srolovitz, J. Mater. Res., 15 (2000) 2468.
21. F. Spaepen, Interfaces and stresses in thin films, Acta mater., 48 (2000) 31.
22. J.D. Finegan, R.W. Hoffman, Low-Energy X-Ray Attenuation Measurements for Elements of Low Atomic Number, J. appl. Phys., 30 (1959) 185.
23. R.W. Hoffman, Thin Solid Films, 34 (1976) 185.
24. W.D. Nix, B.M. Clemens, J. Mater. Res., 14 (1999) 3467.
25. C.E. Banks, R.G. Compton, Electroanalysis, 15 (2003) 329.
26. W.C. Oliver, G.M. Pharr, J. Mater. Res., 7 (1992) 1564.
27. http://en.wikipedia.org/wiki/Copper/01/07/2010
28. Yi-Chung Huang, Shou-Yi Chang, Chih-Hsiang Chang , Thin Solid Films, 517 (2009) 4857.
29. D. Beegan, S. Chowdhury, M.T. Laugier, Thin Solid Films, 516 (2008) 3813.
30. T.H. Courtney, Mechanical Behavior of Materials, McGrill-Hill, New York, 1990.

4.5. Effect of substrate on the deposited thin films

The mechanism of electrodeposition of copper thin film on aluminum has been studied under the influence of power ultrasound using cyclic voltammetry. The deposited thin films were characterized by x-ray diffraction, scanning electron microscopy and atomic force microscopy. Properties, including thermal and mechanical are further analyzed using differential scanning calorimetry and nano-indentation.

4.5.1. Introduction

Copper thin films have been emerged for their versatile applications in microelectronics, bacteriostatic, catalytic, magneto-recording, solar energy cells and sensor technologies. Thus, copper electrodeosition has been studied on numerous substrates starting from the non-metallic graphite to the metals and semiconducting substrates and more recently on hybrid materials to cater the needs of applications. Copper deposition on steel substrate [1], for example, was found to be continuous, fine and uniform with high overpotentials for hydrogen evolutions. Flaky copper deposition has been found on titanium foils as reported in [2]. Dendritic copper arms have been reported [3] when copper was used as electrode. The surface was very smooth for Cu deposited on Au and very rough and irregular on Ni-P [4]. Furthermore copper electrocrystallization is closely related to the substrate used. On glassy carbon [5] and steel [6], it follows the response predicted for 3D instantaneous nucleation with diffusion control [7]. Progressive nucleation and growth has been reported [8] when Au (111) was used as electrode. Others authors have reported island growth mode on amorphous carbon, polycrystalline silver [9,10] and tungsten [11] while the electrodeposition of this metal on conducting polypyrrole benzenesulfonate [12] has been characterized by an instantaneous nucleation and 3D growth. The comprehensive research of copper electrodeposition on pure aluminum is yet to be explored in wider scale. The very obvious effect of low temperature needs no detailed accounts [13,14] and the application of ultrasound to crystallizing systems offers significant potential for modifying and improving both processes and products [15]. Hence, the present work includes the complete electrochemical analysis, evolution of surface topography, mechanical and thermal properties of copper deposition on the metallic aluminum surface. Since the substrate materials have different atomic arrangements, the resulting microstructures and the underlying properties of the copper layers are expected to be different.

This article is written based on the unpublished work

A. Mallik, B. C. Ray, An analysis of the temperature-induced supersaturation effects on structure and properties of sono-electrodeposited copper thin films, **Ultrasonics** (Submitted).

4.5.2. Experimental details

Experiments were performed on O_2 free aluminum substrates of exposed surface area of 1 cm × 1 cm. Prior to the film deposition substrates were polished with emery papers followed by a diamond paste polishing on a polishing cloth in order to remove met nature of the surface and to get mirror like finish. The reproducibility of the results obtained depends on the quality of the polishing. After polishing, the substrates were cleaned with acetone and rinsed in distilled water. The dart particles on the surface of the substrate can adversely affect the nucleation and growth processes during film growth and can also lead to the inclusions or formation of many impurities. Hence it was important to clean substrates properly before they were put into the film deposition system. The bath composition was 10 g l^{-1} $CuSO_4$. $5H_2O$ + 40 g l^{-1} H_2SO_4. A 5 cm long platinum rod of 0.2 cm diameter and an Ag/AgCl electrode (Eco Chemie, Netherlands) served as counter and reference electrodes, respectively. Sonication applications were accomplished by a 20 kHz ultrasonic horn transducer system with 20% power output (Sonics & Materials, VCF 1500) fitted with a titanium probe of 25 mm diameter. Electrochemical measurements were conducted using a potentiostat/galvanostat (Eco Chemie Netherland, Autolab PGSTAT 12) having computer interface of GPES software. The deposits were obtained in the ramped potential of – 0.1 V to – 0.6 V at a sweep rate of 10 mV/s. Experimentation was carried out for a set of temperatures, 20 °C, 15 °C, 10 °C and 5 °C. A freezer was used to maintain low temperature conditions. Several techniques have been used to characterize the deposits. XRD patterns were recorded from 30˚ to 90˚ with a Philips X-pert MPD system diffractometer using Cu K_α at an accelerating voltage of 40 kV. Data was collected at a counting rate of 2 °/min. The K_α doublets were well resolved. Crystal size was estimated from the well established Williamson-Hall [16] formula applicable for adherent deposits. Microscopic studies to examine the morphology, particle size and microstructure were done by SEM (JEOL 6480 LV) equipped with an energy dispersive X-ray detector of Oxford data reference system. Micrographs were taken at an accelerating voltage of 10 and 15 kV for the best possible resolution from the surface rather than the interior of the deposit. EDS spectra were recorded at an accelerating voltage of 20 kV and the real collection time was around 1 min. AFM (SPMLab programmed Veeco diInnova) characterization study was done with a conducting P(n) doped silicon tip. Mechanical properties were studied by nanoindentation. The tests are done with a constant maximum load of 10 mN applied to the coating/substrate and the displacement is recorded for each of the temperatures. Thermal analysis data were recorded by a low temperature differential scanning calorimeter (Mettler-Toledo DSC 822). The program was set with a dried alumina powder. A 5 minutes isothermal run was given at 35 °C, and then a dynamic cycle run from 35 °C to 300 °C at a heating rate of 10 ºC/min and finally an isothermal run for 5 minutes at 300˚C. The tests were done in a N_2 atmosphere and were repeated for all the samples.

4.5.3. Results and discussions

4.5.3.1. Reaction kinetics

Cyclic voltammograms for copper electrodeposition at a scan rate of $10mVs^{-1}$ on aluminum substrates at different temperature values are presented in fig. 4.46.

This potentiodynamic study was used to define the potential region and to reveal relevant features of the process of electrodeposition. From the voltammograms it can be found that the metallic copper starts to deposit on the negative potential sweep, whence on, there is an increase in the cathodic current due to the copper crystallization. The diagnostic potential crossover for the confirmation of diffusion controlled nuclei formation has occurred for each of the temperature values (fig. 4.46a) in silent condition. Two point crossovers between anodic and cathodic current curves also appear on the reverse potential sweep. This could be an indication of mixed mass and charge transport limited electrodeposition. However, the dominating mass restricted phase formation was then better comprehended by observing the linear variation of current with the square root of scan rate ($\gamma^{0.5}$) as shown in fig. 4.46c. The depositing current has attained a constant value in the negative scan after a potential of -250 mV. Apart from the phase kinetic characterization, the cross over potential can be related to the equilibrium potential, in this case $Cu^{2+}(aq)/Cu(s)$, when it is independent of the inversion potential. Equilibrium potential has turned out to be a function of temperature, shifting towards more negative values as the temperature decreased. Similar trend has been observed by Ramirez *et al* [17] for deposition of silver at high temperatures. It was also revealed that the reduction potential of Cu^{2+} ions

has become more anodic with reduction of bath temperature. It is reasonable to believe that the initial high availability of ions in the ionic atmosphere, because of the opposition on the chaotic atom movement at low temperature values, has increased the tendency of reduction of Cu^{2+} ions. When copper deposition was performed with ultrasound, the event of phase formation was found to be charge transport controlled (fig. 4.46b). The cathodic regions do not consist of cathodic peaks. Furthermore the potential crossovers are present in the positive potential region in CV curves.This is consistent with no significant depletion of the active species at the electrode surface, and, therefore, implies charge (or interfacial) control of the deposition. Further the scans have two effects on the deposition part of the transient. The potential required for deposition to begin becomes less negative, and the amount of charge transferred increases steadily. The scans also have irregularities. This can be explained by a combination of ablation of material from the surface and rapid random changes in the surface ion concentration as a result of cavitation consistent with ultrasonic streaming increasing the rate of transfer of metal ions to the surface.

Now considering the stripping peaks, copper dissolution in the absence of sonication is an interesting case. On the reverse part of the deposition loop there is a secondary peak, the size of which increases as the bath temperature decreases. In suspecting simultaneous side reactions, two CV sample were run upto the first (200 mV) and second peak potential (288 mV) and surface topography as well as spectroscopic analysis were done. The SEM and EDS analysis (not shown here) revealed Cu phases of both oxidation states. Hence, a seemingly possible explanation may be the interplay between charge and diffusion control kinetics for the dissolution reactions in the absence of ultrasound source. Diffusion being the dominating phenomena at low temperatures, the secondary peak heights has increased progressively. Hence the system is comparably more of charge controlled at high temperature. The perception is further supplemented by the single stripping peak with sonication, where the system kinetics depends on the rate of discharge and not the diffusion of ions at the electrode. There is also a shift of the insonated dissolution peak potential towards the equilibrium Cu dissolution.

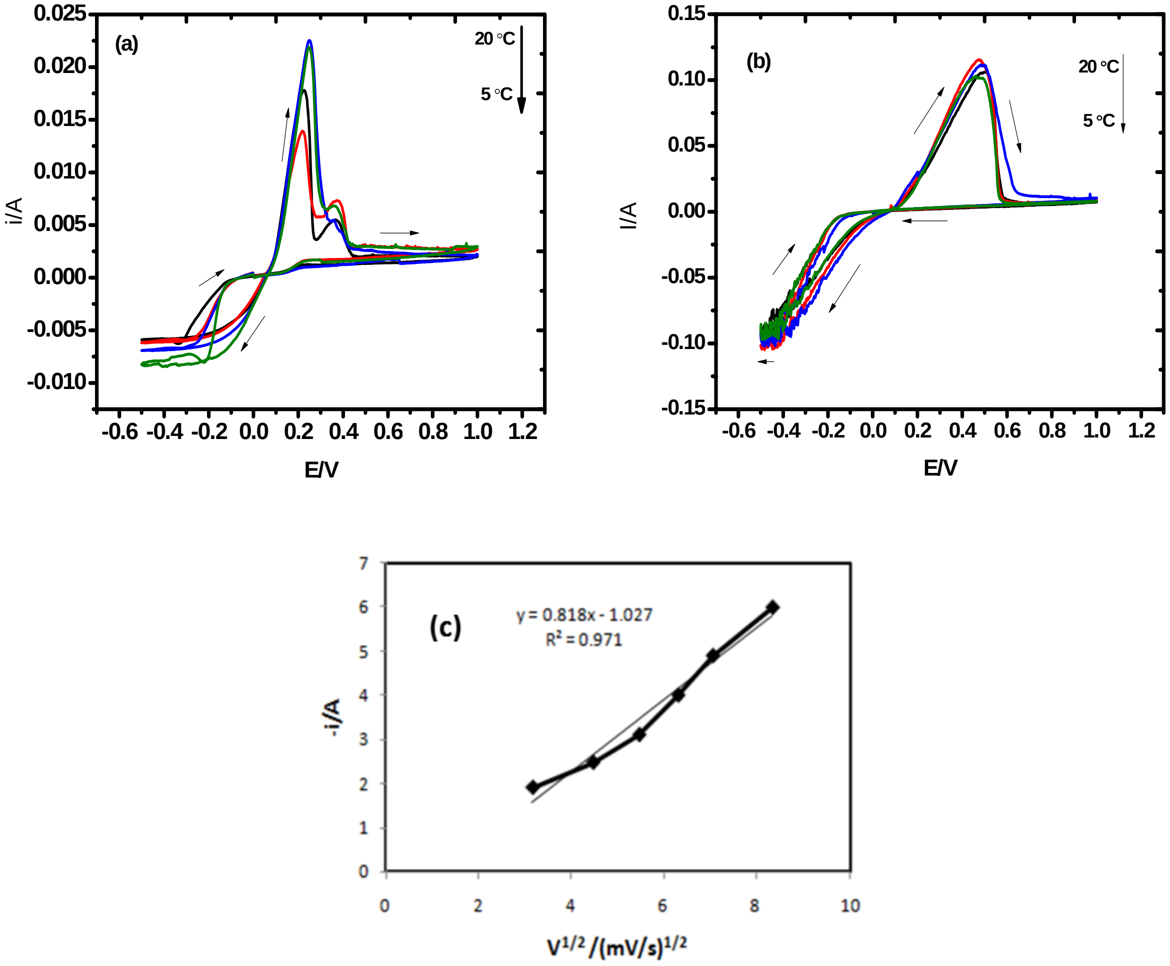

Fig. 4.46. Cyclic voltammetry for copper deposits on Al at various temperatures in conditions of (a) silent, (b) sonication and (c) dependence of scan rate on current density in silent condition

In order to quantify this, the charges under the deposition and stripping peaks of the scans were measured for both insonation and silent conditions, and the ratio of stripping charge to deposition charge data are given in Table 4.8.

Table 4.8: Stripping charge/Deposition charge (Q_a/Q_c) of silent and sonicated copper deposits on aluminum

Temperature (°C)	Stripping charge/Deposition charge (Q_a/Q_c)	
	Silent	Sonication
20	0.8	0.9
15	0.72	0.99
10	0.7	1.01
5	0.6	1.01

In silent conditions, the efficiency of the redox process is below 1. This may be due to simultaneous oxidation of the copper atoms during discharging and adsorption of sulfur atoms at the cathode surface. The presence of oxygen and sulfur is confirmed in the next section of phase and structural analysis. The efficiency of deposition under sonication is found to be increased at low temperatures. This suggests poor adherence of copper at elevated temperatures. Hence ultrasonic ablation removes materials from the anode before it can be stripped, and is most apparent for deposition at 20 °C.

4.5.3.2. Phase and structure analysis

The XRD patterns of the samples synthesized at different reaction temperatures are as shown in figure 4.47. The patterns show that the films are polycrystalline in nature and the highest intensity diffraction peak was the (111) resulting from depositing the close packed planes parallel to the surface. This may conclude that deposited Cu layers had strong [111] texture. The diffraction peaks at 2θ = 43.27, 50.34, 74.11, 89.93 can be indexed as the (111), (200), (220), (311) planes of copper with cubic symmetry respectively [18]. With decreasing temperature, broadening increases where as intensity decreases. Average crystallite size of copper deposit varies from70.44 nm to 45.99 nm with reduction in deposition temperature from 20 °C to 5 °C. Concerning the morphology of the deposited copper, SEM (at 10000 X) and AFM analysis of the samples for all experimented temperatures are demonstrated in figs. 4.48 -4.50 In the presence of continuous nucleation of new grains (linear applied potential) the microstructure of the deposits are comparatively uniform and finer at low temperatures. Figs. 4.48(a)-(d)

The silent deposit at 20 °C comprises of branched dendritic structures with branches of about 3 – 5 µm.

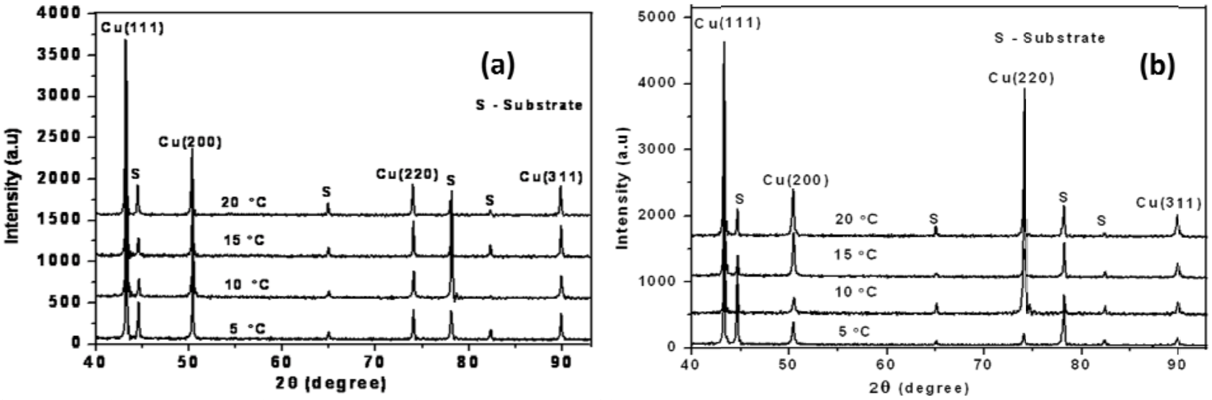

Fig. 4.47. XRD patterns of copper thin films prepared at different temperatures (a) without sonication and (b) with sonication on aluminum

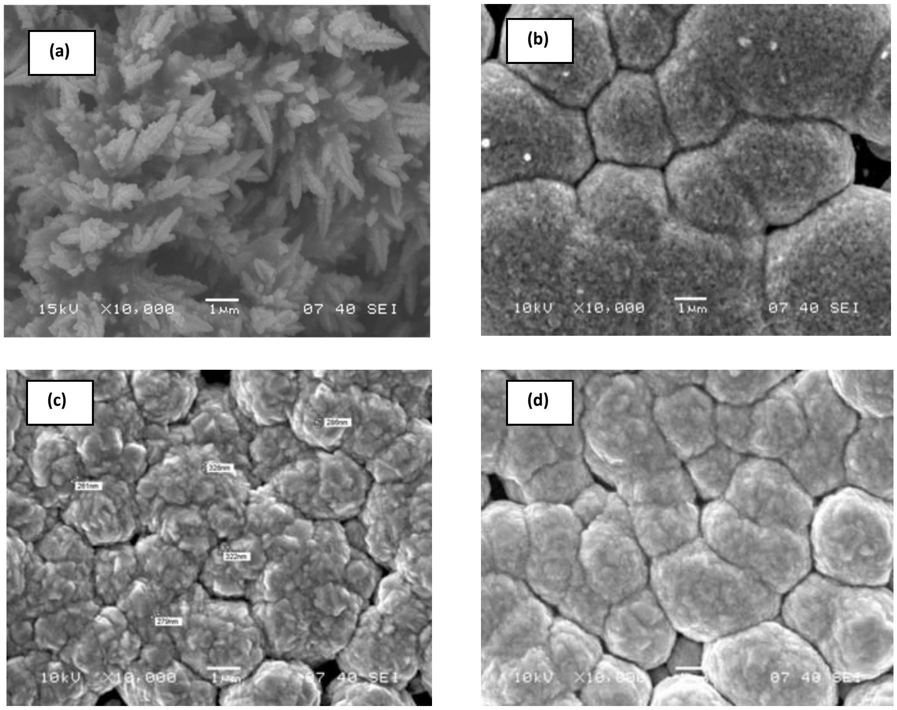

Fig. 4.48. SEM micrographs of electrodeposied copper on aluminum at (a) 20 °C, (b) 15 °C, (c) 10 °C and (d) 5 °C temperatures at magnifications of 10000X

The pattern indicates that the growth is globally diffusion-controlled. In such system, mass transport is dominated because of the limitation of the electrolyte concentration which reaches to the substrate. As a result, the crystals will tend to grow randomly outwards towards regions of higher concentrations to form the dendritic branches. The fine powders may readily be used in preparation of industrial parts through powder metallurgy without further preparation. As the temperature is progressively taken lower, the images, figs. 4.48 (b)-(d), reveal the formation of hemispherical centers randomly distributed on the electrode surface. The images also clearly demonstrate that the island density and tendency of agglomeration increases, and the average island size gets smaller, upon lowering the temperature. The projected copper dendrite arms have become blunt, resulting in near-circular disks and hemisphere islands. This is a typical feature of diffusion control, as inferred from the cyclic voltammogram in fig. 4.46 (a). Modification of the diffusion controlled nucleation model from planar to individual hemispherical diffusion regimes explains well the spherical structure. Transition from the disordered dendritic pattern to the ordered structures may occur as the parameters representing crystalline anisotropy and supersaturation are varied. Thus, the fact that temperature can alter the supersaturation level, can clearly be visualized from the findings.

The diverging dendritic copper arms seem to be folded to form the most common mushroom, but faceted peripheral structures are formed in the presence of ultrasound, as shown in fig. 4.49. In addition, the deposits also show compact and smooth microstructure. The mushrooms have become gradually smaller with distinct contours at low temperatures. The 3D height mode topographical AFM images of large scan area, 5 × 5 µm^2, for the sonicated deposit are shown in fig. 4.50. The most heighted grains belong to the range of 1.62 µm. Average grains have the height of 599 nm. The average roughness factor is 386 nm. Deposits at lower temperatures are made of closely spaced finer copper mushrooms. The grains at 15 ºC do fall in the height range of 0-733 nm with the average roughness factor of 152 nm. Significant in appearance can be observed at 10 °C. The micro domains have started engulfing their boundaries, which may indicate the compactness of the films.

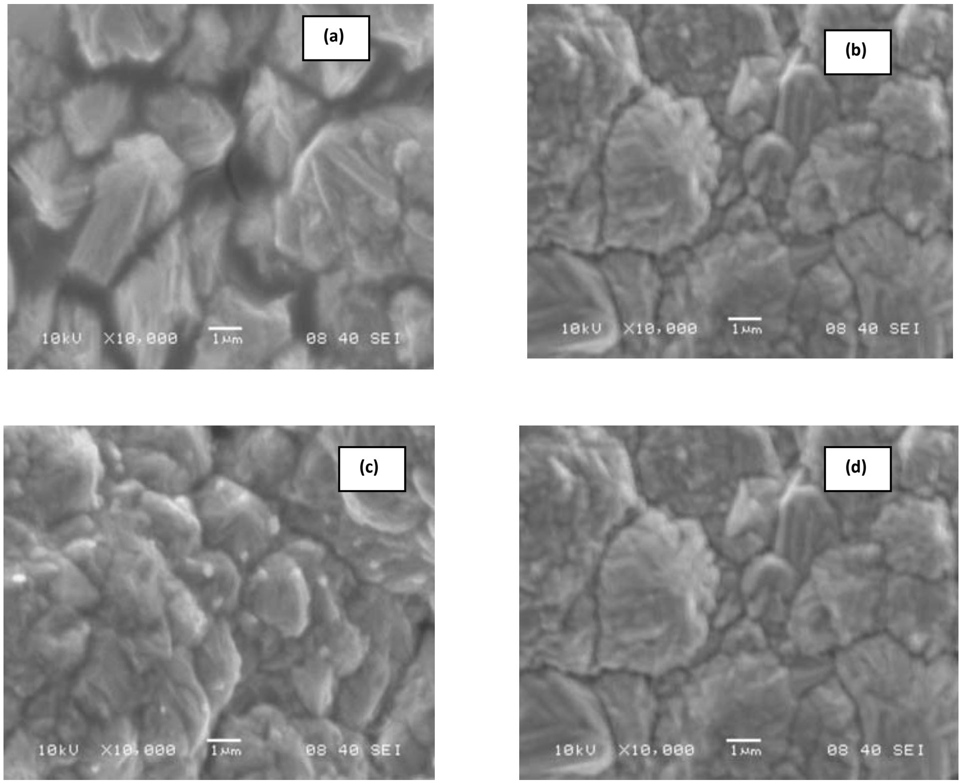

Fig. 4.49. SEM micrographs of sono-electrodeposied copper on aluminum at (a) 20 °C, (b) 15 °C, (c) 10 °C and (d) 5 °C temperatures at magnifications of 10000X

current efficiency even at low temperature. The non-uniform coalesced mushrooms at 10 °C are observed to have a greater degree of smoothness at 5 ºC. Micro-polishing of the surfaces may result high coplanarity and smooth surface for use in electronic industries.

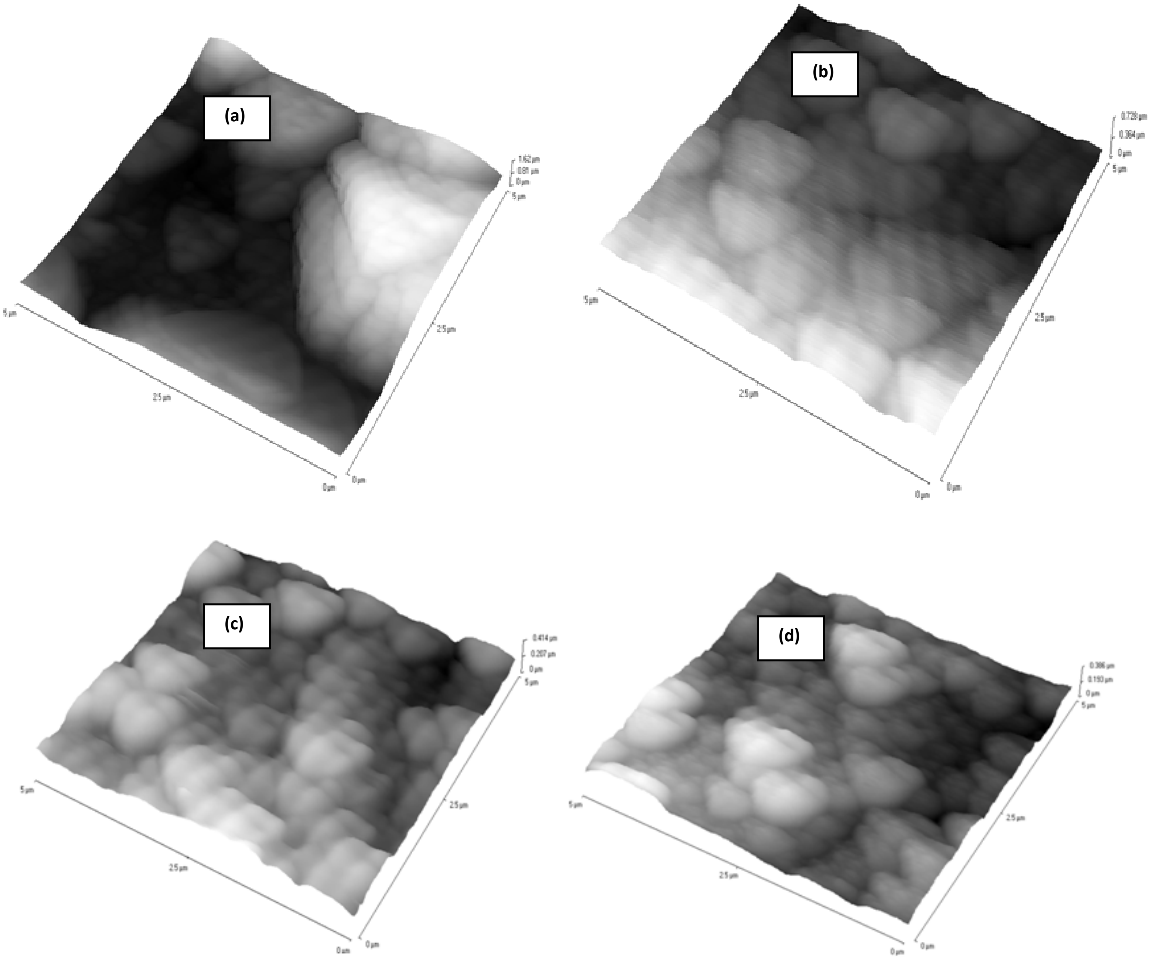

Fig. 4.50. AFM micrographs of sono-electrodeposied copper on aluminum at (a) 20 °C, (b) 15 °C, (c) 10 °C and (d) 5 °C temperatures

Sonicated deposits are better covered than the silent deposits confirming higher throwing power and The AFM micrograph at 5 ºC is shown in fig. 4.50 (d). The grains have the average height and roughness factor of 167 nm and 60 nm respectively. This result indicated the highest surface finish of the deposit at 5 °C bath temperature, among all the deposits. An exclusive explication on the frequently observed mushroom structures is still inadequate in the open literature. And the explanation stems from the well established fact that electric charge neutrality can be assumed, except within a thin boundary layer of exceptionally high electric field (10^6 or 10^7 V/cm), at the surface of the cathode [19]. The electrodeposition processes, uniform forward and backward diffusion of adsorbing depositing ions and desorbing byproducts respectively, occur in this very thin region of metal-solution interphase. And the nature of a kinetically control system is to form a layer as thin as possible for the ease of the sequence of processes. Ultrasound waves could indeed thin down the diffusion layer and reduces the depletion of electroactive surface near the substrate [20], resulting in the formation of facets on the existing nuclei.

A comparative compositional analysis from the EDS result has given in Table 4.9. The results show that the sonicated deposits are cleaner as compared to the silent.

Table 4.9: EDS compositional analysis of silent and sonication copper thin films deposited on aluminum

Temperature (°C)	Elements (at%) Silent			Elements (at%) Sonication		
	Cu	O	S	Cu	O	S
20	72	26	2	100	-	-
15	65	34	1	100	-	-
10	62	37	1	100	-	-
5	54.5	45	0.5	100	-	-

The findings do support the in-situ cleaning and the inconvenience for the undesired reactions as reported by the authors for deposition onto graphite electrodes.

4.5.3.3. Thermal stability analysis

Fig. 4.51 shows the heat absorption measurement data for the films. The scale is represented in exothermic setting. It can be observed that the heat absorved with decreased temperature increases from 2 to 8 mW. However, we have not calculated exactly the specific heat change associated with the finegarined deposits, but the change in amount of heat absorbed with the reduction in deposition temperature. The above observations can be explained by the fact that, the specific heat of a bulk solid was calculated by Einstein in 1910 by assuming that all of the atoms have one and the same vibration frequency. In 1940, it was found that there is a soft-phonon mode, the frequency of which varies with temperature, moving toward the Rayleigh line and reaching zero at the transition temperature so that there is a contribution to the specific heat that vanishes at the transition temperature. Hence phonon scattering generated at the grain boundaries of nanocrystals are well expected. This scattering generates new phonon frequencies in a nano-crystal, which contributes to the specific heat in terms of lattice energy. Thus, the size dependence of the lattice energy, E, is described by equation (4.13) [21]:

$$E = b_1 \mathrm{T}^4 \exp(-\alpha d) \quad (4.13)$$

Where, b_1 and α are constants, T is absolute temperature. Thus, there is a large change in lattice energy for a small change in size, d , of the nanocrystal due to phonon scattering at the surface. Though the level of energy absorbed was varied, fims were stable even at 300 °C unlike the films deposited onto graphite substrates. Hence, films are expected to be stable at high temperatures and can be used without any alteration in the film's initial properties.

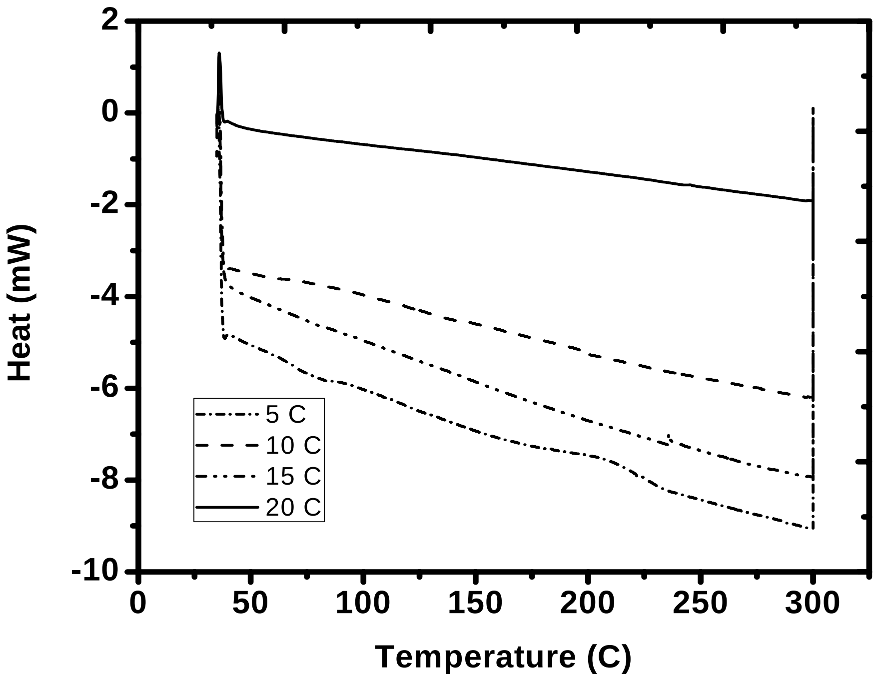

Fig. 4.51. Thermal analysis (by DSC) curves of sono-electrochemically deposited thin films onto aluminum

4.5.3.4. Mechanical property

Fig. 4.52 depicts the variations of thickness and mechanical properties of the films produced at different deposition temperatures. The maximum load exerted on the films was 10 mN. Thickness of films were measured by the peak and valley method of AFM analysis. In the nanoindentation technique hardness and Young's modulus can be determined by the Oliver and Pharr method [22], where hardness (H) can be defined as, $H = \frac{P_{max}}{A_c}$, P_{max} is maximum applied load, A_c is contact area at maximum load. The ratio of maximum indentor depth to coating tickness should be limited at 1/5, 1/10 and even 1/20 to eliminate the influence of substrate deformation on measurement. The maximum displacement observed was 350 nm, 1/5 times of the total thickness of the coating (1.7 μm). The reported hardness value of copper thin films is in the range of 1-3 GPa [23], which are harder than the aluminium substrate (0.1-1 GPa). Hence the coating hardness values may considered to be not affected by the substrate effects. It can be seen that the displacement decreases with decreasing temperature. The hardness values observed are in the range from 1.26 – 2.7 GPa.

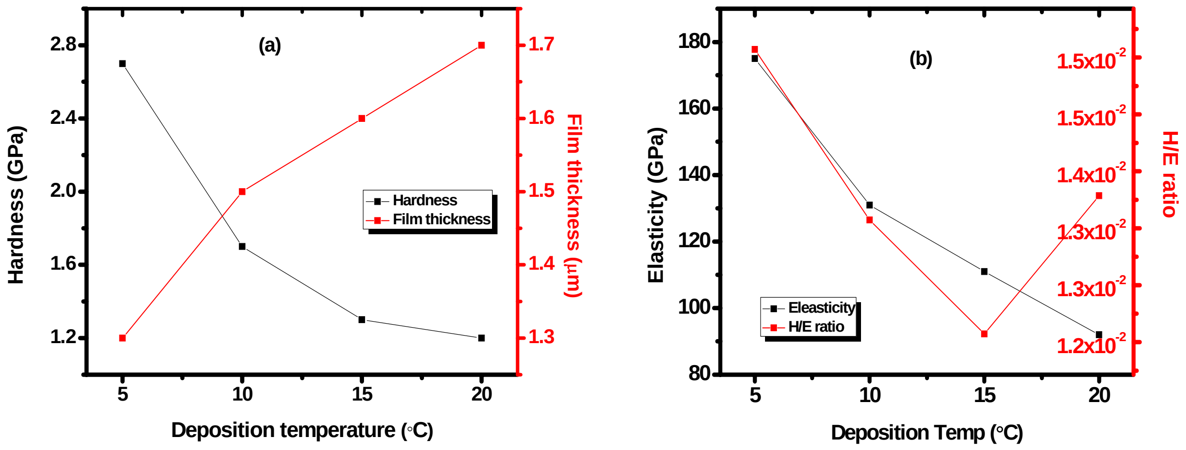

Fig. 4.52. Variation of (a) hardness and thickness and (b) elasticity and H/E ratio values of deposited copper thin films on aluminum with deposition temperatures

Copper films at temperatures below 15 ºC have hardness above the hardness values for pure crystalline copper (1-1.5 GPa) [24]. This can be attributed both to grain size strengthening (small grains compared to the grain size of pure crystalline copper) and/or strain hardening. The grain size strengthening is determined by the strength of Cu grains (H_0) and the average grain size (d) of Cu according to the Hall-Petch relation ($H = H_o + kd^{-1/2}$), where k, Hall-Petch coefficient accounting the grain boundary resistance to dislocation movement. Thus, the increased dislocation piled up with decreasing size has resulted such high strength in films. The determined Young's modulus values range from 92 -175 GPa. Recently Leyland et. al. [25] have reported, that moderately soft materials can achieve high wear resistance and ductility, if they pose high *H/E* ratio. The H/E values are greater than 0.01, obtained for almost at all the temperatures and exceeds for pure crystalline copper (0.008) [26]. This suggests that fairly improved wear properties can be achieved for this inherently soft material.

4.5.4. Summary

The results presented in this section elucidate that suitable tuning and control of the morphology and hence the properties of copper electrodeposits can be realized from low temperature acidic supersaturated bath under acoustic activation. The effects of ultrasound and temperature for copper electrodeposition on aluminum were studied using cyclic voltammetry. Silent deposition showed a mixed kinetics control and sonicated system were dominantly charge transfer control. The deposits from the doubly activated bath have the distinct mushroom like morphologies. Further, the addition of sonication environment has lead to substantial variations of thermal and mechanical properties of the copper thin films. Thus, the beneficial sonication effect on deposits may be effortlessly and suitably manipulated depending on the requirement, which holds a great promise for the future.

4.5.5. References

1. Chi-Chang Hu*, Chi-Ming Wu, Surface and Coatings Technology 176 (2003) 75–83.
2. Zulkarnain Zainal*, Anuar Kassim, Mohd Zobir Hussein, Chuah Hang Ching, Materials Letters 58 (2004) 2199– 2202.
3. N.D. Nikolić a, , K.I. Popov b, Lj. J. Pavlović a, M.G. Pavlović a, Surface & Coatings Technology 201 (2006) 560–566.
4. Anette A. Rasmussen a, Jens A.D. Jensen a,1, Andy Horsewell a, Marcel A.J. Somers a,* Electrochimica Acta 47 (2001) 67–74.
5. G. Fabricius, K. Kontturi, G. Sundholm, Electrochimica Acta 39 (1994) 2353.
6. L. Bonou, M. Eyraud, J. Crousier, J. App. Electrochem. 24 (1994) 906.
7. B. Scharifker, G. Hills, Electrochimica Acta 28 (1983) 879.
8. M.H. HoÈlzle, V. Zwing, D.M. Kolb, Electrochimica Acta 40 (1995) 1237.
9. P.V. Brande, R. Winand, Surf. Coat. Technol. 52 (1992) 1.
10. P.V. Brande, R. Winand, J. App. Electrochem. 23 (1993) 1089.
11. M. Peykova, E. Michailova, D. Stoychev, A. Milchev, Electrochimica Acta 40 (1995) 2595.
12. R.J. Nichols, D. SchroÈer, H. Meyer, Electrochimica Acta 40 (1995) 1479.
13. J. S. Santos, R. Matos, F. Trivinho-Strixino, E.C. Pereira, Electrochim. Acta, 53 (2007) 644.
14. E. W. Bohannan, C. C. Jaynes, M. G. Shumsky, J. K. Barton, J. A. Switzer, Solid State Ionics, 131 (2000) 97.
15. A. Gedanken, Ultrason. Sonochem., 11 (2004) 47.
16. G. K. Williamson, W. H. Hall, Acta Metall., 1 (1953) 22.
17. C. Ramirez, E. M. Arce, M. Romero-Romo, M. Palomar-Pardave, Solid State Ionics, 169 (2004) 81.
18. International Centre for Diffraction Data (ICDD), Card No. 04-0863.
19. M. Paunovic, M. Schlesinger, Fundamentals of Eelectrochemical Deposition, Wiley Interscience, USA, 2006.
20. F. Marken, R. P. Akkermans, R. G. Compton, J. Electroanal. Chem., 415 (1996) 55.
21. N. Srivastava, Nano Lett., 2 (2002) 21.
22. W. C. Oliver, G.M. Pharr, J. Mater. Res., 7 (1992) 1562.
23. Beegan, S. Chowdhury, M.T. Laugier, Surf. Coat. Technol., 201 (2007) 5804.
24. http://en.wikipedia.org/wiki/Copper/21/06/10
25. A. Leyland, A. Matthews, Wear, 246 (2000) 1.
26. K. W. McElhaney, J.J. Vlassak, W.D. Nix, J. Mater. Res., 13 (1998) 1300.

Chapter 5

Conclusions

The present investigation emphasizes the synthesis of copper thin films by electrodeposition route at reduced bath temperatures in presence of ultrasound. In the first instance, an extensive phase and structural study has been performed to enlist the sole as well as synergistic effects of low temperature and sonication on the deposition characteristics. Subsequently the alterations in the nucleation and growth mechanisms guiding the morphological variations have been included. It also contributed to give the variations in the mechanical properties and ex-situ growth behavior of the films. In order to explore the potential applications of these films, synthesis was carried out on different substrate. The main advantage of the coupling effect is that they promote synthesis of ultrafine grained adherent deposits. In this regard, the following outcomes could be drawn based on this study:

- There was quite variation in the structure and morphology of the copper deposited from the silent and sonicated baths. Copper depositions were crystalline for both the conditions of presence and absence of ultrasound. Deposits in sub-ambient temperatures for silent condition were highly branched and sharp dendritic structure while sonicated deposits were spherical with uneven grain distribution. The sonicated deposits were also perforated, which may be an effect due to micro-stream jetting. Compared to sub-ambient depositions, well covered and agglomerated bright copper spheroid like deposits were obtained for sub-zero temperatures under sonication.

A thorough compositional analysis of the deposits by EDS shows a cleaner sonicated deposit as compared to a highly oxidized silent deposit, which also contains traces of adsorbed sulfur. However, deposition at far below sub-zero temperature has resulted rougher surfaces. Therefore, merely sub-ambient temperatures were chosen for nucleation and kinetics studies.

- A novel understanding of the nucleation mechanism involved in sonoelectrochemical synthesis of copper has been proposed. The hypothesis was experimented by correlating the kinetics of the nucleation mechanism with the microstructural evolution. The diagnostic nucleation transient did consist of crests and troughs, hence multiple maxima and nucleation cycles in-place of single maxima for one nucleation cycle. An increase of nucleation population density and reduction of grain size was observed for protracted sonication. In contrast, the deposits without sonication consisted of coarse grains. Hence, sonication possibly imparts the ambience for promoting secondary nucleation by breaking the existing primary nuclei in addition to the primary nucleation.

- While studying the reaction and nucleation mechanism of copper at low temperatures in presence of ultrasound, it was observed that a net increase in anodic, cathodic and depositing currents was observed for all sonication experiments in comparison to their silent counterparts. A positive anodic peak shift was observed for insonicated CVs. The redox process in silent condition was controlled by mixed diffusion + ions transfer and under sonication the probable mechanism was charge transfer controlled. The stripping charge/deposition charge ratio was found to be increased for sonication condition, which can be due to the absence of simultaneous undesired cathodic reactions and good adherence of the deposits to the substrate. Copper nucleates according to 3D instantaneous mechanisms for all temperature ranges. The extent of nucleation was found to be increased at low temperatures. A transition of dendritic type morphology to spherical copper with better surface coverage was observed. The addition of sonication has further triggered the nucleation process by stimulating the biphasic nucleation sequence i.e. primary nucleation due to the extreme high level of localized supersaturation at low temperatures and secondary nucleation by fragmentation of the existing primary nuclei. There was no variation in the morphology habitat. The spherical copper grains were found to consist of nanometer sized agglomerates. Diffusion coefficients and nuclei population density were calculated for each temperature range for both presence and absence of ultrasound. It was found that both the quantities increased in presence of ultrasound.

- The character of the stress in copper films/graphite substrate was of compressive in nature. The stress–deposition temperature curves suggest that the compressive stress increased as the film deposition temperature decreased. The most significant generative origins of the film stress are the effect of increased adatom mobility, surface stress and good island substrate attachment. The hardness increased from 0.78 (at 25 °C temperature) to 1.86 (at 5 °C temperature) whereas modulus from 87 GPa (at 25 °C temperature) to 147 (at 5 °C temperature). The compressive residual stress was found to be varied linearly with decreasing deposition temperature. Hence, residual compressive stresses were expected to blunt crack tips and suppress crack propagation as the films got refined structure. In addition to the hardness and elasticity the surface adhesion at the grain surfaces were also increased with decreased bath temperature. However, the adhesion at grains boundaries was decreased. Thus, a cleaner and chemically stable surface with good interface adherence may be expected for the films deposited at low bath temperatures.

- The effect of bath temperatures and sonication on the non-isothermal post deposition growth behavior was investigated by examining the growth kinetics and condition of the surface microstructure. The DSC thermograms were found to have multi peaks, past the main exothermic growth peak for high temperature films. While low temperature films have single peaks. Further the application of Kissinger method at several heating rates allowed us to estimate the activation energy for growth, and was found to be controlled by grain boundary self diffusion for all the film crystallization temperatures. The XRD analysis of the films after and before thermal treatment had visible variations. The calculated grain size was increased for all films after DSC scan. Bimodal and uniform grain distributions were observed for the post treated high temperature and low temperature films respectively. The surface roughness was also found to be increased after DSC scan for deposits at 25, 20 and 15 °C. Surface energy estimations of the films showed an increase tendency for the films synthesized at high bath temperatures, whereas films deposited at 10 and 5 °C have reduced values than the as-deposited conditions. This did lead us to introduce a second phase of abnormal grain growth of the copper grains, favorable after the completion of the stable and normal grain growth for the high temperature films. Moreover comparisons between the DSC, surface morphology and texture analysis by SEM and AFM may suggest a transition of abnormal growth to normal mode of growth behavior as the film synthesis temperature were reduced.

- Comparisons of the results obtained on aluminum substrate elucidate that suitable tuning of the morphology and hence the properties of copper electrodeposits can be realized from low temperature acidic supersaturated bath under acoustic activation. Silent deposition showed a mixed kinetics control while sonicated system was dominantly charge transfer control. Films were crystalline in structure. The spherical copper domains of the deposits on graphite substrates have been converted to mushroom structures on aluminum electrodes. There was a significant change in the variation of energy absorbed for films that deposited at different bath temperatures. However, unlike films on graphite substrates, films did not show any growth tendency upto 300 °C. The observed hardness values were higher than the films deposited on graphite. Furthermore the soft films were found to have good wear properties. Thus, the beneficial sonication effect on deposits may be effortlessly and suitably be manipulated depending on the requirement, which holds a great promise for the future.

Appendix A

A.1. Thickness calculation

The procedure for determination of thickness of the deposits can be presented in the following way: The calculation is based on Faraday's law, "in electrolysis, 96500 Coulombs of electric charge produce chemical charge of 1 g equivalent." If the thickness is d (cm) and the sample has an area A (cm^2), the quantity of electricity passed is Q (C), M the atomic mass (gm) with a density of ρ (gm cm^{-3}) and *n* represents the number of electrons involved in the reduction of the ion. Then the thickness of materials deposited can be calculated as:

$$d = \frac{QM}{96500 nA\rho} \quad \text{(A.1)}$$

A.2. Stress measurement by curvature analysis

Curvature measurements are frequently used to determine the stresses within coatings and layers. The deposition of a layer can induce stresses which cause the substrate to curve, as illustrated in figure below.

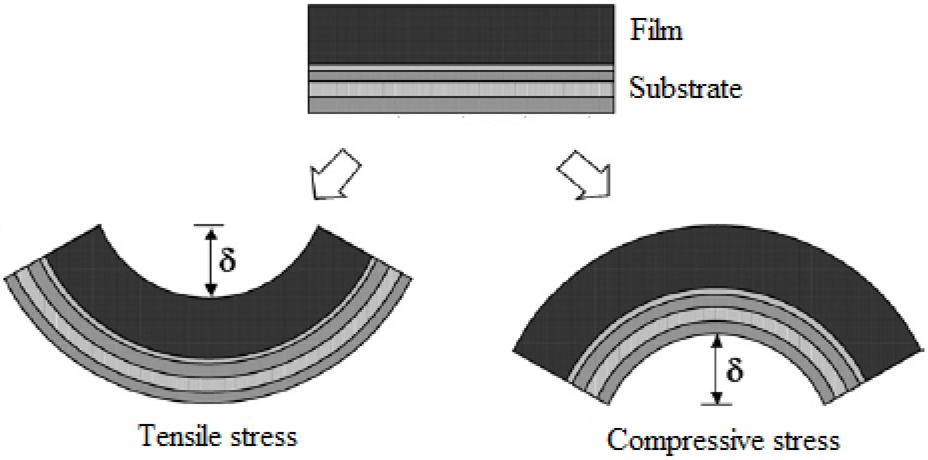

Fig. A.1. Schematic of stress evolution in coatings

The resulting changes in curvature during deposition make it possible to calculate the corresponding variations in stress as a function of deposit thickness. Curvature can be measured using contact methods (e.g. profilometry, strain gauges) or without direct contact (e.g. video, laser scanning, grids, double crystal diffraction topology10), allowing curvatures down to about 0.1 mm21 to be routinely characterised. The intrinsic stress of a film deposited on a substrate has been normally calculated from the substrate's radius of curvature before and after film deposition using the Stoney equation. It is well known that the Stoney equation is valid when a film thickness, t_f is much smaller than a substrate thickness, t_s ($t_f << t_s$). The equation for calculation of the film stress, σ_f can be expressed as:

$$\sigma_f = \frac{1}{6}\left(\frac{1}{R_2} - \frac{1}{R_1}\right)\frac{E_s t_s^2}{(1-v_s)t_f} \qquad \text{(A.2)}$$

Where E_s and v_s denote Young's modulus and Poisson's ratio of the substrate, and R_1 and R_2 are the substrate's radii of curvature before and after film deposition, respectively.

A.3. Force-Displacement measurement by AFM

In addition to topographic measurements, the AFM can also provide much more information. The AFM can record the amount of force felt by the cantilever as the probe tip is brought close to — and even indented into — a sample surface and then pulled away. This technique can be used to measure the long range attractive or repulsive forces between the probe tip and the sample surface, elucidating local chemical and mechanical properties like adhesion and elasticity, and even thickness of adsorbed molecular layers or bond rupture lengths. To help examine the basics of AFM force measurements, fig. A.2a shows a typical force-versus-distance curve or force curve, for short.

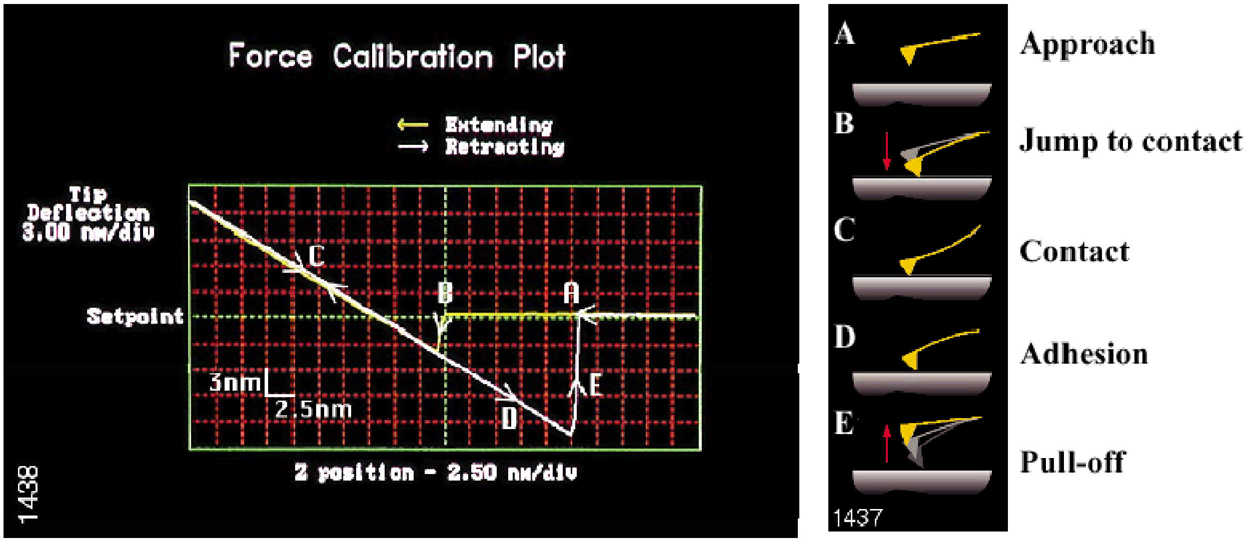

Fig. A.2. (a) Force-Displacement curve generated by AFM and (b) Stages of force-displacement curve)

Force curves typically show the deflection of the free end of the AFM cantilever as the fixed end of the cantilever is brought vertically towards and then away from the sample surface. Experimentally, this is done by applying a triangle-wave voltage pattern to the electrodes for the *z*-axis scanner. This causes the scanner to expand and then contract in the vertical direction, generating relative motion between the cantilever and sample. The deflection of the free end of the cantilever is measured and plotted at many points as the *z*-axis scanner extends the cantilever towards the surface and then retracts it again. By controlling the amplitude and frequency of the triangle-wave voltage pattern, the researcher can vary the distance and speed that the AFM cantilever tip travels during the force measurement. Several points along a typical force curve are shown schematically in fig. A.2b. The cantilever starts (point A) not touching the surface. In this region, if the cantilever feels a long-range attractive (or repulsive) force it will deflect downwards (or upwards) before making contact with the surface. In the case shown, there is minimal longrange force, so this noncontact part of the force curve shows no deflection. As the probe tip is brought very close to the surface, it may jump into contact (B) if it feels sufficient attractive force from the sample. Once the tip is in contact with the surface, cantilever deflection will increase (C) as the fixed end of the cantilever is brought closer to the sample. If the cantilever is sufficiently stiff, the probe tip may indent into the surface at this point. In this case, the slope or shape of the contact part of the force curve (C) can provide information about the elasticity of the sample surface. After loading the cantilever to a desired force value, the process is reversed. As the cantilever is withdrawn, adhesion or bonds formed during contact with the surface may cause the cantilever to adhere to the sample (section D) some distance past the initial contact point on the approach curve (B). A key measurement of the AFM force curve is the point (E) at which the adhesion is broken and the cantilever comes free from the surface. This can be used to measure the rupture force required to break the bond or adhesion.

List of publications

Published (In peer reviewed journals)

1. **A. Mallik** and B. C. Ray, Morphological study of electrodeposited copper under the influence of ultrasound and low temperature, **Thin Solid Films**, 517 (2009) 6612.
2. **A. Mallik**, A. Bankoti and B. C. Ray, A study on the modification of conventional electrochemical crystallization under sonication: The phenomena of secondary nucleation, **Electrochemical and Solid-State Letters**, 12 (2009) F46.
3. **A. Mallik**, S. Rout, A study on ex-situ non-isothermal grain growth behavior of sono-electrochemically deposited Cu thin films, **International Journal of Materials Science,** 1 (2011) 77.
4. **A. Mallik,** B. C. Ray, Evolution of principle and practice of electrodeposited thin film: A review on effect of temperature and sonication, **International Journal of Electrochemistry (In press).**
5. **A. Mallik,** B. C. Ray, Residual stress and nano-mechanical properties of sono-electrodeposited Cu films, **Surface Engineering (Accepted)**.

Communicated (In peer reviewed journals)

1. **A. Mallik** and B. C. Ray, An analysis of the temperature-induced supersaturation effects on structure and properties of sono-electrodeposited copper thin films, **Ultrasonics** (Submitted).
2. **A. Mallik** and B. C. Ray, An understanding of the non-isothermal growth behavior of sono-electroplated Cu thin film, **Thin Solid Films (TSF-D-10-02791) .**
3. **A. Mallik** and B. C. Ray, Implication of low temperature and sonication on Cu electrocrystallization mechanism: A kinetics and structural correlation, **Journal of Electrochemical Society (JES-10-1620).**

Selected list of publication in national & international conferences/ Symposia

1. **A. Mallik** and B. C. Ray, Proceedings of 2nd WSEAS International conference on Nanotechnology (Nanotechnology'10), 20- 22 February 2010, **University of Cambridge, UK**, pp 108-112.
2. **A. Mallik,** B. C. Ray, International Workshop on Physics of Semiconductor Devices (IWPSD 2009), 15-19th December 2009, New Delhi, India.
3. **A. Mallik,** B. C. Ray, 4th Asian Advanced Particle Technology (APT'09), New Delhi, 14-16 September 2009.
4. S. Rout, **A. Mallik** and B. C. Ray, International Conference on Recent Trends in Materials and Characterization (RETMAC -2010) February 14 – 15, 2010, National Institute of Technology, Suratkal, Karnataka.

Curriculum Vitae

Name **Archana Mallik**

Date of birth 01/07/1981

Educational qualification

2010	*PhD* (dissertation submitted) NIT, Rourkela, India
2004	*M.Tech*, Institute of Technology, Banaras Hindu University, UP, India
2002	*B. E.*, Indira Gandhi Institute of Technology, Sarang, Odisha, India

Research and Professional Experiences

2003 – 2004	*Project associate*, Sterlite Industries Pvt. Ltd., Silvassa, India
2006 – 2008	*Lecturer*, Dept. of Metallurgical and Materials Engg., NIT, Rourkela, India
2008 – 2009	*Management trainee* (technical) in Rourkela Steel Plant (SAIL), India
2009 – Cont.	*Asst. Prof.*, Dept. of Metallurgical and Materials Engg., NIT, Rourkela, India

Permanent address

C/O B. C. Malik
At Madhukarkhunta
PO Santaragadia
Dist Balasore, Odisha, India
PIN 756042

Email **archananitrkl@gmail.com**
archanam@nitrkl.ac.in